UNIVERSIDADE D
COIMBRA

João Pedro de Carvalho Saraiva

LARGE-AREA TIME & POSITION SENSITIVE RPC FOR MUON SCATTERING TOMOGRAPHY

Tese no âmbito do Doutoramento em Engenharia Física, Instrumentação, orientada pelo Doutor Alberto Blanco Castro (LIP – Laboratório de Instrumentação e Física Experimental de Partículas) e pela Professora Doutora Maria Isabel Silva Ferreira Lopes (Universidade de Coimbra), e apresentada ao Departamento de Física da Faculdade de Ciências e Tecnologia da Universidade de Coimbra

Agosto de 2025

Large-Area Time & Position Sensitive RPC for Muon Scattering Tomography

Ph.D. Thesis in Engineering Physics

by

João Pedro de Carvalho Saraiva

Coimbra, August 2025

Abstract

Over the past decades, Resistive Plate Chambers (RPCs) have become widely used in high-energy physics experiments, notably for muon triggering and tracking across large areas. RPCs are particularly well suited for muon detection over extensive areas, as they combine relatively low construction cost with high efficiency and precise spatial and temporal resolution. Nevertheless, instrumenting a sensitive area of tens or hundreds of square meters with a strip pitch in the millimeter range can represent a financial challenge primarily driven by the electronics. To address this issue, a novel readout encoding scheme was designed and tested, enabling a significant extension of the detector area without a proportional increase in electronic channels. The method relies on a Signal Merging Printed Circuit Board (SMPCB), which combines signals from multiple readout strips in parallel before feeding them to preamplifiers. By connecting several SMPCBs in a daisy-chain configuration, only 48 electronic channels were needed to read out 888 strips on a 130×90 cm^2 timing Resistive Plate Chamber (tRPC). Comprehensive tests using 30×30 cm^2 prototypes and the 130×90 cm^2 detector demonstrated the effectiveness of the proposed signal multiplexing approach during cosmic-ray measurements. Sub-1 mm 2D spatial resolution and sub-100 ps time resolution were achieved in high-efficiency tRPCs with areas exceeding 1 m^2, while the number of electronic channels was reduced by an order of magnitude.

FLUKA Monte Carlo simulations were also performed to evaluate the use of tRPCs with high spatial and temporal resolution for scanning very large volumes through the Muon Scattering Tomography (MST) technique. Extensive simulations were conducted using the sea-level muon flux as the source term, transported through both a medium-sized volume (1 m^3) and a truck-sized geometry (150 m^3). Two methods were developed to obtain the muon spectrum at the Earth's surface: one based on propagating Primary Cosmic Rays (PCRs) through the FLUKA atmospheric model, and the other employing a muon generator implemented for these tests. An acquisition time of 1 minute was found sufficient to detect a $10 \times 10 \times 10$ cm^3 tungsten block inside a large shipping container. The simulation results for the medium-sized volume were also compared with experimental

data from an MST scan of blocks made of different materials, performed using a 2 m^2 muon tracker. The combination of millimeter spatial resolution and sub-100 ps time resolution for low-energy muon rejection proved adequate for this muon imaging method.

Resumo

Nas últimas décadas, as câmaras de placas resistivas (RPCs) passaram a ser amplamente utilizadas em experiências de física de altas energias, nomeadamente para trigger e determinação de trajetórias de muões em grandes áreas. As RPCs são particularmente adequadas na deteção de muões em extensas áreas, pois combinam um custo de construção relativamente baixo com alta eficiência e elevada resolução espacial e temporal. No entanto, instrumentar uma área ativa de dezenas ou centenas de metros quadrados com uma distância entre strips na ordem dos milímetros pode representar um custo financeiro muito elevado, principalmente devido à eletrónica usada na leitura dos sinais provenientes do detetor. Para fazer face a este problema, um novo esquema de codificação para leitura das strips foi desenvolvido e testado, permitindo uma extensão significativa da área do detetor sem aumentar proporcionalmente o número de canais de eletrónica. O método baseia-se numa placa de junção de sinais (SMPCB), que agrupa em paralelo sinais vindos de várias strips antes de os transmitir aos pré-amplificadores. Ao ligar várias SMPCBs em série, foram necessários apenas 48 canais de eletrónica para ler 888 strips numa timing RPC (tRPC) de 130×90 cm^2. Testes detalhados com protótipos de 30×30 cm^2 e com o detetor de 130×90 cm^2 demonstraram a eficácia da abordagem proposta de multiplexação de sinais durante medições com raios cósmicos. Uma resolução espacial 2D inferior a 1 mm e uma resolução temporal inferior a 100 ps foram alcançadas com tRPCs de alta eficiência e área acima de 1 m^2, reduzindo ao mesmo tempo o número de canais de eletrónica em uma ordem de grandeza.

Realizaram-se também simulações Monte Carlo com o código FLUKA para avaliar o uso de tRPCs de alta resolução espacial e temporal na realização de imagens de extensos volumes através da técnica de tomografia muónica MST. Nesse sentido, efetuou-se um alargado número de simulações usando o fluxo de muões ao nível do mar como fonte de partículas primárias, transportando esses muões em dois volumes diferentes, um de média dimensão (1 m^3) e outro correspondendo ao tamanho de um grande camião (150 m^3). Desenvolveram-se dois métodos para obtenção do espectro de muões na superfície terrestre: um baseado na propagação de raios cósmicos primários (PCRs) através do

modelo atmosférico do FLUKA, e outro usando um gerador de muões implementado para estes testes. Verificou-se que um tempo de aquisição de 1 minuto era suficiente para detetar um bloco de tungsténio de $10 \times 10 \times 10$ cm^3 no interior de um contentor de grandes dimensões. Os resultados da simulação do volume de tamanho médio foram comparados com dados experimentais de uma reconstrução por MST de blocos de diferentes materiais, realizada com um detetor de muões de 2 m^2 por plano. Uma resolução espacial milimétrica combinada com uma resolução temporal inferior a 100 ps para rejeição de muões de baixa energia revelou-se adequada para este método de imagem com muões.

Contents

List of Figures

List of Tables

Acronyms

ADC Analog-to-Digital Converter

CDF Cumulative Distribution Function

CTS Central Trigger System

DAQ Data Acquisition

DB Daughterboard

EMI Electromagnetic Interference

FEE Front-End Electronics

JFET Junction Field-Effect Transistor

FPGA Field-Programmable Gate Array

FR4 Flame Retardant 4

GCR Galactic Cosmic Ray

HEP High Energy Physics

HFC Hydrofluorocarbon

HST Hubble Space Telescope

HV High-Voltage

HVPS High-Voltage Power Supply

LSB Least Significant Bit

LVDS Low-Voltage Differential Signaling

MB Motherboard

MCS Multiple Coulomb Scattering

MIP Minimum Ionizing Particle

MMIC Silicon Monolithic Microwave Integrated Circuit

MRPC Multi-gap Resistive Plate Chamber

MST Muon Scattering Tomography

MTL Multiconductor Transmission Line

NTP Normal Temperature and Pressure

PCB Printed Circuit Board

PCR Primary Cosmic Ray

PDF Probability Density Function

PID Particle Identification

PMT Photomultiplier Tube

PoCA Point of Closest Approach

PP Polypropylene

PPC Parallel-Plate Chamber

PPF Percent Point Function

RPC Resistive Plate Chamber

RMS Root Mean Square

SCR Secondary Cosmic Ray

SiPM Silicon Photomultiplier

SMPCB Signal Merging Printed Circuit Board

SNR Signal-to-Noise Ratio

STIS Space Telescope Imaging Spectrograph

TDC Time-to-Digital Converter

TOF Time Of Flight

ToT Time over Threshold

TRB3 Trigger Readout Board - v3

tRPC timing Resistive Plate Chamber

UV Ultraviolet

Introduction

Over the past decades, the use of Resistive Plate Chambers (RPCs) has become widespread in High Energy Physics (HEP) experiments, notably for muon triggering and tracking across large areas. Additionally, when designed for high time resolution (below 100 ps), these gaseous detectors can be employed in a wider range of applications, including Particle Identification (PID) in Time Of Flight (TOF) measurements.

RPCs are particularly well suited for muon detection over extensive areas since they can, on one hand, be constructed at relatively low cost, and on the other hand, provide high efficiency along with precise spatial and temporal resolution. Over the years, RPCs have found use in related applications beyond HEP. As an example, the 2018 latitude survey from Spain to Antarctica, which used three 1.8 m^2 RPCs to evaluate the correlation between cosmic muon flux at sea level and vertical cutoff rigidity [Sar20].

In large-scale experiments such as ATLAS or CMS at CERN (Geneva, Switzerland), the area covered by RPCs reaches thousands of square meters [Aie13, Pug06]. In comparison, the instrumented surface required to scan large volumes using the Muon Scattering Tomography (MST) technique can also be considerable: for example, scanning a shipping container would require approximately 137 m^2, comparable to the 141 m^2 of RPCs used in ALICE (CERN) [Aki09]. Instrumenting such large areas, with a strip pitch in the millimeter range, would entail significant costs on the electronics side, representing a major financial challenge. Indeed, the larger the area covered by RPCs, the higher the detector cost, primarily driven by the Front-End Electronics (FEE). The best way to tackle this issue would be to decouple the detector surface from the number of FEE channels, even if only partially.

The main purpose of this work is to address the aforementioned problem by designing and testing a novel readout encoding scheme that enables a significant extension of the detector area without a proportional increase in FEE channels. The proposed method relies on the Signal Merging Printed Circuit Board (SMPCB), which combines signals from multiple readout strips in parallel before sending them to the preamplifiers. Of course, decoupling the detector area from the FEE channels is not without consequences, namely

the increased capacitance of each transmission line, which directly impacts electronic noise and leads to signal degradation. Nevertheless, the number of strips multiplexed into a single line can be adjusted based on the acceptable level of signal degradation for the intended application, ultimately determined by its spatial and temporal resolution requirements.

The approach was therefore twofold: **(1)** testing the new readout method with 30×30 cm^2 RPC prototypes followed by a large-area detector of 130×90 cm^2, and **(2)** evaluating, via Monte Carlo simulations, the detector requirements for the MST scan of an extensive volume, such as a truck loaded with a large shipping container.

The contents of each chapter are briefly summarized as follows:

- **Chapter 1** starts with a description of Primary Cosmic Rays (PCRs) and their interactions in the atmosphere. An overview is given of the different components of cosmic-ray showers, with emphasis on the muonic component, which constitutes the most abundant energetic particles at sea level. Due to their high penetrating power, muons are the only particles capable of providing information about the internal structure of very large objects, ranging from nuclear reactors to mountains or volcanoes. No additional radiation exposure beyond the natural muon flux is required for analyzing the internal structure of these large objects, a method known as muon imaging;

- Two main muon imaging techniques exist, relying on different interaction mechanisms with matter. The transmission (or absorption) technique is particularly suited for very large structures, on the order of tens to hundreds of meters, whereas the scattering method (MST) is more appropriate for medium-sized objects, such as shipping containers or nuclear reactors. Both methods are presented in **Chapter 2**, with particular emphasis on the scattering technique, as it corresponds to the main application of interest in this document. The chapter concludes with MST applications, including results from a scan of blocks made of different materials, placed within a volume of 1 m^3 and performed using a muon tracker composed of four 2 m^2 RPCs;

- **Chapter 3** covers RPC detectors, providing a short historical overview and outlining the key developments that led to their current state-of-the-art configuration. A general description of the working principle of these gaseous detectors is also provided, covering the three main physical processes occurring across the detector layers: **(i)** charge creation by ionizing particles, **(ii)** charge multiplication under the influence of the electric field, and **(iii)** signal induction on the pick-up electrodes. Alternative

readout encoding methods to the presented scheme based on the SMPCB are also briefly discussed in this chapter;

- The instrumentation and experimental setups, comprising three prototypes and one large-area timing Resistive Plate Chamber (tRPC), are detailed in **Chapter 4**. A description of all readout electrodes, including the SMPCB, is provided, along with the electronics used to retrieve and amplify the induced signals;

- The experimental results – including efficiency, spatial resolution along and transverse to the strips, and time resolution of the various tested detectors – are discussed in **Chapter 5**. The proposed readout encoding method is also assessed for its impact on precise and unambiguous position reconstruction of ionizing particles crossing each detector. To this end, 2D reconstruction maps of the projected image of scintillators used for external triggering are produced. The details present in the reconstructed images are further evaluated;

- **Chapter 6** concludes with Monte Carlo simulations in which cosmic-ray muons at sea level are propagated through a medium and a large-area geometry to assess the relevant RPC parameters for performing rapid MST scans of objects within these geometries. Two methods to determine the muon flux at sea level are described. One method involves propagating PCRs through the FLUKA atmospheric model to retrieve the muon spectrum at the Earth's surface. The second approach relies on a dedicated muon generator, which is also described in this chapter. After validating the particle spectra from both methods and muon scattering in various materials, the simulation results are presented. Special emphasis is placed on the simulation of the truck platform carrying a shipping container and on the time needed to detect the presence of a small tungsten block inside the container. The required acquisition time is evaluated as a function of the spatial and temporal resolution of the detector. The material budget of the RPCs is also taken into account.

Several results, both experimental and from Monte Carlo simulations, published during the course of this work [Sar23a, Sar23b, Sar24, Sar25], are compiled throughout this document.

1

Cosmic Rays

Since the studies of Victor Hess [Hes12] in the early 20$^{\text{th}}$ century, it has been known that Earth's atmosphere is constantly bombarded by high-energy particles from outer space. These particles, nowadays known as Primary Cosmic Rays (PCRs)[1], are mostly protons (∼90%)[2], alpha particles (∼9%), and heavier nuclei, with energies ranging from a few MeV to hundreds of EeV (tens of Joules) [PDG21, Geo09].

To reach the atmosphere from the vertical direction of a given geographic location, PCRs must have a minimum energy to overcome the geomagnetic field, characterized by the vertical cutoff magnetic rigidity. The magnetic rigidity R is defined as the momentum p (in GeV·c^{-1}) of a charged particle or ion divided by its charge Ze:

$$R = \frac{pc}{Ze} \quad [\text{GV}], \tag{1.1}$$

with c (speed of light) used to express R in volts. A global map of vertical cutoff rigidities can be seen in Figure 1.1. As an example, a proton with momentum below 1 GeV·c^{-1} (i.e., $R < 1$ GV) can reach the atmosphere only at high latitudes ($> \sim 60°$). In contrast, to enter the atmosphere in the equatorial region, a proton must have momentum greater

[1] followed convention: "primaries" refers to cosmic rays interacting with the upper atmosphere, and "secondaries" to the resulting particles.

[2] atomic percentages.

than approximately 12 GeV·c^{-1}.

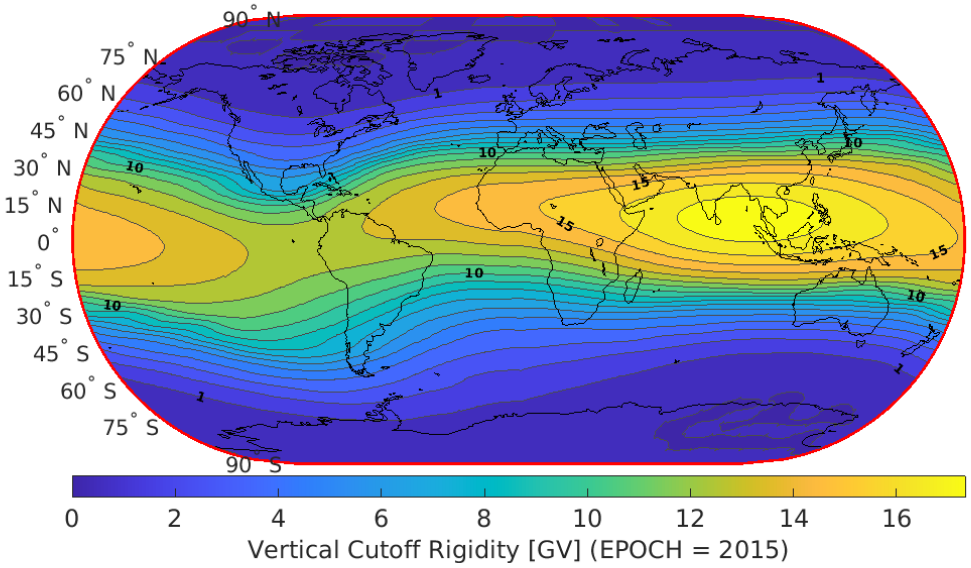

FIGURE 1.1: Vertical cosmic-ray cutoff rigidity [GV] with iso-rigidity contours. Adapted from [Sar20] with updated calculations, using the 12$^{\text{th}}$ generation International Geomagnetic Reference Field for epoch 2015, from [Sma21].

After successfully crossing the magnetic field, PCRs reach the atmosphere, where they encounter an increasing number of molecules and atoms. The vertical atmospheric thickness X at a given altitude h represents the amount of matter traversed by particles along their vertical path up to that altitude and is expressed in units of mass per area. It can be obtained by integrating the atmospheric density ρ along the particle's path r, as expressed in Equation (1.2). The variation of vertical atmospheric thickness with altitude above sea level is shown in Figure 1.2. As illustrated in the figure, the average vertical atmospheric depth at sea level is approximately 1030 g·cm^{-2}.

$$X = \int_{h}^{\infty} \rho \cdot dr \quad [\text{g}\cdot\text{cm}^{-2}] \tag{1.2}$$

In the first few hg·cm^{-2}, primaries interact with atmospheric constituents, producing an increasing number of Secondary Cosmic Rays (SCRs), which can reach and be detected at sea level. The particle flux increases with atmospheric depth, reaching a maximum around 1 hg·cm^{-2}, which corresponds to an altitude of ∼15 km or an atmospheric pressure of 80 mm of mercury, as reported by Pfotzer in 1936 (see Figure 1.3). At lower altitudes, the SCR flux decreases continuously as particles lose energy or decay in the atmosphere.

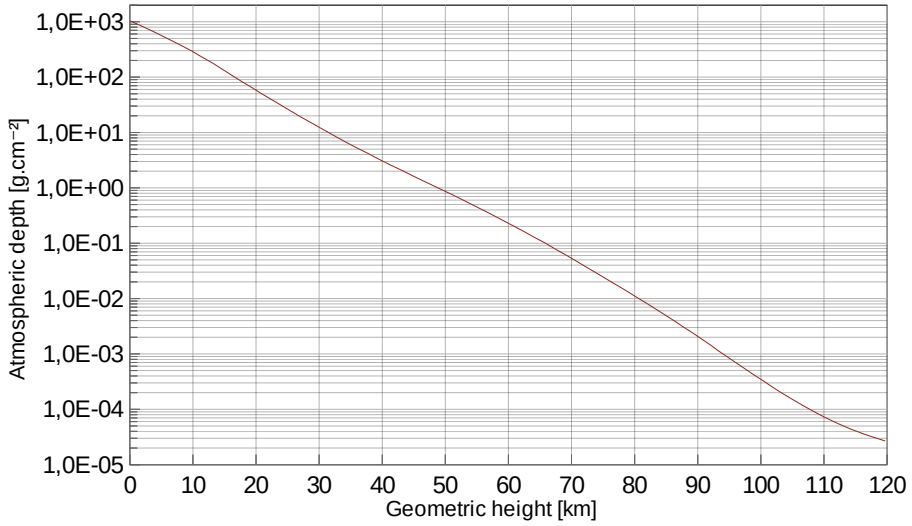

FIGURE 1.2: Vertical atmospheric depth as a function of altitude (0–120 km). Data obtained from the COSPAR International Reference Atmosphere; updated version of Barnett and Chandra, 1990 [NAS07].

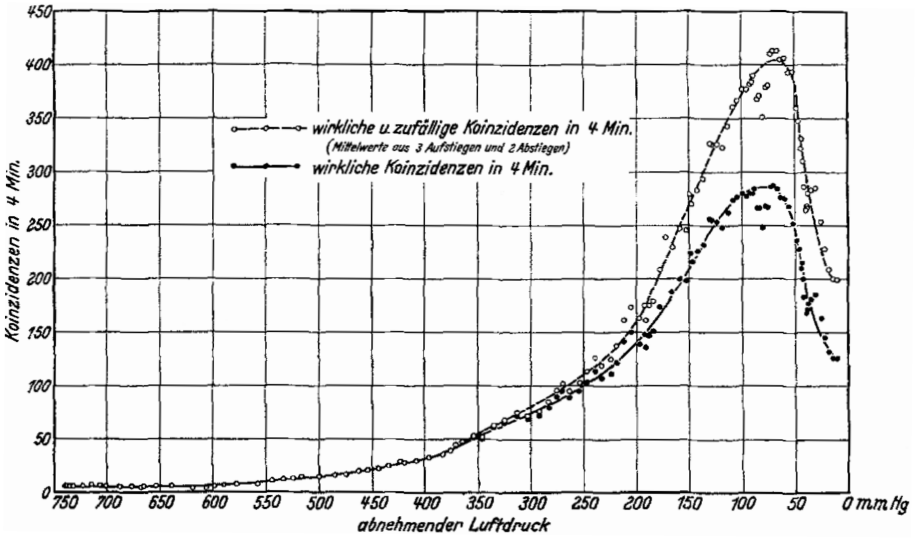

FIGURE 1.3: Particle counting rate of nearly vertical cosmic rays versus atmospheric pressure, as presented by Pfotzer in 1936; mean values from 3 ascents and 2 descents: real+random coincidences (upper curve), real coincidences (lower curve). [Pfo35, Pfo36]

Upon entering the atmosphere, PCRs mainly interact through ionization and inelastic hadronic collisions. While excitation and ionization processes are the most frequent interactions, they play a minor role in the upper atmosphere, as the energy loss by ionization is relatively small, about 1–2 MeV·cm^2·g^{-1} for Minimum Ionizing Particles (MIPs), i.e.,

only ∼200 MeV is lost by a relativistic charged particle reaching an altitude of 15 km from the vertical direction ($X = \sim 100$ g·cm^{-2}, as shown in Figure 1.2). On the other hand, due to the short range of the strong interaction[3], collisions between PCRs and atomic nuclei[4] are much less frequent than Coulomb interactions. However, they contribute substantially to the energy dissipation of primaries with energies on the order of GeV or higher, and to the production of energetic SCRs. These secondaries, in turn, collide with additional atmospheric nuclei, giving rise to the hadronic component of the particle shower (also known as air or atmospheric shower).

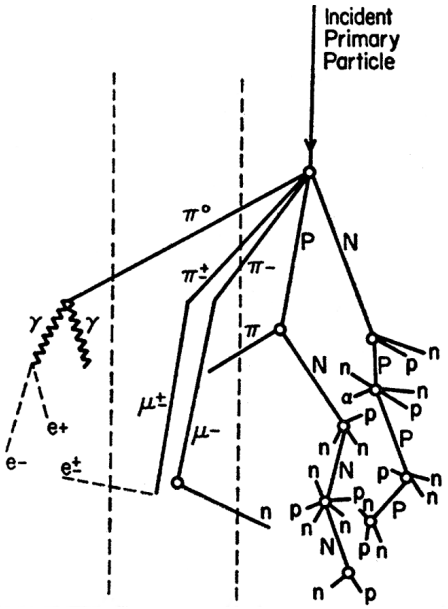

FIGURE 1.4: Schematic representation of the typical development of SCRs in the atmosphere. Adapted from [Sim52].

Air showers can be divided into three cosmic-ray components (see Figure 1.4):

1. **Hadronic component:**

   - **light nuclei**: nuclear fragments from the primary impact that may have enough energy to interact with further nuclei;
   - **nucleons**: high-energy nucleons (up to the incident particle's energy, represented as P and N in the figure) ejected from target nuclei primarily in the forward direction, i.e., close to the trajectory of the parent particles; evaporation nucleons (p and n in the figure) emitted isotropically from target nuclei

[3] on the order of a few femtometers.
[4] with diameters approximately 5 orders of magnitude smaller than typical electronic clouds.

with energies of a few to tens of MeV [Sim52];

- **mesons**: charged and neutral pions, with a production threshold around 290 MeV [Fer97]; heavier mesons, such as charged and neutral kaons and eta mesons, are also produced. These are all unstable particles that either decay or interact, generating further secondaries. Neutral pions and eta mesons predominantly decay into two gamma-ray photons, initiating the electromagnetic component of the shower. Charged pions decay into muons, giving rise to the muonic component of the cascade. Kaons decay as well, producing additional pions and muons;

2. **Electromagnetic component:** gamma-ray photons interact with matter mainly via pair production when their energy exceeds twice the electron rest mass, creating electron–positron pairs. These secondary particles lose most of their energy through bremsstrahlung emission, producing additional photons. This multiplication process in the electromagnetic shower continues as long as the particle energies remain above the electron critical energy[5], which is about 81 MeV in air [PDG21];

3. **Muonic component:** the most penetrating part of atmospheric showers[6]. Most muons are produced at an altitude of around 15 km (see Figure 1.5), where the majority of pions decay ($c\tau$∼7.8 m)[7]. Muons decay into electrons and positrons ($c\tau$∼660 m), but most reach the ground due to time dilation[8]. Some can even penetrate several kilometers of rock (see e.g. the vertical muon intensity versus depth in [PDG21]). The mean energy of muons at sea level is ∼4 GeV [PDG21], and for a vertical trajectory, relativistic muons lose about 2 GeV before reaching the ground. Below 1 GeV more than 60% of the produced muons decay in the atmosphere (see e.g. the muon survival probability in [Gri01]).

All particles in air showers interact more or less strongly with atmospheric constituents. For muons, the main energy loss mechanism when passing through matter is inelastic scattering with orbital electrons, i.e., primarily through atomic excitation and ionization. As leptons, muons don't interact via the strong force, and due to their mass being about 207 times that of electrons, their radiative losses are small: bremsstrahlung is negligible below a few hundred GeV (E_c^μ∼1 TeV in air) [Gri01, PDG21]. Since muons are mainly subject

[5] critical energy E_c: energy at which ionization and bremsstrahlung loss rates are equal.

[6] neutrinos (mainly muon and electron neutrinos, along with their antiparticles) are also produced by the decay of pions, kaons, and muons, but are of no relevance to the present work.

[7] decay length $c\tau$: distance traveled by the particle at the speed of light c during its mean lifetime τ.

[8] e.g., a 6 GeV muon has a decay length $\beta\gamma c\tau$∼38 km, which is reduced by energy loss along its trajectory in the atmosphere; for a pion with the same energy: $\beta\gamma c\tau$∼350 m.

to collision losses[9], they have a much higher penetration capability than other particles and can travel long distances through matter. Muons are in fact the most abundant[10] energetic charged secondaries at sea level, as they are the least likely to undergo interactions with significant energy loss.

As seen in Figure 1.5, for particles above 1 GeV, the vertical flux at sea level consists almost entirely of muons, with much smaller contributions from neutrons, protons, electrons, and pions. Protons and neutrons, in turn, dominate over all other particle species at altitudes above approximately 6–7 km.

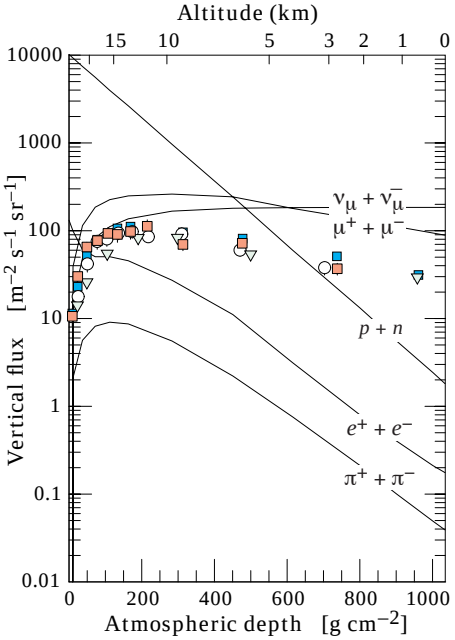

FIGURE 1.5: Calculated vertical fluxes of the major SCR components throughout the atmosphere for energies above 1 GeV (energy region where the particles are most numerous, except for electrons, which are most numerous near their critical energy). The points show measurements of negative muons also with energy above 1 GeV. Taken from [PDG21].

The overall angular distribution of muons at the ground, as a function of zenith angle θ, falls approximately as $cos^2(\theta)$ [PDG21]. However, this dependence of muon intensity with zenith angle varies with the muon energy as follows: **(1)** at higher energies ($>\sim$100 GeV), the muon intensity increases with increasing zenith angle. The competition between decay and interaction for pions and kaons at a given energy changes in favor of decay as

[9] a comprehensive description of muon energy loss mechanisms (ionization, bremsstrahlung, direct electron pair production, direct muon pair and muon trident production, and photonuclear reactions of muons) can be found in [Gri10].

[10] except for the almost non-interacting neutrinos, which, as previously mentioned, are not considered in this work.

the zenith angle increases, since they travel longer paths through lower-density regions compared to vertical propagation (the rate of change of atmospheric density per unit path length is smaller along an inclined trajectory) [Gri01]. Consequently, the greater likelihood of pion or kaon decay at larger zenith angles enhances the muon intensity near the horizon; **(2)** at lower energies, the effect is opposite, as muons at large zenith angles tend to decay before reaching the surface. The combined effect of the previous two points leads to an increase in the average muon energy at sea level with increasing zenith angle.

The energy spectrum of atmospheric muons at sea level is nearly flat below 1 GeV and decreases gradually above this energy, partially reflecting the PCR spectrum [PDG21]. An example of the characteristic features of the muon energy spectrum, including its dependence on the zenith angle, is illustrated in Figure 1.6.

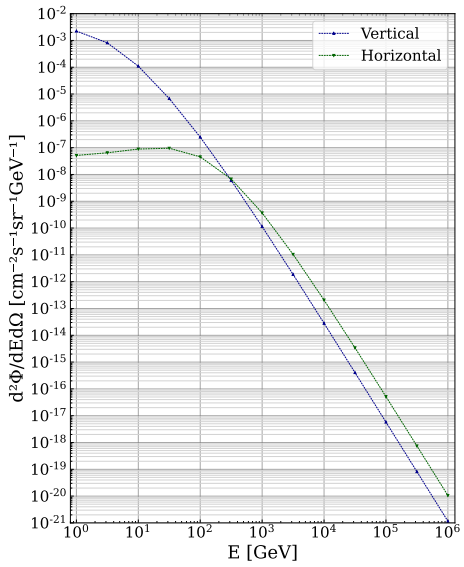

FIGURE 1.6: Analytical calculation of the muon spectra at sea level for vertical ($\theta = 0°$) and horizontal ($\theta = 90°$) directions. The muon enhancement with zenith angle is visible for energies above a few hundred GeV. Based on data from [Lip93].

$I_0 = 80$–90 $\mathrm{m^{-2}{\cdot}s^{-1}{\cdot}sr^{-1}}$ is the vertical intensity at sea level of muons with momentum above 1 GeV/c, as provided in Figure 1.5. Integrating this value over 2π sr and using the $cos^2(\theta)$ dependency, the result is an overall[11] muon intensity I at sea level of around 1 $\mathrm{cm^{-2}{\cdot}min^{-1}}$ or, equivalently, about 170 $\mathrm{m^{-2}{\cdot}s^{-1}}$ (see Equation (1.3)).

$$I = \int_{\Omega} I_0 \cdot cos^2(\theta) = I_0 \int_0^{2\pi} d\phi \int_0^{\pi/2} sin(\theta) cos^2(\theta) d\theta = \frac{2}{3}\pi I_0 \quad [\mathrm{Hz{\cdot}m^{-2}}] \tag{1.3}$$

[11] omnidirectional above the horizon.

2

Muon Imaging Techniques

As discussed in the previous chapter, muons are the most abundant energetic charged SCRs at sea level and exhibit a very high penetration capability, as they are the least likely to interact with significant energy loss. These characteristics make muons the most suitable particles for investigating the internal properties of large-scale objects. Two techniques are available for this purpose. In the first, the muon counting rate is measured after the particles have passed through the scanned object. The differential attenuation of muons across different lines of sight provide information on the amount of material traversed, allowing, for instance, the detection of internal voids. This method, known as muon transmission, muon absorption, or simply muography, is briefly described in the next section. The second approach, referred to as Muon Scattering Tomography (MST), rely on the Coulomb scattering of muons to infer the presence of materials with high atomic number Z ('high-Z materials') in large volumes. In this case, particle tracks must be measured upstream and downstream of the target to infer the scattering angle suffered by the muons along their trajectories. This document focuses primarily on the MST application, which is described in more detail in Section 2.2.

2.1 Muography

For the muography technique, a detector plane must measure the particles that have passed through the large object under investigation. In this configuration, the detector is placed on one side of the object, behind or below it, and measures the natural muon flux over the exposure time required to collect sufficient statistics and achieve the desired precision. The passage of muons arriving from all directions within the detector acceptance is analyzed and then compared to open-sky measurements[1] or Monte Carlo simulations.

The muon attenuation observed for each line of sight is related to the so-called opacity of the target, which depends on both the density and thickness of the material encountered along the trajectories of the muons. The opacity can be quantified in the same way as the atmospheric depth discussed in the previous chapter: by integrating the material density along the muon path (see Equation (1.2)). It is generally expressed in g·cm^{-2} or in meters water equivalent (m.w.e.)[2]. By comparing the attenuated muon flux to open-sky measurements, the material opacity can be inferred. Knowing the dimensions of the studied object, its average density can then be estimated. Measurements can also be repeated from different orientations to produce a 3D representation of the density distribution. Alternatively, if the density is known or estimated, the object's boundaries can be determined.

The dependence of the mean energy loss of muons, and thus their probability of absorption, on the material density can be seen directly from the well-known Bethe formula (Equation (2.1)), bearing in mind that atomic excitation and ionization are the dominant energy loss mechanisms for most muons at sea level (E_c^{μ}~500 GeV in standard rock [PDG21]), as discussed in the previous chapter.

$$-\left\langle \frac{dE}{dx} \right\rangle = K\rho \frac{Z}{A} \frac{z^2}{\beta^2} \left[\frac{1}{2} ln \frac{2m_e c^2 \beta^2 \gamma^2 T_{max}}{I^2} - \beta^2 - \frac{\delta}{2} \right] \quad [\text{MeV.cm}^{-1}] \tag{2.1}$$

The mean stopping power shown in Equation (2.1) includes only the density-effect correction, relevant in the high-energy regime. The symbols and their corresponding values are listed in Table 2.1.

From the analysis of the Bethe formula, one can observe the dependence on the material density, but also on other intrinsic properties of the medium crossed by the muons, namely the atomic number Z, atomic mass A, and mean excitation energy I. Nevertheless, in most cases, all the other contributions can be disregarded: the Z/A ratio is approximately constant at around 0.5 (except for hydrogen), while the contribution of I is reduced by

[1] taken when no target object is present in the field of view; also referred to as free-sky measurements.
[2] 1 m.w.e. = 100 g·cm^{-2} for ρ_{H_2O} = 1 g·cm^{-3}.

Symbol	Definition	Value or Unit
K	$4\pi N_A r_e^2 m_e c^2$	0.3070749 MeV·cm^2·mol^{-1}
N_A	Avogadro's constant	6.02214076×10^{23} mol^{-1}
r_e	classical electron radius	2.8179403262(13) fm
$m_e c^2$	electron rest mass	0.51099895000(15) MeV
c	speed of light in vacuum	299792458 m·s^{-1}
ρ	mass density of the absorber	g·cm^{-3}
Z	atomic number of the absorber	
z	charge number of the incident particle	
A	atomic mass of the absorber	g·mol^{-1}
β	normalized particle velocity (v/c)	
γ	Lorentz factor ($1/\sqrt{1-\beta^2}$)	
T_{max}	maximum energy transfer in a single collision $2m_e c^2\beta^2\gamma^2/(1+2\gamma m_e/M+(m_e/M)^2)$	MeV
I	mean excitation energy of medium (I=f(Z))	eV
δ	density effect correction*	

* relevant at high energies: the electric field of the particle polarizes the atoms along its path, which in turn effectively shields the long-range component of the field, reducing energy loss from distant collisions. δ depends on the particle energy and the material density (greater induced polarization in denser materials). [Leo94]

TABLE 2.1: Symbols and values in the Bethe stopping power equation. [PDG21, BIP19, NIS18]

the logarithmic dependence in the formula. As mentioned earlier, since MIPs lose about 1–2 MeV·cm^2·g^{-1} due to excitation and ionization, the energy loss of most muons at sea level is approximately 100–200 MeV/m.w.e.

2.1.1 Applications of Muography

Muography can be used to study massive bodies such as mountains or volcanoes, often requiring data acquisition times of several days, weeks, or even months. The first known application of muons to evaluate the thickness of rock over an underground facility was performed by Eric George in 1954. As noted in his paper, only one type of radiation could be used to penetrate ∼150 m of rock: 'the cosmic radiation' [Geo55]. George evaluated the overburden above the Guthega-Munyang tunnel (part of the Snowy Mountains Hydro-Electric Scheme in Australia) using 100 Geiger counters arranged in four planes stacked vertically. To minimize background noise, a ∼10 cm lead layer was inserted between the middle two planes, and data acquisition required four-fold coincidence. Figure 2.1 shows the obtained calibration curve relating the counting rate ratio (tunnel/outside) to the corresponding opacity.

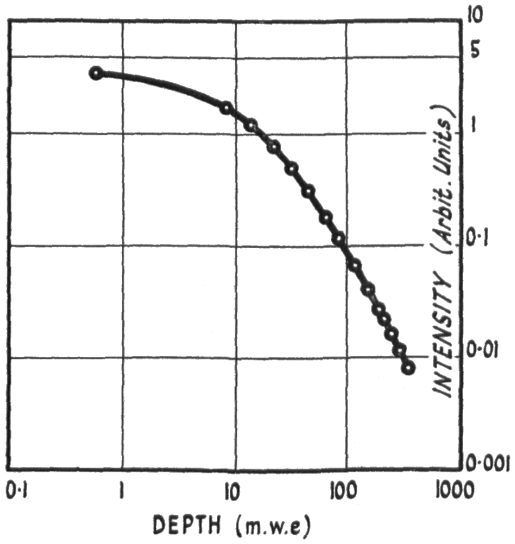

FIGURE 2.1: Muon counting rate ratio as a function of material opacity. Taken from [Geo55].

Having measured a counting ratio of 0.0128, George estimated the opacity of the rock above the tunnel to be 163 ± 8 m.w.e., or equivalently, 16.3 ± 0.8 kg·cm^{-2}. This value was in good agreement with the 17.5 ± 0.6 kg·cm^{-2} obtained through sample drilling.

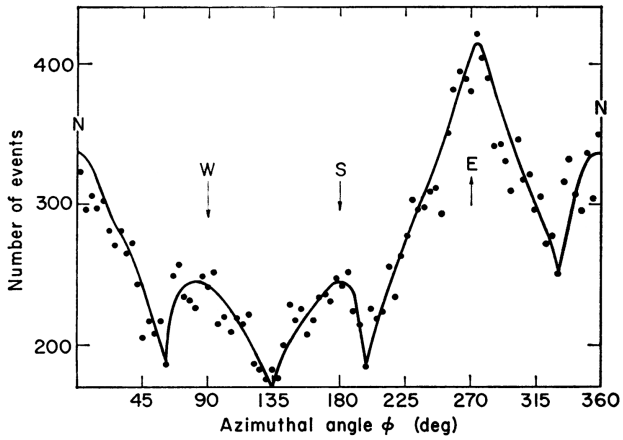

FIGURE 2.2: Variation of the cosmic-ray intensity with azimuthal angle (for zenith angles between 20° and 40°), as measured in the "Belzoni Chamber" beneath the base of the pyramid of Chephren and near its center. The detector was located 15.5 m east and 4 m north of the pyramid's center, which explains the difference in maximum counting rates between the east–west and north–south directions. Taken from [Alv70].

Luis Alvarez, in turn, tried to detect hidden chambers in the pyramid of Chephren at

Giza in 1968, using two 1.8×1.8 m^2 spark chambers[3] placed 30 cm apart vertically, with external triggering provided by three scintillators positioned above and below the detector stack[4] [Alv70]. After months of event acquisition triggered by all three scintillators, no voids were found in the pyramid; however, its four diagonal ridges were clearly identified, as shown in Figure 2.2.

After almost 50 years, several research groups joined efforts to apply the same imaging method to the Khufu pyramid. This time, different detector technologies (emulsion films, scintillators, and Micromegas) were independently used, all confirming the presence of a ∼30 m void located 21 m above ground level, as reported in 2017 [Mor17].

Resistive Plate Chambers (RPCs) have also been employed in muography for the imaging of geological formations, such as the Puy de Dôme volcano in France [Car13, Men16] and the Lousal mine in Portugal [Afo22, Tei22].

As described above, muography is well suited for imaging structures ranging from a few tens to several hundreds of meters, though it requires long exposure times. In cases involving smaller objects and when rapid response is crucial, such as cargo inspection for homeland security, the preferred imaging technique is typically based on the MST method.

2.2 Multiple Scattering Tomography

2.2.1 Multiple Coulomb Scattering

The main energy loss process for muons reaching the ground is inelastic scattering with orbital electrons[5], as briefly mentioned in the previous chapter and described in the section above. This loss mechanism results in a quasi-continuous slowing down of charged particles passing through matter, which is the physical process underlying the muon transmission technique.

The inelastic scattering of muons with nuclei, in turn, results in radiative losses[6] accompanied by trajectory deflection. However, this type of interaction can be neglected if the particle energy is well below the critical energy in the material they are passing through. Elastic scattering with nuclei also occurs frequently, though less often than inelastic collisions with electrons. In this process, particles are deflected by the intense electric field near nuclei but do not radiate. The incident particles lose only the kinetic energy required for conservation of momentum with the target nuclei. Therefore, the latter process has a

[3] two modules (0.9×1.8 m^2) per spark chamber, installed side-by-side.
[4] with a detector acceptance angle around 35° (half-angle of a vertically oriented cone).
[5] excitation and ionization losses.
[6] which includes the bremsstrahlung emission, direct electron pair production and photonuclear reactions [PDG21].

negligible impact on the energy loss[7] of particles but dominates their angular deflection in matter, forming the basis of the MST technique. [Eva55, Leo94]

The vast majority of deflections of heavy charged particles traversing a medium are very small, as shown by Rutherford, Geiger, and Marsden in the early 20^{th} century, with the probability of angular deflection of α particles in a thin foil of gold (∼0.2 µm) being proportional to: **(1)** the inverse fourth power of $\sin(\theta/2)$, where θ is the scattering angle of the incident particles, **(2)** the inverse fourth power of the velocity of the α particles (v_α), and **(3)** the square of the atomic number Z of the scattering nuclei, as illustrated by Equation (2.2). [Gei13]

$$\frac{d\sigma}{d\Omega} \propto \frac{Z^2}{v_\alpha^4 sin^4(\theta/2)} \tag{2.2}$$

The statistical cumulative effect of numerous small-angle scatterings experienced by charged particles traversing a material results in a deflection from their original direction, with an angular distribution that approximately follows a normal distribution with non-Gaussian tails due to rare large-scattering events. The shape and characteristic width of the Multiple Coulomb Scattering (MCS) distribution can be described by Molière's theory; however, simple approximations exist for practical purposes. [PDG21]

The Lynch & Dahl formula (Equation (2.3)) is frequently used as a proxy for Molière's theory and provides the Root Mean Square (RMS)[8] width of a Gaussian approximation to the central 98% of the MCS angular distribution, projected onto a plane containing the initial trajectory. The formula is based on an earlier one, Highland's formula, which in turn was established by fitting the Bethe variant[9] of Molière's theory [Got93]. Lynch & Dahl improved the constants in Highland's formula by performing maximum likelihood fits to the central 98% of projected angular distributions generated by Monte Carlo code[10] [Lyn91].

$$\theta_0 = \frac{13.6 \text{ MeV}}{\beta cp} z \sqrt{\frac{x}{X_0}} \left[1 + 0.038 ln\left(\frac{xz^2}{X_0\beta^2}\right)\right] \quad \text{(rad)} \tag{2.3}$$

The symbols used in Equation (2.3) are defined in Table 2.2. The Lynch & Dahl formula was compared, for instance, to the MCS of 160 MeV protons in several materials, and was shown to be in good agreement with experimental data [Got93]. However, for high-Z

[7] except for low-energy heavy particles that can lead to atomic displacements (non-ionizing energy losses (NIEL)).

[8] the RMS and standard deviation σ coincide in the case of a Gaussian distribution with zero mean deflection, as is the case here.

[9] using $Z(Z+1)$ instead of Z^2 to take into account the scattering induced by atomic electrons.

[10] 10^6 scatters of single-charged heavy particles simulated for materials of different atomic numbers Z and thicknesses.

Symbol	Definition
p	momentum of the incident particle [MeV/c]
βc	velocity of the incident particle (in units of c)
z	charge number of the incident particle
x/X_0	thickness of the scattering medium in radiation lengths
θ_0	RMS width of the projected angular distribution (rad)
θ_{space}	deflection angle (non-projected) (sr)
$\theta_{plane,x}; \theta_{plane,y}$	orthogonal projections of the deflection angle* (rad)

* the orthogonal projections on X and Y planes are independent and identically distributed.

TABLE 2.2: Symbols in the Lynch & Dahl formula and related distributions, using the same notation as in [PDG21].

materials and small thicknesses, it may significantly overestimate the Molière scattering angle [Lyn91, PDG21].

The corresponding projected angular distribution, with zero mean deflection, is given by:

$$\frac{1}{\sqrt{2\pi}\theta_0} e^{-\frac{1}{2}\left(\frac{\theta_{plane}}{\theta_0}\right)^2} d\theta_{plane}, \tag{2.4}$$

and the respective non-projected angular distribution is:

$$\frac{1}{2\pi\theta_0^2} e^{-\frac{1}{2}\left(\frac{\theta_{space}}{\theta_0}\right)^2} d\Omega, \tag{2.5}$$

where $\theta^2_{space} \approx \theta^2_{plane,x} + \theta^2_{plane,y}$ and $d\Omega \approx d\theta_{plane,x}\, d\theta_{plane,y}$. [PDG21]

The dependence of Equation (2.3) on the scattering medium is entirely conveyed by the radiation length X_0. Although MCS is not a radiative process, θ_0 depends on the material's atomic number Z and atomic mass A in a way similar to that of X_0 [Ros41]. This explains why the Lynch & Dahl formula, and those preceding it, express material thickness in radiation lengths. To compute the RMS scattering angle of muons in different targets, one may use tabulated radiation length values for each material (e.g., from [Tsa74]) or perform a quick estimate using Equation (2.6) provided in [Leo94].

$$X_0 = \frac{716.4\, A}{Z(Z+1)ln(287/\sqrt{Z})} \quad [\text{g.cm}^{-2}] \tag{2.6}$$

Table 2.3 lists RMS scattering angles of 4 GeV muons, computed with Equations (2.3) and (2.6) for several target materials, each 10 cm thick. Figure 2.3, in turn, provides the RMS angles as a function of muon momentum for 10 cm-thick materials, and as a function

Material	**Z**	**X_0 [cm]**	**θ_0 (mrad)**	**θ_0 (deg)**
Al	13	8.99	3.60	0.21
Fe	26	1.80	8.55	0.49
Ag	47	0.87	12.57	0.72
W	74	0.35	20.46	1.17
U	92	0.31	21.96	1.26

TABLE 2.3: RMS projected scattering angles of 4 GeV muons crossing 10 cm-thick targets of various materials.

of material thickness for 4 GeV/c muons. As can be seen from the figures, most muons at sea level undergo deflections on the order of 0.1° to a few degrees when passing through 10 cm-thick high-Z materials such as lead, tungsten, or uranium. Since the width of the MCS angular distribution increases with the material's atomic number, MST exploits this effect to discriminate high-Z materials.

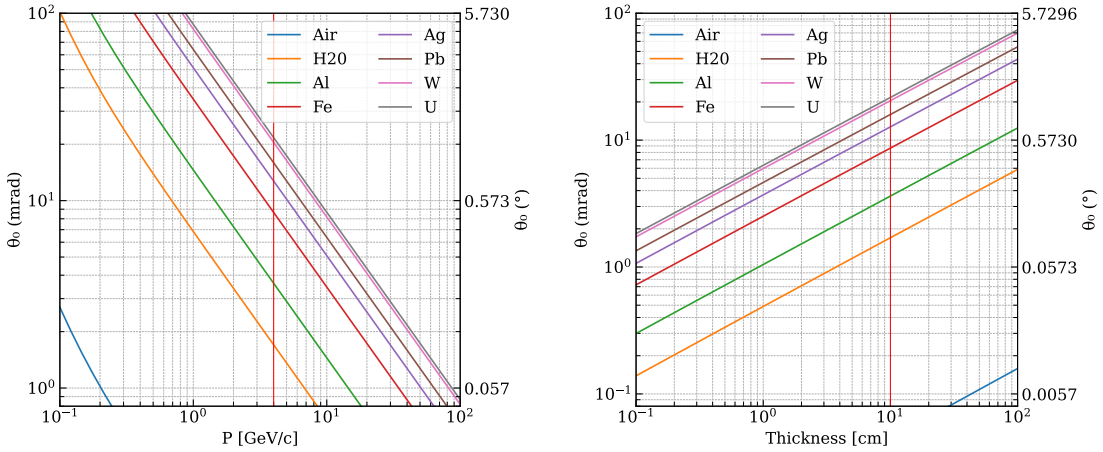

(a) (b)

FIGURE 2.3: RMS projected scattering angles as a function of muon momentum for 10 cm-thick materials (a), and as a function of material thickness for 4 GeV/c muons (b).

While the physical property of interest in MST is the angular deflection of muons traversing a material, it can be considered a side effect in the muography technique. On the other hand, muography relies on muon absorption in large targets, which corresponds to a loss of signal in MST. Another fundamental difference between the two techniques is that MST involves measuring muon trajectories not only downstream but also upstream of the probed volume. This enables the determination of the muon deflections within the scanned region, and thereby the identification of the locations with greater scattering. The

Point of Closest Approach (PoCA) is a simple algorithm that allows the 3D reconstruction of the objects causing these large deflections.

2.2.2 Point of Closest Approach

As previously mentioned, to distinguish between high- and low-Z materials, muon trajectories must be known before and after they traverse the object under study. This can be done by measuring at least four points along each muon path, two upstream and two downstream of the target, as shown in Figure 2.4. The example depicted in the figure corresponds to a real muon trajectory crossing a 20 cm × 10 cm × 5 cm tungsten block, obtained with a tracker consisting of four RPCs, each with nearly 2 m^2 of active area (see the next subsection for further details).

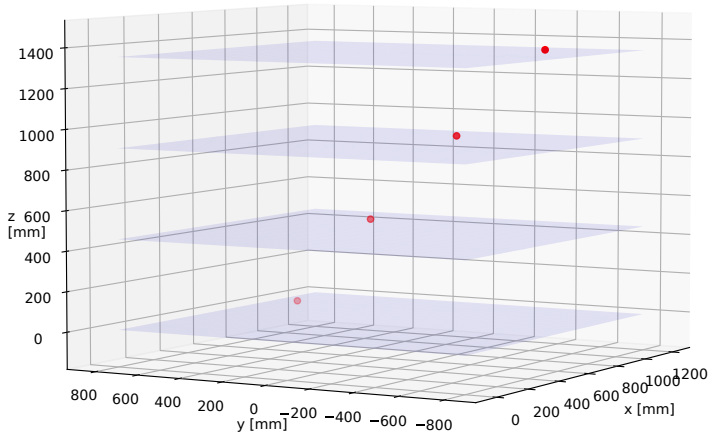

FIGURE 2.4: Four points along a muon track, measured by four 1.6 m × 1.2 m RPCs (represented as blue horizontal planes). A 20 cm × 10 cm × 5 cm tungsten block (X, Y, Z) is placed between the inner detector planes (not shown in the figure). The points in the two upper planes define the incoming trajectory, while those in the lower planes define the outgoing one.

The PoCA algorithm is used to identify the locations of high-scattering events and, in this way, reconstruct the 3D image of the object. The algorithm relies on two main premises: **(1)** the muon undergoes a single Coulomb scattering in the target, rather than multiple scatterings, and **(2)** the location of the scattering point coincides with the point of closest approach between the incoming and outgoing trajectories (the PoCA point).

In the case of coplanar incoming and outgoing trajectories, the PoCA point is simply their intersection; otherwise, it corresponds to the midpoint of the shortest distance between the two trajectories, as depicted in Figure 2.5. The shortest distance between non-coplanar trajectories is called the common perpendicular, as it is the unique line perpendicular to both trajectories.

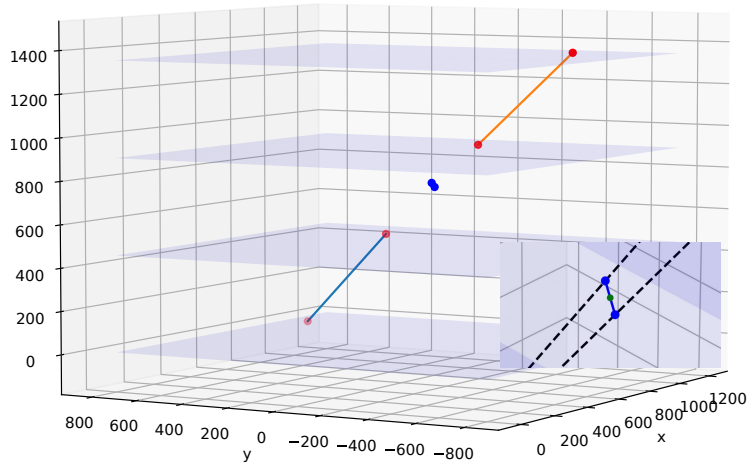

FIGURE 2.5: Same muon path as Figure 2.4 (axes in mm as before). The blue points represent the intersections of the incoming and outgoing extrapolated tracks with their common perpendicular (shortest segment connecting the two trajectories). The PoCA point (midpoint of the common perpendicular) is shown in the inset at the lower right corner of the figure (green point).

Being a stochastic process, the algorithm requires a large number of trajectories to reconstruct the 3D image of the high-Z material, with each PoCA point ideally corresponding to a location inside the target object. Figure 2.6 shows 500000 muon tracks with the tungsten block at the center between the inner detector planes, and two additional blocks (iron and aluminium) positioned on either side (see also Figure 2.7).

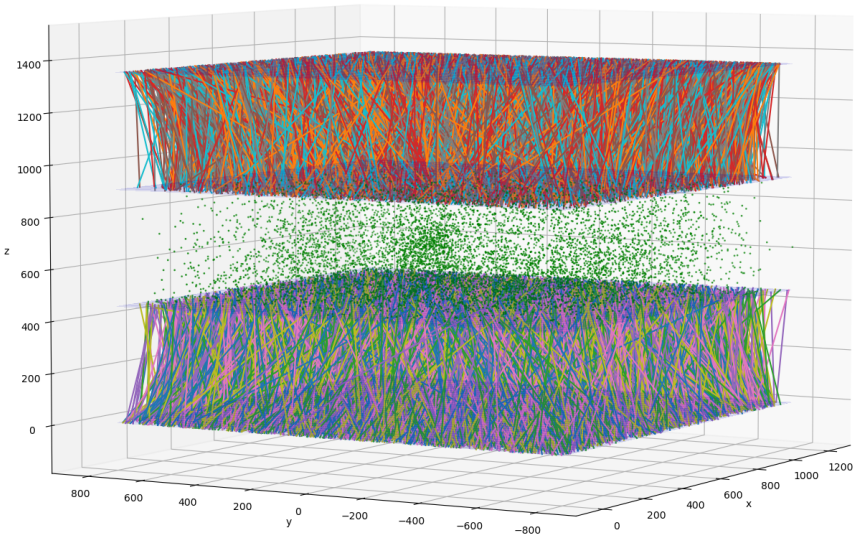

FIGURE 2.6: 500000 tracks with three blocks (Fe, W, and Al) of similar dimensions placed at the center of the scanner volume. Only PoCAs with angular deflections above 11° are plotted (green points) to enhance the visibility of the tungsten block at the center of the scanned volume.

2.2.3 Applications of MST

Materials with high atomic number Z, concealed in medium-sized volumes, can be identified by exploiting the multiple scattering deflections undergone by cosmic-ray muons within the scanned volume, as first reported in 2003 [Bor03]. Using four multiwire proportional chambers spaced 27 cm apart and each with an active area of 60×60 cm^2, the authors were able to identify a tungsten cylinder (radius: 5.5 cm; height: 5.7 cm) and steel support rails within the probed volume [Pri03, Sch03].

Since the MST method involves only the natural flux of muons and does not require active sources, it can be used without radiation exposure restrictions or the need to create safety zones. Moreover, due to their high penetration capability, muons enable the inspection of medium-sized objects within acceptable time frames. The MST technique can therefore be applied to the fields of homeland security and border control, for example to search for smuggled high-Z fissile materials or weapons in commercial trucks or shipping containers. Several companies have been established in recent years, providing products and services that are now commercialized globally. One example is Decision Sciences, which uses drift tube technology with sub-millimeter spatial resolution and low material budget to perform cargo scanning [Dec].

The first application of RPCs for detecting a lead block within a scanned volume was reported in 2012 [Bae12]. The tracker consisted of six 50 cm $\times$ 50 cm planes, with the inner detectors spaced by approximately 70 cm. Each RPC achieved a spatial resolution better than 1 mm. Under this configuration, a 10 cm $\times$ 10 cm $\times$ 15 cm lead block located at the center of the tracker was imaged after approximately 100 minutes of acquisition.

More recently, a muon tracker with four RPCs, each with an active area of nearly 2 m^2, was used to infer, via the MST technique, the presence of small blocks of aluminium, iron, and tungsten within a scanned volume slightly below 1 m^3 (see Figure 2.7). Designed for atmospheric studies and to operate in industrial environments at low gas flux, the tracker featured a spatial resolution on the order of 1 cm and a time resolution of a few hundred ps. [Sar23a, Sar23b]

Although not specifically designed for the MST technique, the presence of a tungsten block measuring 20 cm $\times$ 10 cm $\times$ 5 cm was observed in the first 10 minutes of acquisition. Figure 2.8 shows the projection onto the horizontal plane of the PoCAs that were registered in the fiducial region (volume between the two inner planes) after 10 minutes and after 5 hours of acquisition, for which the muon scattering angle was greater than 10°.

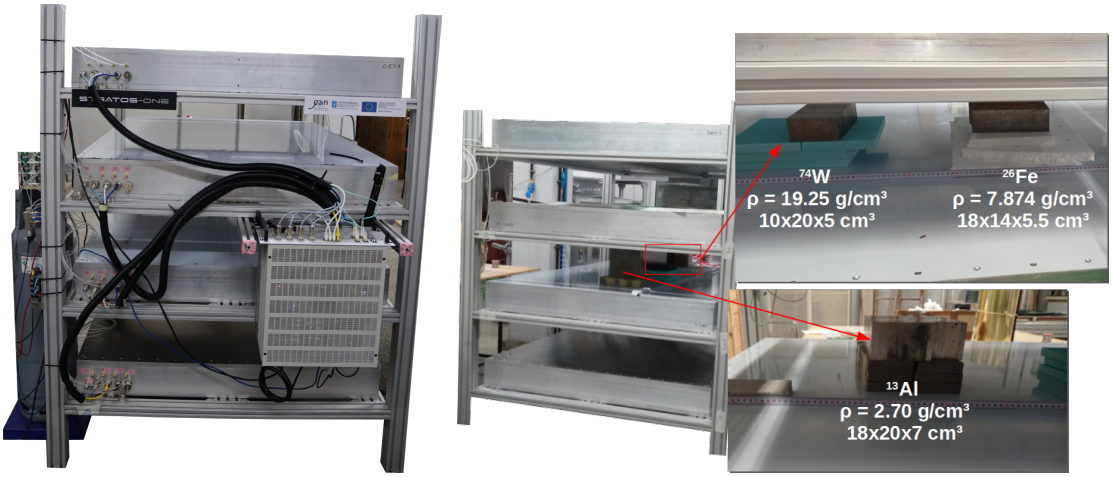

(a) (b)

FIGURE 2.7: (a) Muon tracker composed of four detector planes, 45 cm apart. Each RPC has an active area of 1.6 m × 1.2 m. (b) MST scan of blocks made of different materials: aluminium (Al), iron (Fe), and tungsten (W). The fiducial region is approximately 0.9 m^3.

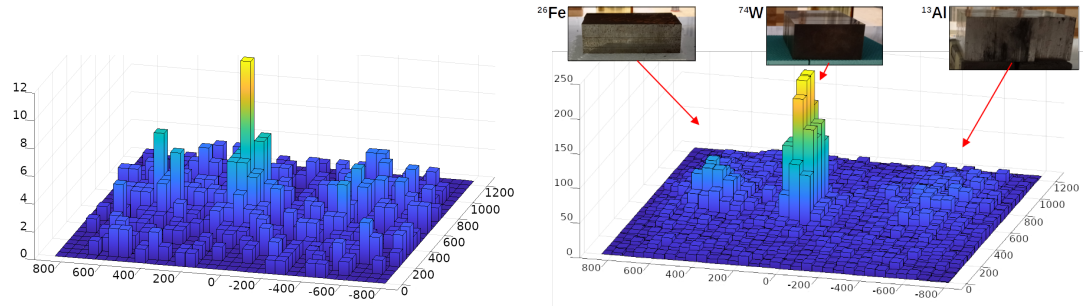

(a) (b)

FIGURE 2.8: 2D projection of PoCAs obtained from the MST scan of small blocks of Al, Fe, and W, restricted to events with muon angular deflection above 10°, after an acquisition time of ∼10 minutes (a) and ∼5 hours (b). Taken from [Sar23b], with the number of PoCAs on the vertical axis and both horizontal axes in mm.

3

Resistive Plate Chambers

In this chapter, the first section provides a historical overview of the main developments that led to the RPCs currently in use. The section concludes with a brief overview of encoding readout methods found in the literature, which, although not specific to RPCs, offer alternatives to the codification discussed in Subsection 4.1.4. The basic physics and the working principle of the RPCs are discussed in Section 3.2. It includes three subsections, each describing a main process occurring in most gaseous detectors: charge creation, charge multiplication, and signal induction.

3.1 Early Developments and Key Contributions

RPCs are gaseous detectors characterized by a planar geometry with at least one resistive electrode. Their development trace back[1] to the works of Keuffel [Keu49] (see timeline in Figure 3.1), and Madansky and Pidd [Mad48], in 1948, leading to the creation of the first Parallel-Plate Chamber (PPC)[2]. At that time, the study of processes such as γ-ray emission from metastable nuclei (isomeric transition) was constrained by the time

[1] In 1924, ionizing particles were already detected by applying a DC voltage to plane-parallel electrodes ('mikrophonlampe') [Bae24]. Years later, Curran referred to these tubes as 'erratic in their behaviour and lacking the required stability of action' [Cur36, Cur54].

[2] also known as Parallel-Plate Spark Chamber or Counter.

resolution of the Geiger-Müller tube, which was around 0.1 µs – barely enough, for instance, for Rossi to measure the muon decay time[3] in 1942 as 2.3 ± 0.2 µs [Ros42]. In cylindrical detectors with a central wire anode, the electric field scales inversely with the radial distance from the anode, while in planar detectors it is uniform across the gap. Under a constant electric field, primary electrons can promptly initiate secondary ionizations after their creation, eliminating the separation between the drift and multiplication regions and drastically improving the PPCs' time resolution. However, these planar detectors require some form of quenching to terminate the discharge initiated by the ionizing particle: **(i)** initially, as implemented by Keuffel, applying only short high-voltage pulses to the metallic electrodes of the PPC, when triggered by external detectors (pulsed or triggered mode of operation), and later **(ii)**, driven by the need to reduce the detector dead time, by replacing the metallic electrodes with resistive ones (continuous mode of operation) [Bab56, Par71]. Despite the complex preparation of the electrode surfaces and the operation at high pressure, the devices of the Novosibirsk group [Par71] are considered the earliest RPC prototypes. In 1978, Pestov achieved a record time resolution of 24 ps (σ), using two glass electrodes (11×11 cm^2), a 0.1 mm gas gap, and an operating pressure of 12 atm [Fed78].

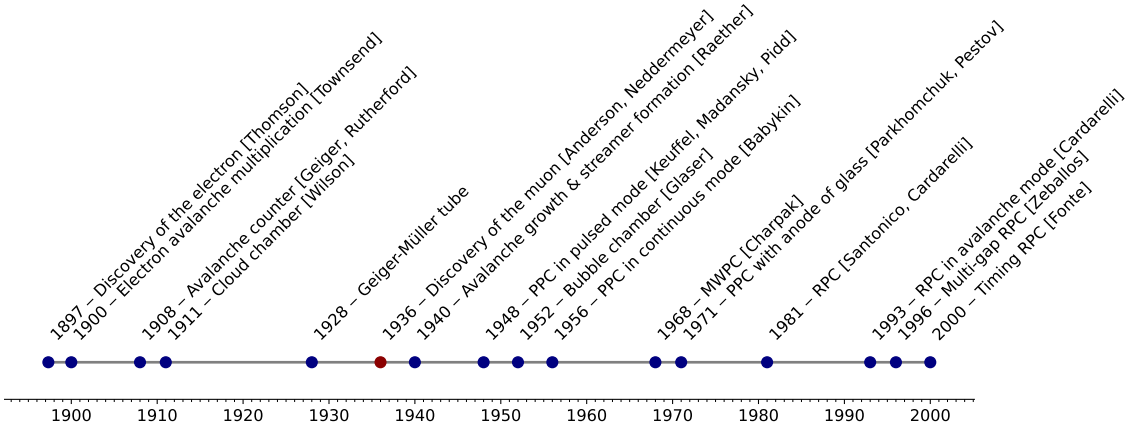

FIGURE 3.1: Timeline highlighting major developments in RPCs, including selected milestones and contemporaneous contributions (not exhaustive).

A further step toward modern RPCs was made by Santonico and Cardarelli in 1981, introducing a significant simplification in both detector construction and operation [San81]. The detector, referred to at the time as a Resistive Plate Counter, featured plastic (bakelite) electrodes with a sensitive area of 85×13 cm^2 and operated with a gas mixture of argon (50% vol) and butane at atmospheric pressure. Using a 1.5 mm gap and bakelite

[3] 2.1969811 ± 0.0000022 µs [PDG24].

plates 2 mm thick, they reported a time resolution close to 500 ps (σ). The RPC operated in streamer mode[4], producing signals of a few hundred millivolts and requiring no pre-amplification.

In 1993, Cardarelli changed the gas mixture to pure Freon 13B1 ($CBrF_3$), an electronegative gas that captures free electrons in the gas, reducing the electronic component of the charge generated during the avalanche process [Car93]. This mode of operation, known as avalanche mode, significantly improves the detector's rate capability[5], as a smaller amount of charge reaches the resistive electrodes and locally discharges them (leading to a smaller reduction of the local electric field in the gas and therefore faster recovery). However, operating an RPC with lower gas amplification (induced signals up to a few mV), implies transferring part of the amplification to the Front-End Electronics (FEE), which must include pre-amplification.

Another key step was the proposal of the Multi-gap Resistive Plate Chamber (MRPC) in 1996 [Zeb96]. The multi-gap technique includes intermediate resistive electrodes that are electrically floating[6], with high voltage applied only to the outermost electrodes. A higher number of gaps increases the overall gas thickness and, consequently, the probability of primary interactions. Since the avalanches in the different gaps contribute to the induced signal, this may lead to an increase in efficiency. However, the greater distance between the readout electrodes – due to the additional gas gaps and inner resistive planes – in turn reduces the overall induced charge, which has the opposite effect on efficiency. The initial goal of their development was to improve time resolution while keeping the advantages of wide-gap RPCs over conventional narrow-gap RPCs, such as a smaller dynamic range and consequently higher rate capability due to the lower charge per avalanche. This work, along with subsequent studies on MRPCs (see e.g. [Zeb97]), showed that time resolution could be improved by using multiple gaps of reduced thickness, triggering the development of a new type of RPC, which has since become known as the timing RPC.

The advent of timing Resistive Plate Chamber (tRPC) technology began in 2000, following a beam test with 7 GeV/c negative pions, which resulted in a record time resolution of 47 ps (σ) using a stack of two MRPCs with sub-millimeter gas gaps, each with two 0.3 mm gaps and a 3×3 cm^2 active area [Fon00]. Two decades after Pestov's work, similar temporal resolution was achieved, but now operating in avalanche mode and at atmospheric pressure. RPCs could then be used in a broader range of applications, including

[4] term commonly used in the RPC community to indicate that the total charge in avalanches created by ionizing particles has reached the Raether limit ($\sim 10^8$ electrons) as explained further.

[5] from particle fluxes of about 100 Hz/cm^2 to more than 1 kHz/cm^2, without significant loss of efficiency.

[6] the intermediate electrodes dynamically reach their equilibrium potential.

Time Of Flight (TOF) measurements for Particle Identification (PID). The current state-of-the-art in time resolution is 21 ps (σ), attained in 2008 with a 24-gap MRPC featuring 0.16 mm wide gaps, with 5 GeV/c negative pions impinging on a 1 cm^2 area [An08].

The first TOF-tracker, combining sub-100 µm spatial resolution and sub-100 ps time resolution in a single device, was reported in 2012. MRPCs featuring five 0.35 mm gaps and a 6×6 cm^2 active area were used, with the total induced charge – comprising the electronic (prompt) and ionic (slow) components of the signal – collected on two orthogonally oriented readout electrodes, each with a 4 mm strip pitch. Using the charge interpolation method for tracking cosmic-ray muons, they achieved a 2D spatial resolution below 100 µm (38 µm in X and 71 µm in Y), along with a time resolution of 77 ps (σ). [Bla12]

More recently, due to the progressive phasing out of Hydrofluorocarbon (HFC) gases because of their high global warming potential, the operation of RPCs in sealed mode, i.e., with zero gas flow instead of the usual continuous gas flux, has been under investigation. Operating RPCs without the need for complex gas systems would represent the most significant simplification since the improvements introduced by Santonico in 1981, offering multiple benefits, such as: enhanced portability for remote locations, improved environmental sustainability, simplified maintenance, and substantially reduced operational costs. The method adopted was to use only glass-based materials for the detector construction, ensuring that the initially supplied gas mixture (97.5% Freon 134a and 2.5% SF_6) remains in contact exclusively with glass. Results after several months of operation of a sealed MRPC featuring two 1.0 mm gaps and a 35 × 35 cm^2 area showed no degradation in performance of the main detector characteristics, as reported in [Bla25].

3.1.1 Readout Encoding Alternatives

Achieving excellent spatial resolution in large detectors requires a high granularity of detection elements (strips or pads in the case of RPCs), which over extended surfaces leads to a large number of readout channels. While the electronics accounts for a significant fraction of the total detector cost, for each ionizing event, only a few of these detection elements are typically involved. Finding an encoding scheme that groups readout elements to reduce the number of electronic channels appears to be a natural consequence of the points outlined above and an effective approach. Of course, such a reduction in electronic channels is not without consequences, which must be taken into account and could limit its use in certain applications:

- a reduction in Signal-to-Noise Ratio (SNR) may occur due to the increased input capacitance resulting from connecting multiple readout elements to a single electronic channel, as detailed in Subsection 5.2.1;

- high-rate fluxes should be avoided, as simultaneous multiple hits would most likely entail an ambiguity that cannot be resolved by the chosen grouping pattern. In turn, applications relying on low particle fluxes, e.g. in high-energy physics or cosmic-ray studies at sea level, are well suited to this approach.

- An increase in detector area raises the probability of multiple primaries crossing it, which in turn increases the possibility of unresolved positional ambiguities. For cosmic rays at sea level, assuming Poissonian arrival times, the multi-hit probability in a 1 m^2 detector within a 1 µs window is well below 1%, reaching 1% only for a time window on the order of 1 ms.

Several encoding methods were proposed by Timothy in the late 1970s and 1980s (see Figure 3.2), all requiring that the passage of a particle generates signals on at least two adjacent readout strips [Tim81]. The first proposed configuration was the coarse-fine scheme, which relies on $m + n$ electronic channels to read out $m \times n$ strips.

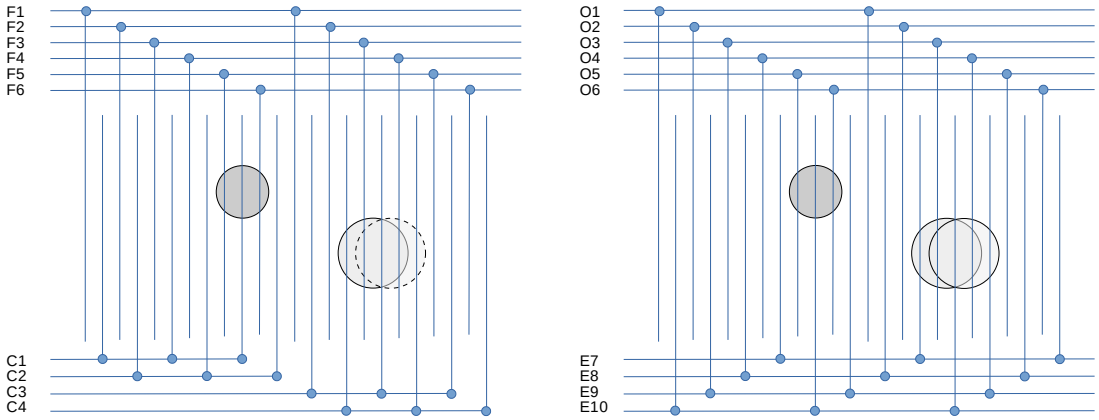

FIGURE 3.2: Example of encoding schemes: the coarse-fine array (a) includes six fine-encoding electrodes (F1 to F6) and four coarse-encoding electrodes (C1 to C4), while the fine-fine array (b) comprises ten fine-encoding electrodes, with six (O1 to O6) connected to odd strips and four (E7 to E10) to even strips. The grey circles represent two events of different multiplicities, with the dashed circle indicating a positional ambiguity unresolved only when using the coarse-fine array. Adapted from [Tim89].

Figure 3.2a depicts $m = 6$ fine-encoding electrodes and $n = 4$ coarse-encoding electrodes, both connected to interleaved strips arranged in a repeating series. The charge collected on each electrode is then routed to a FEE channel. Two events are also shown (grey circles): one with charge collected on three contiguous strips (multiplicity M3), and another on four strips (multiplicity M4). While the position of the M3 event is unequivocally identified

by the output electrode sequence F5–C1–F6, a positional ambiguity arises for the M4 event, as signals on output electrodes n = F3 and F4 and m = C3 and C4 lead to two possible shifted positions, corresponding to the sequences C4–F3–C3–F4 and F3–C3–F4–C4 (dashed circle).

The later-proposed fine-fine configuration resolves the positional ambiguity of M4 events by employing two sets of fine-encoding electrodes connected to the interleaved strips: with one connection pattern repeating every m strips and the other every $m+2$ strips, requiring $2m+2$ electronic channels to read out $m \times (m+2)$ strips. The configuration illustrated in Figure 3.2b includes $m+2=6$ output electrodes connected to odd strips and $m=4$ connected to even strips. Both depicted positions of the M4 event are now unambiguously identified by the sequences E7–O3–E10–O4 and O3–E10–O4–E9. As a result, by replacing the coarse-encoding electrodes with a second set providing fine position encoding, each set of output electrodes corresponds to a unique position, even in the case of higher multiplicities[7].

The fine-fine scheme was implemented, for instance, in the Space Telescope Imaging Spectrograph (STIS)[8] aboard the HST (launched in 1990) [Woo98]. In 2014, Yue tested the same encoding method with MRPCs [Yue14]. Using 30 electronic channels per axis (X, Y) and per MRPC (six in total) to read out 224 strips, they reported a mean position resolution of 800 µm. One year earlier, Procureur proposed a variant of the fine-fine configuration, calling it 'genetic multiplexing' [Pro13]. The method still requires at least two adjacent readout strips to register the passage of the particle but needs only one set of fine-encoding electrodes to identify the respective location. Instead of connecting the strips to the output electrodes in a repeated sequence, they are connected in an unordered way such that any given pair of triggered electronic channels maps to only one possible pair of adjacent strips (see Figure 3.3). Procureur also described a second technique called 'double-sided multiplexing'. In this method, instead of using interleaved strips in the same plane, which connect to both fine-encoding and coarse-encoding electrodes as done by Timothy, the coarse electrodes are placed directly above the thin strips, in a similar way to the approach used in this work (see Subsection 4.1.4).

[7] limited by the size of the smaller set of fine-encoding electrodes: to avoid positional ambiguity, an event can generate signals in up to m-1 electrodes, resulting in a maximum multiplicity of 2×(m-1) strips.

[8] installed on the Hubble Space Telescope (HST) during the second servicing mission, in 1997.

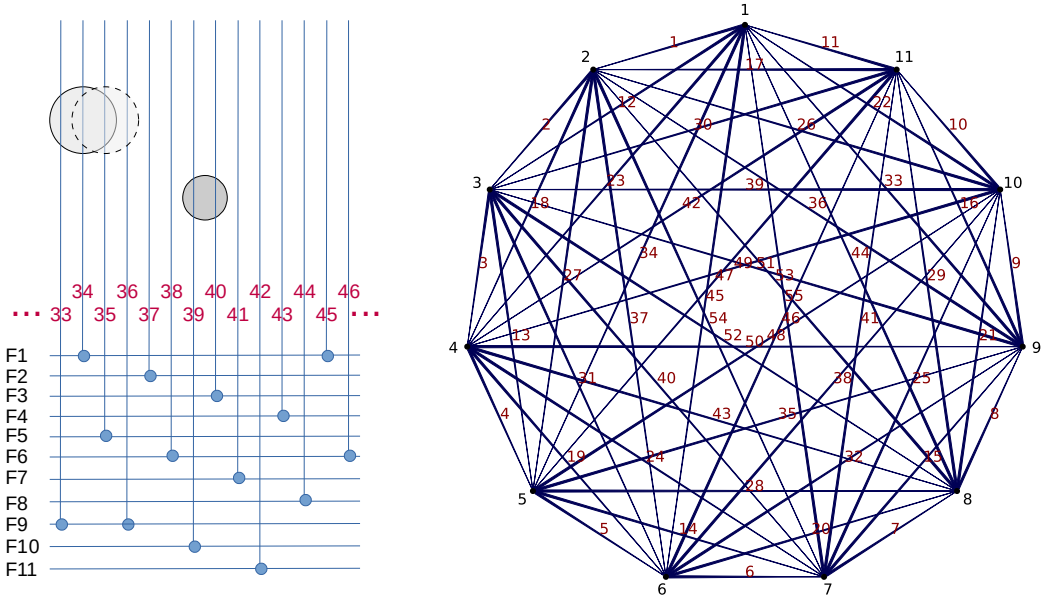

(a) (b)

FIGURE 3.3: Example of an encoding scheme using the genetic multiplexing method to connect 11 electronic channels to 56 strips: (a) the strips (labelled in red) are connected to the fine-encoding electrodes (F1 to F11) in a non-sequential manner such that each pair of adjacent strips corresponds uniquely to a pair of electronic channels. (b) Full sequence of strip-to-channel connections represented with the graph method as proposed by Yue [Yue16]: the vertices of the hendecagon correspond to the electronic channels, and the edges indicate the strips (and their immediate successors) transmitting the signals to the respective pairs of channels. For instance, if channels 10 and 3 were triggered, the event occured in strips 39 (labeled at the center of the edge) and 39+1. This specific encoding scheme cannot handle events with multiplicity M3, as illustrated by the dashed circle (the firing channels 9-1-5 could correspond to an event in strips 33–34–35, 34–35–36, or 33–34–35–36).

3.2 Physics of RPCs

When an ionizing particle passes through the detector and collides with gas molecules in the sensitive volume, it creates a few primary ion-electron pairs along its path. These ions and electrons start drifting to the corresponding electrode due to the presence of the applied electric field. Along their path toward the anode, the electrons can create additional ion-electron pairs starting an avalanche of ionizations. The progression of the avalanches in the gas gaps, in turn, induces current pulses in the readout electrodes that are relayed to the FEE and subsequently, after amplification, to the Data Acquisition (DAQ) board. The conceptual description above can be divided into three main processes: **(i)** charge creation by the passage of the ionizing particle through the gas, **(ii)** charge

multiplication via avalanche development under the applied electric field, and **(iii)** signal induction on readout electrodes positioned as close as possible to the sensitive volume. Each of them is described in the following subsections.

3.2.1 Charge Creation

As discussed in Chapter 1, cosmic-ray muons reach ground level with an average energy of approximately 4 GeV, and are thus essentially MIPs. Since the main application described in this work relies on these particles, the following considerations are limited to interactions involving minimal energy transfer.

Primary Ionizations

The first key quantity to consider regarding the charge deposited in the gas gap is the number of primary ionizations. These primary collisions are also referred to as clusters, as they include the ion-electron pairs directly produced by the ionizing particle, along with additional pairs generated by the primary expelled electrons if their kinetic energy is sufficient to cause further ionizations (δ-rays). Since the secondary ionizations are typically produced in the immediate vicinity of the primary encounter, they collectively form a cluster consisting of one or more ion-electron pairs. The average number of primary pairs (or clusters) per unit length N_P depends on the gas mixture and the energy of the impinging particles. Table 3.1 provides the values of N_P in some gases at Normal Temperature and Pressure (NTP) for unit charge MIPs, along with other physical parameters.

Since MIPs lose a negligible fraction of their energy within the gas gap (see dE/dx in Table 3.1), N_P remains constant along their path. The inverse of the average number of clusters per unit length, $\lambda = 1/N_P$, corresponds to the mean free path of MIPs for primary ionizing collisions, representing the average distance traveled in the gas gap between two interactions producing ion-electron pairs[9].

[9] other interactions can occur along this path, including inelastic interactions leading to atomic excitation or elastic interactions that may deflect the incident particle.

Gas	Density $mg{\cdot}cm^{-3}$	E_x eV	E_I eV	W_I eV	$dE/dx\|_{min}$ $eV{\cdot}mm^{-1}$	N_P mm^{-1}	N_T mm^{-1}
H_2	0.084	10.8	15.4*	37	34	0.52	0.92
He	0.179	19.8	24.6	41.3	32	0.35	0.8
Ne	0.839	16.7	21.6	37	145	1.3	4.0
Ar	1.66	11.6	15.7	26	253	2.5	9.7
Xe	5.495	8.4	12.1	22	687	4.1	31.2
CH_4	0.667	8.8	12.6	30	161	2.8	5.4
C_2H_6	1.26	8.2	11.5	26	291	4.8	11.2
iC_4H_{10}	2.49	6.5	10.6	26	567	9.0	22.0
CO_2	1.84	7.0	13.8	34	335	3.5	10.0
CF_4	3.78	10.0	16.0	35-52	638	5.2-6.3	12.0

* value corrected following [Chr71].

TABLE 3.1: Properties of noble and molecular gases at NTP (20 °C, 1 atm): first excitation energy E_x, first ionization energy E_I, average energy to create one ion-electron pair W_I, differential energy loss for unit charge MIPs $dE/dx|_{min}$, primary N_P and total N_T number of ion-electron pairs per mm for unit charge MIPs (approximate values). [PDG24]

The mean free path can be expressed in terms of the cross section for primary ionization σ_{ion} (see Equation (3.1)), which can in turn be determined experimentally (see e.g. [Rie72]). Dedicated Monte Carlo codes can alternatively be used to evaluate the number of clusters and other relevant parameters [Smi05]. Equation (3.1) relates the mean free path λ to the gas number density N [cm^{-3}] (number of molecules or atoms per unit volume) and the ionization cross section σ_{ion} [cm^2]. For a given gas, the number density can be computed based on the relation $N = N_A{\cdot}\rho/M$, where M the molar mass of the gas [$g{\cdot}mol^{-1}$], ρ is its mass density [$g{\cdot}cm^{-3}$], and N_A is the Avogadro constant [mol^{-1}].

$$\lambda = \frac{1}{N\,\sigma_{ion}} = \frac{M}{N_A\,\rho\,\sigma_{ion}} \tag{3.1}$$

The actual number of primary ionizations in the gas gap, resulting from randomly distributed events with a constant mean free path λ, follows a Poisson distribution with mean l/λ:

$$P(k) = \frac{(l/\lambda)^k}{k!} e^{-\frac{l}{\lambda}}, \tag{3.2}$$

where $P(k)$ is the probability of having k primary ionizations, and l is the particle track length in the gap; for a gas gap of thickness g, $l = g/cos\theta$, with $\theta \in [0; \pi/2[$ the angle between the particle's trajectory and the normal to the gap.

The probability that a vertically incident MIP traverses the gas gap without undergoing

any primary interaction is given by $P(0) = e^{-g/\lambda}$. This result sets the detector inefficiency, which in turn allows one to determine the corresponding theoretical efficiency, defined as the probability of detecting at least one interaction:

$$\epsilon = 1 - e^{\frac{-n_g\, g}{\lambda}} \tag{3.3}$$

This equation establishes an upper limit on the efficiency, as it assumes that all generated primary interactions in the gap are detected. The number of gaps n_g was included in the equation to account for cumulative inefficiency in RPCs with multiple gaps. Table 3.2 reports the efficiency obtained using Equation (3.3) for RPCs with gas gap thicknesses of 0.3 and 1.0 mm, assuming a mean free path of 125 µm (corresponding to $\mathrm{N_P} = 8\ \mathrm{mm}^{-1}$, a typical value for gas mixtures similar to those used in this work (see e.g. [Rie04])). The increase in efficiency with the number of gaps is also shown, explaining why these multi-gap configurations were chosen in the present work.

Number of gaps	Gap thickness µm	Efficiency %
1	300	90.93
6	300	100.00
1	1000	99.97
2	1000	100.00

TABLE 3.2: Upper limit of gaseous detector efficiency calculated for various thicknesses and numbers of gaps, assuming a mean free path of 125 µm for MIPs traversing the gap vertically.

A final consideration regarding the spatial distribution of clusters in the gas gap: since primary ionizations follow a Poisson distribution, the distance between them is exponentially distributed, with the corresponding Probability Density Function (PDF) given by:

$$f(x) = \frac{1}{\lambda}\, e^{-\frac{x}{\lambda}}, \tag{3.4}$$

where x is the distance between successive primary interactions along the particle's track and λ is the mean free path, as defined previously. The respective Cumulative Distribution Function (CDF) is presented in Equation (3.5). The probability that the distance between two successive primary ionizations is smaller than the gap thickness is then given by $F(g)$, providing an alternative approach to obtain the same results[10] as Equation (3.3).

$$F(x) = \int_0^x f(x)\, dx = 1 - e^{-\frac{x}{\lambda}} \tag{3.5}$$

[10] for configurations with multiple gaps, the number of gaps n_g must also be included in Equation (3.5).

Secondary Ionizations

The second key quantity to be taken into account is the total number of ion–electron pairs per unit length N_T which is also provided in Table 3.1. It includes both primary and secondary pairs: the former produced by the MIP, the latter by the δ-rays, as previously mentioned. The comparison of N_T with N_P indicates that the typical cluster size is on the order of 2–3 pairs, varying little on the medium. N_T is computed by dividing the energy loss dE/dx by the average energy per ion pair W_I, both values given in Table 3.1. The table also provides the first ionization energy E_I, the lowest energy to remove an electron from an atom or molecule, and the first excitation energy E_x, just enough to raise it to the lowest excited state. The average energy required to create an ion pair W_I is of the order of a few tens of eV, typically 2 to 3 times higher than E_I, indicating that roughly half of the energy lost by the impinging particle goes into excitation processes[11].

As mentioned above, each cluster includes on average only a few ion–electron pairs, and this number shows little variation with the medium. A frequently cited reference on cluster size measurements across several gases is [Fis91]. Fischle reported the probability of forming clusters containing n = 1, 2, ... electrons for MIPs in argon, helium, methane, ethane, propane, isobutane and carbon dioxide. Figure 3.4 provides the original cluster size distributions in the form of cumulative probabilities. The CDFs show that around 90% of the clusters consist of 3 or fewer ion–electron pairs, while less than 3% have 10 or more pairs. The number of secondary ion–electron pairs can be much higher, even in the hundreds, although with much lower probability. In fact, while the energy transferred by MIPs to primary ejected electrons is most often on the order of a few tens of eV (W_I in Table 3.1), it can reach the keV range or even higher in rare events: for example, approximately 0.6% have kinetic energies of 1 keV or more in argon, and about 0.04% exceed 10 keV (as shown in Figure 35.4 of [PDG24], where their 'practical ranges' are also given as 50 µm and 1.5 mm for 1 keV and 10 keV electrons, respectively).

[11] radiative losses remain negligible for muons in the GeV range.

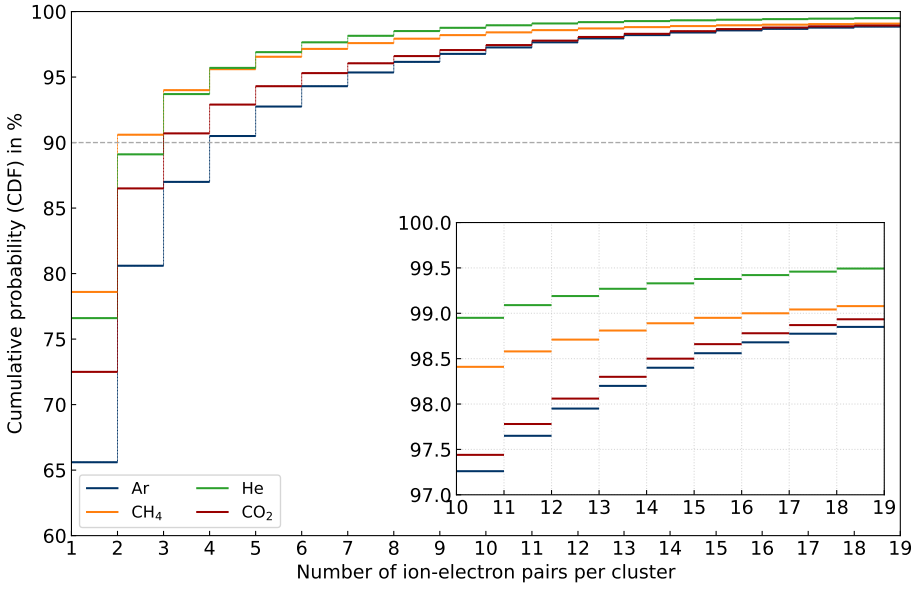

FIGURE 3.4: Cumulative distributions of the number of ion–electron pairs per cluster for MIPs in four gases: argon, helium, methane, and carbon dioxide. The CDFs of ethane, propane and isobutane are equivalent to that of methane. The inset shows the cumulative probabilities of observing a cluster with 10 or more pairs. Adapted from [Fis91].

To summarize the first process of charge creation, when a cosmic-ray muon traverses the gas gaps of the RPCs used in this work:

- as MIPs, muons lose only hundreds of eV per millimeter of gas, with roughly half of the energy going into atomic or molecular excitation and the other half into ionization;
- on average, each muon travels ∼125 µm before producing an ionizing event;
- the corresponding number of primary ionizing events (or clusters), which follows a Poisson distribution, averages about 8 in the 1 mm gap and 2.4 in the 0.3 mm gap;
- to reach a theoretical detector efficiency of 100%, 6 gas gaps are required for the 0.3 mm thickness case, and 2 for the 1 mm case;
- if the primary electron is ejected with a kinetic energy of a few tens of eV, it may produce an additional ionization, known as secondary ionization event, occurring in the surroundings of the first encounter (from a few to tens of micrometers, or more in rare cases of δ-rays with energies above 1 keV);
- the primary ejected electron has, on average, enough energy to produce 1 to 2 secondary pairs, corresponding to an average cluster size of 2 to 3 pairs;

- based on percentile analysis with similar gases, around 90% of the clusters have 1 to 3 ion–electron pairs, less than 3% have more than 10 pairs, while rare events can produce hundreds.

As previously discussed, the passage of a MIP through a 1 mm gap generates on average a few tens of electrons, corresponding to a charge on the order of 0.01 fC. Knowing that the charge induced on the readout electrodes is only a fraction of that created in the gas gap[12], it becomes clear that a gas amplification of several orders of magnitude is required to reach the readout electronics threshold (tens of fC).

3.2.2 Charge Multiplication

Under the effect of an electric field E [V·cm^{-1}], the created charges mentioned in the previous subsection, start migrating toward the respective electrode. As reported by Townsend in 1900 [Tow00], for a given gas pressure and if the electric field between two parallel plates exceeds a certain threshold, n_e electrons moving an infinitesimal distance dx toward the anode produce dn_e additional electrons, according to the relation:

$$dn_e = \alpha n_e dx, \tag{3.6}$$

where α is now known as the first Townsend coefficient, representing the average number of ionizing collisions an electron undergoes per unit length in the direction of the anode. α depends on the reduced electric field[13] E/N [V·cm^2], where N is the gas number density [cm^{-3}], as defined in the previous subsection. E/N is generally expressed in Townsend (Td) units, where 1 Td = 10^{-17} V·cm^2.

At a fixed reduced electric field, both electrons and ions drifting through the gas reach equilibrium, each traveling with a specific drift velocity and mean energy. Under these circumstances, the first Townsend coefficient remains unchanged along the entire gas gap, and the integration of Equation (3.6) over the distance x, followed by straightforward manipulations, yields:

$$n_e(x) = n_{e_0} e^{\alpha\, x}, \tag{3.7}$$

with n_{e_0} the number of electrons at $x = 0$, the starting point of the avalanche. In the case of an avalanche developing across the entire gap thickness g, $n_e(g) = n_{e_0} e^{\alpha\, g}$, with $e^{\alpha\, g}$ referred to as the gas gain.

[12] depending on the detector geometry, one can roughly assume a reduction factor of 10 between the charge collected on the anode and the charge induced on the readout electrodes.

[13] also expressed as E/p [V·m^{-1}·torr^{-1}], with p the gas pressure.

Other processes occur simultaneously with the ionizing collisions mentioned above. For instance, drifting electrons can attach to atoms or molecules in the gas, forming negative ions. This mechanism is particularly important in gases with high electron affinity[14], as it reduces the number of free electrons and thus the number of ionizations in the avalanche. A coefficient of attachment η can therefore be defined as the average number of electron captures per unit length along the direction of the electric field. The effective first Townsend coefficient, defined as $\alpha_{\text{eff}} = \alpha - \eta$, accounts for the reduction in ionizations due to electron attachments. Using α_{eff} in Equation (3.7), the exponential gain reduces to $e^{\alpha_{\text{eff}}\, x}$, with the total number of electrons after a distance x in the presence of attachment given by Equation (3.8). Figure 3.5a shows numerical calculations of the effective Townsend coefficient in various gases as a function of the reduced electric field [LXC]. For the SF_6, the first Townsend and attachment coefficients are also shown. The figure also includes experimental measurements of α_{eff} in Freon 134a ($C_2H_2F_4$) [Urq09], the main gas used in the present work.

$$n_e(x) = n_{e_0} e^{\alpha_{\text{eff}}\, x} \tag{3.8}$$

A direct consequence of electron attachment is the reduction of the induced signal (the fast electronic component) on the readout electrodes, as observed by Cardarelli in 1993 when pure Freon 13B1 was used in an RPC detector (see Section 3.1). Another beneficial effect is the reduced transverse progression of the avalanche, which remains localized near the primary event. The negative ions created during attachment migrate much more slowly than electrons toward the anode, contributing – together with the positive ions – to the slow ionic component of the induced signal, as shown in the next subsection. Several other processes can occur in the gas gap depending on the gas mixture used. A comprehensive list can be found in [Dav73].

The drift velocities of electrons v_e and ions v_i result from the combined effect of acceleration by the electric field E and momentum loss in collisions with gas molecules. They can be expressed in terms of the respective mobilities as:

$$\begin{aligned} \vec{v}_e &= -\,\mu_e(E/N)\,\vec{E} \\ \vec{v}_i &= \quad \mu_i(E/N)\,\vec{E} \end{aligned} \tag{3.9}$$

with the electron μ_e and ion μ_i mobilities, expressed in $[\text{cm}^2{\cdot}\text{V}^{-1}{\cdot}\text{s}^{-1}]$, and dependent on the reduced electric field. Figure 3.5b presents numerical results for the electron drift velocity in several gases, along with measurements in Freon 134a. For comparison, the

[14] ability of a neutral atom or molecule to attract and capture a free electron.

drift velocity of the positive species CO_2^+ migrating in CO_2 is also shown. As can be seen from the figure, ion velocities are at least two orders of magnitude lower than those of electrons.

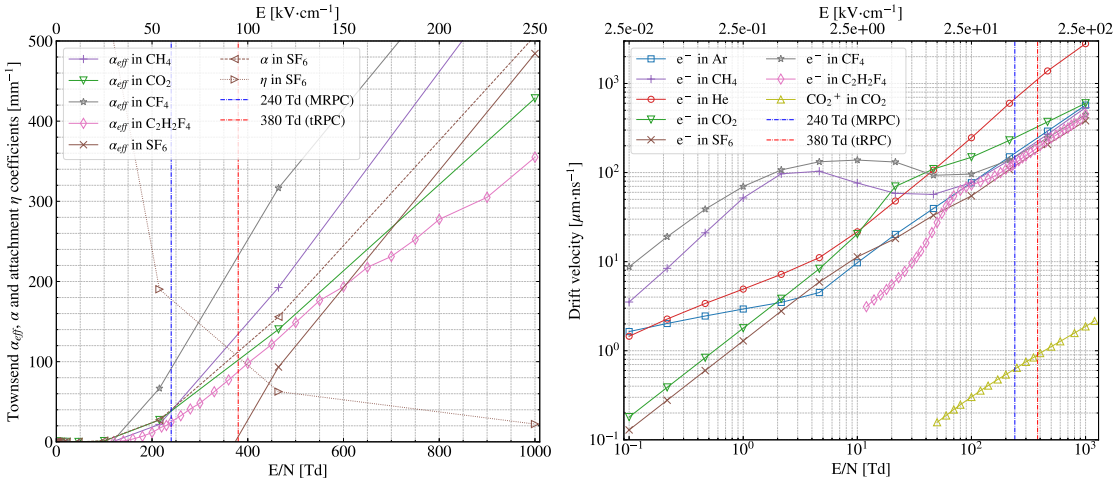

(a) (b)

FIGURE 3.5: (a) Effective Townsend coefficients α_{eff} from numerical calculations in CH_4, CO_2, SF_6 (Biagi database) and CF_4 (Bordage database) available on the LXCAT website [LXC], and from experimental measurements in $C_2H_2F_4$ [Urq09]. For the SF_6, the first Townsend α and attachment η coefficients are also included. Values are presented as a function of E/N and the corresponding electric field E in kV·cm^{-1}, assuming gas number density at NTP conditions (2.50×10^{19} cm^{-3} at 20 °C and 1 atm). The vertical lines indicate the nominal reduced fields applied to the RPCs in this work: two 1 mm gaps at 240 Td and six 0.3 mm gaps at 380 Td. (b) Drift velocities of electrons calculated for the same gases (Ar and He also from Biagi database), including also the measurements in $C_2H_2F_4$. The drift velocity of the CO_2^+ ion in CO_2 (Viehland database) is also shown for comparison.

Based on the analysis of Figure 3.5 and the range of E/N values applied to the RPCs used in this work (Freon 134a ($C_2H_2F_4$) as the main gas mixture), it follows that:

- an electron emitted near the cathode, traversing a 1 mm gap with an E/N of 240 Td, produces slightly more than 20 ionizations through avalanche multiplication – close to the Raether limit, as discussed below. For comparison, a MIP crossing the same gap generates on average approximately 8 primary ionizations, as seen in the previous subsection;
- assuming an effective Townsend coefficient of 25 ionizations per mm, the corresponding mean free path $1/\alpha_{\text{eff}}$ of electrons in the avalanche is approximately 40 µm (125 µm for the primary ionizing particle, as seen before);
- At 380 Td, the effective electron multiplication increases to 90 mm^{-1} and $1/\alpha_{\text{eff}}$

decreases to ∼11 µm. Over a 0.3 mm gap, this avalanche growth is self-limited by the large accumulation of charge, which locally reduces the electric field due to space-charge effects (see below). The addition of a small percentage of SF_6 also contributes to the gas gain reduction;

- the electron drift velocity is on the order of 100 µm/ns (∼140 at 240 Td and ∼200 µm/ns at 380 Td, i.e., below 0.1% c), taking a few nanoseconds to cross the 1 mm gap.

Temporal and Spatial Development of the Avalanche

Over time, electrons in the gas gap drift under the influence of the external electric field while simultaneously undergoing diffusion. In the absence of an electric field, diffusion is isotropic and driven only by thermal motion. The spatial distribution of a point-like source evolves over time t into a Gaussian profile with variance $2Dt$, where D is the diffusion coefficient[15] of the electron [m^2/s]. In the presence of an electric field, electron diffusion becomes anisotropic, being characterized by the longitudinal D_L and transverse D_T diffusion coefficients.

The spatial and temporal evolution of avalanche growth is commonly described by a transport equation accounting for diffusion, drift and a source term for ionization multiplication and attachment, as in [Mee53, Dav73]:

$$\frac{\partial n_e}{\partial t} = D_L \frac{\partial^2 n_e}{\partial x^2} + D_T \left(\frac{\partial^2 n_e}{\partial y^2} + \frac{\partial^2 n_e}{\partial z^2} \right) - v_e \frac{\partial n_e}{\partial x} + \alpha_{\text{eff}} v_e n_e, \tag{3.10}$$

where $n_e = n_e(x, y, z, t)$ denotes the electron density at position (x, y, z) and time t; v_e is the electron drift velocity, and α_{eff} is the effective first Townsend coefficient, as previously defined. The electric field is set along the X-axis. Assuming a point-like initial condition with n_{e_0} electrons released at $x = y = z = 0$ and $t = 0$, Equation (3.10) has the following solution [Mee53, Rae64]:

$$n_e(x, y, z, t) = \frac{n_{e_0}}{(4\pi D_T t)\sqrt{4\pi D_L t}} e^{\alpha_{\text{eff}} v_e t} e^{-\frac{(x - v_e t)^2}{4 D_L t}} e^{-\frac{y^2 + z^2}{4 D_T t}}. \tag{3.11}$$

Electrons are distributed in a Gaussian profile that drifts along the X-axis and grows exponentially. In the approximation of isotropic diffusion, where $D = D_L = D_T$, Equation (3.11)

[15] at thermal equilibrium, $D = \mu k_B T/q$, where q is the particle charge, μ its mobility, T the temperature, and k_B the Boltzmann's constant.

simplifies to:

$$\begin{aligned} n_e(x,y,z,t) &= \frac{n_{e_0}}{(4\pi Dt)^{3/2}}\, e^{\alpha_{\text{eff}} v_e t}\, e^{-\frac{(x-v_e t)^2+y^2+z^2}{4Dt}} \\ &= \frac{n_{e_0}}{(4\pi Dt)^{3/2}}\, e^{\alpha_{\text{eff}} v_e t\, -\, \frac{(x-v_e t)^2+y^2+z^2}{4Dt}}. \end{aligned} \tag{3.12}$$

Under the same approximation, Equation (3.10) can be rewritten as:

$$\frac{\partial n_e}{\partial t} = D\nabla^2 n_e - \vec{v}_e \cdot \nabla n_e + \alpha_{\text{eff}} v_e n_e. \tag{3.13}$$

By applying the additional simplification of neglecting diffusion ($D = 0$) and assuming steady-state conditions ($\partial n_e/\partial t = 0$), it follows that:

$$\begin{aligned} \vec{v}_e \cdot \nabla n_e &= \alpha_{\text{eff}} v_e n_e \\ v_e \frac{dn_e}{dx} &= \alpha_{\text{eff}} v_e n_e \\ dn_e &= \alpha_{\text{eff}} n_e\, dx, \end{aligned} \tag{3.14}$$

which corresponds to the simplified form of Equation (3.6), describing the spatial evolution of the number of electrons under the effects of drift and effective ionization only.

Space-Charge Effects

The gas gain given by Equation (3.8) deviates from exponential growth when the electric field generated by the ions and electrons in the avalanche approaches the applied field in the gap (E_0). The field distortion caused by the accumulated space charge in the avalanche is known as space-charge effect. This effect plays a crucial role in the avalanche-to-streamer transition, as observed by Raether in the late 1930s using plane-parallel electrodes inside a cloud chamber [Rae38, Rae39]. He observed that when a critical amplification of $\alpha x \approx 20$ is reached[16], the avalanche transitions into a rapidly advancing channel discharge[17] – initially referring to the formation process as Kanalaufbau [Rae40], and later in its 1964 survey as streamer mechanism [Rae64].

As the avalanche size grows beyond $\sim 10^6$ electrons, its progression is influenced by the space-charge field arising from the accumulation of electrons at the avalanche head and trailing ions in its tail. Two direct consequences follow:

- due to the strong accumulation of charge, the field lines of E_0 are bent toward the head and the central part of the avalanche, increasing the field intensity in the regions

[16] the so-called Raether limit, corresponding to an avalanche size of $e^{20} \approx 10^8$ electrons.

[17] Vorentladungskanal (pre-discharge channel) and Funkenkanal (spark channel), as described in early German papers.

in front of the head and behind the tail (see Figure 3.6). These high-gain regions can enhance further ionizations, leading to rapidly growing secondary avalanches and ultimately to the formation of a streamer – a thin plasma channel that, in its final stage, can extend from the anode to the cathode, locally discharging the resistive electrodes;

- in the overlapping region of electrons and ions within the avalanche, the space-charge field opposes E_0, thereby reducing its effective strength and the avalanche's gas gain. As a consequence, the avalanche reaches a saturated state in which the rate of new ionizations drops drastically, allowing RPCs to operate at an initially high gain while still avoiding exceeding the Raether limit, i.e., preventing streamer formation (see below: timing RPCs).

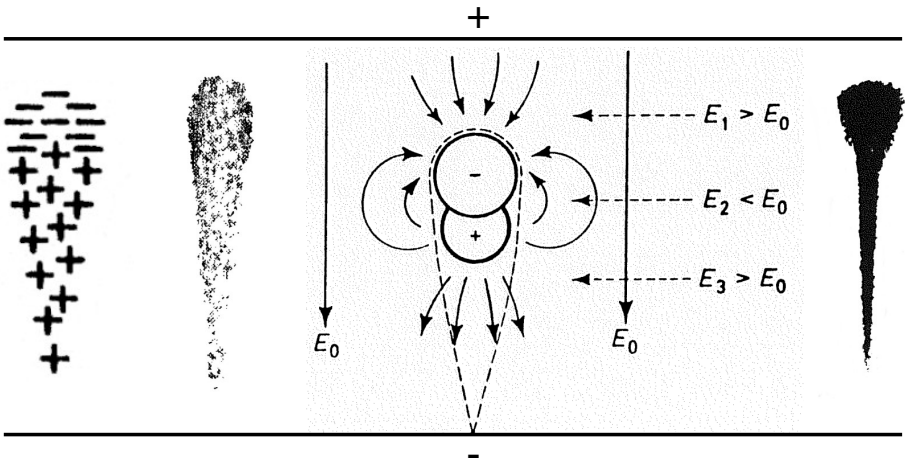

FIGURE 3.6: From left to right: charge carrier distribution in the avalanche; picture of a low-amplification avalanche ($e^{\alpha x} < 10^6$) showing a rounded head shape; space-charge effects in a high-gain avalanche; image of an avalanche approaching the Raether limit, resulting in significant expansion of the electron cloud at the head. Both avalanches are photographic negatives recorded in a cloud chamber. Adapted from [Rae64].

Figure 3.6 presents a collection of images from [Rae64], illustrating from left to right:

- charge distribution in the avalanche, with two regions depicted: the head, which consists primarily of electrons, and the body or tail, which is dominated by positive ions;

- negative image of an avalanche in CO_2 at ~0.2 atm within a 3.6 cm gas gap. The High-Voltage (HV) pulse was removed 100 ns after the release of the primary electron from the cathode: electrons thus traveled slightly over 1 cm, and ions less than 1% of

this distance. By removing the electric field, the avalanche ceases to propagate in the gap, and the electrons eventually attach to gas molecules. It should be noted that in the cloud chamber, ions act as condensation nuclei for the supersaturated vapor; thus, at the moment the picture was taken, the droplets mark the locations of both attached electrons (negative ions) and positive ions. As pointed out by the author, the head of the avalanche appears rounded due to electron diffusion occurring in all directions;

- representation of the distortion of the external electric field E_0 in the gas gap due to the space-charge effect: the field is increased in front of the head and behind the tail (E_1 and E_3, respectively), while the opposite effect occurs between the electron and ion clouds ($E_2 < E_0$).

- avalanche in air at ∼0.4 atm, recorded as its size approached the Raether limit; its profile is no longer governed by thermal diffusion alone, but is strongly influenced by electrostatic repulsion among the electrons in the head.

Timing RPCs

A final note on tRPCs and the relevance of space-charge effects in operating these detectors at high gas gain while maintaining a low streamer probability. The current induced on a readout electrode by a single ionizing event can be written in the form [Rie03]:

$$i_{ind}(t) = Ae^{\alpha_{\text{eff}} v_e t}, \tag{3.15}$$

where A is the initial amplitude of the induced signal, varying from event to event due to statistical fluctuations in both cluster size and the initial avalanche growth. The ionic component has been neglected in the previous equation due to the much slower ion drift velocity, resulting in a considerably weaker induced current (see next subsection). Taking the natural logarithm of both sides of Equation (3.15) yields a linear expression in time:

$$ln(i_{ind}(t)) = \alpha_{\text{eff}}\, v_e\, t \;+\; ln(A). \tag{3.16}$$

The corresponding plot in Figure 3.7 allows for the following observations:

- the linearity highlighted by Equation (3.16) holds until the space-charge regime is reached. At that stage, the electric field in the avalanche becomes comparable to the external field. As a result, the multiplication rate decreases significantly, reducing the final avalanche size and ultimately preventing the Raether limit from being reached;

- the time to reach the discriminator threshold FEE_{th} is independent of the position of the initial ionizing event in the gap, providing excellent timing characteristics to these detectors. In turn, the discrimination level (if sufficiently low) does not affect the time resolution;
- the timing jitter depends on:
  - the variation of the initial current amplitude A, related to the statistical fluctuations mentioned above;
  - the current growth rate, which in turn depends on the effective Townsend coefficient α_{eff} and the electron drift velocity v_e;
- last but not least, the excellent timing properties of tRPCs are directly linked to the reduction of their gas gap to a few hundred micrometres. A smaller gas gap increases the reduced electric field E/N, and significantly enhances space-charge effects [Fon02b]. Another direct consequence of the reduced gap thickness is the increase in α_{eff} and v_e, as shown in Figure 3.5.

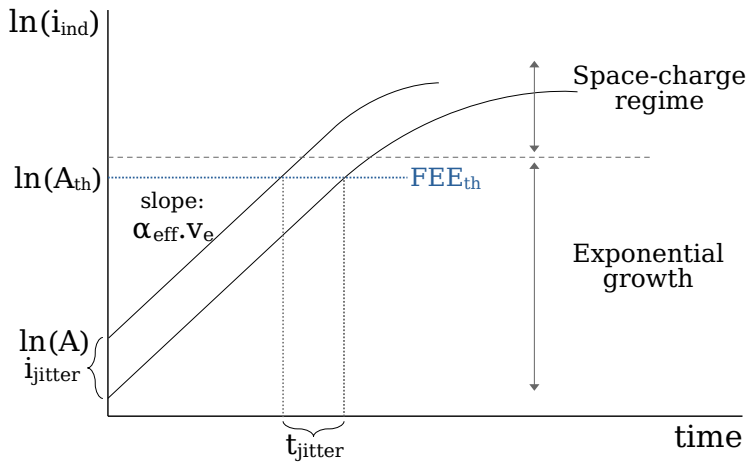

FIGURE 3.7: Illustration of the tRPC operating principle, highlighting the need for an initially high current growth rate ($\alpha_{\text{eff}}\, v_e$) to achieve very good time resolutions (below 100 ps), while the final sub-exponential growth is driven by space-charge effects. Adapted from [Fon02a, Abb18].

The current corresponding to a given discriminator threshold FEE_{th} can be expressed using Equation (3.15) as:

$$i_{ind}(t_{th}) = Ae^{\alpha_{\text{eff}} v_e t_{th}} = A_{th}. \tag{3.17}$$

By substituting A_{th} into Equation (3.16) and solving for t, one obtains:

$$t_{th} = \frac{1}{\alpha_{\text{eff}}\, v_e}\, ln\frac{A_{th}}{A}, \tag{3.18}$$

with t_{th} the time when the induced signal crosses the threshold level. Taking into account that the amplitude A is exponentially distributed around a mean amplitude, and considering the case of a single-electron cluster created somewhere in the gap, Riegler computed the time distribution for a given threshold and extracted the respective uncertainty, which corresponds to the intrinsic time resolution of the single-gap RPC:

$$\sigma_t = \frac{1.28}{\alpha_{\text{eff}}\, v_e}. \tag{3.19}$$

He concluded that the time resolution of the RPC depends on the effective Townsend coefficient and the electron drift velocity, but not on the threshold level – a result corroborated by both Monte Carlo simulations and experimental measurements [Rie03].

As a first-order approximation, Equation (3.19) was used to estimate the expected time resolution of the MRPCs tested in this work. The factor $1/\sqrt{n_g}$ was included in the equation to account for the number of gaps n_g in each detector. Taking as input the values presented at the beginning of this subsection (from Figure 3.5), the following results were obtained:

→ 259 ps σ, for the MRPC with E/N = 240Td (n_g=2, $\alpha_{\text{eff}} = 0.025$ µm^{-1}, v_e = 140 µm·ns^{-1})

→ 29 ps σ, for the tRPC with E/N = 380Td (n_g=6, $\alpha_{\text{eff}} = 0.090$ µm^{-1}, v_e = 200 µm·ns^{-1})

These results are broadly consistent to the experimental values listed in Table 5.4. An equivalent equation that also accounts for the efficient region of the gap (near the cathode) and avalanche statistics can be found in [GD17].

3.2.3 Signal Induction

As established by Ramo in 1939 [Ram39], the instantaneous current induced on a given electrode by the motion of a single electron is:

$$i^{-}_{ind} = e\, v_e\, E_w, \tag{3.20}$$

where e is the elementary charge, v_e the magnitude of the electron drift velocity $\vec{v}_e$ and E_w the component in the direction $\vec{v}_e$ of the electric field that would exist at the electron's instantaneous position under the following conditions:

i. electron removed;

ii. given electrode raised to unit potential (V_w=1);

iii. all other electrodes grounded (V_w=0).

The corresponding expression for an electron moving between two infinite parallel plates (see Figure 3.8) separated by a distance d is then given by:

$$\begin{aligned} i^-_{ind} &= e\, v_e\, E_w = e\, v_e\, \frac{V_w}{d} \\ &= \frac{e\, v_e}{d}. \end{aligned} \tag{3.21}$$

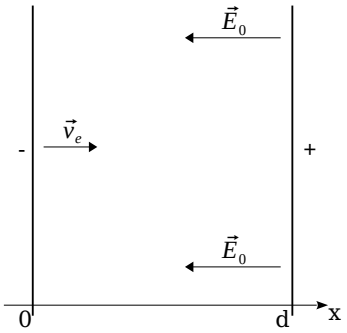

FIGURE 3.8: Electron emitted from the cathode of two infinite parallel plates separated by a distance d. The electron drifts along field lines defined by $\vec{E}_0$ with constant velocity $\vec{v}_e$, inducing a current $e\, v_e/d$ in the anode and a symmetric value in the cathode.

Following the approach of Raether [Rae64] in the analysis below, and assuming n_{e_0} electrons are released simultaneously from the cathode, their number increases exponentially due to successive ionizing collisions. Along the distance x, this growth is described by Equation (3.7), which can be rewritten as a function of time t:

$$n_e(t) = n_{e_0} e^{\alpha\, v_e\, t}. \tag{3.22}$$

The instantaneous induced current, resulting from the contribution of all electrons, increases accordingly. By including the total number of electrons at time t, the induced current becomes:

$$i^-_{ind}(t) = \frac{e\, v_e\, n_{e_0}}{d} e^{\alpha\, v_e\, t}. \tag{3.23}$$

The induction occurs until the electrons reach the anode, corresponding to the transit time $t_e = d/v_e$, i.e., for $0 < t < t_e$.

The positive ions, in turn, drift with velocity v_i from their point of creation toward the cathode. In this case, two time intervals must be considered: **(i)** the initial phase, corresponding to the ion buildup, which occurs only during the electron transit time ($0 < t < t_e$), and **(ii)** the subsequent period, lasting until all ions are collected at the cathode ($t_e < t < t_e + t_i$). Given that $v_i \ll v_e$, the ionic component of the induced current can be expressed as in Equation (3.24). Figure 3.9 shows the electronic and ionic components of the induced signal, as given by Equations (3.23) and (3.24), for an event reaching the Raether limit in a 1 mm gas gap.

$$\begin{cases} i^+_{ind} = \dfrac{e\, v_i\, n_{e_0}}{d} \left(e^{\alpha\, v_e\, t} - e^{\alpha\, v_i\, t} \right), & 0 < t < t_e \\ i^+_{ind} = \dfrac{e\, v_i\, n_{e_0}}{d} \left(e^{\alpha\, d} - e^{\alpha\, v_i\, t} \right), & t_e < t < t_e + t_i \end{cases} \tag{3.24}$$

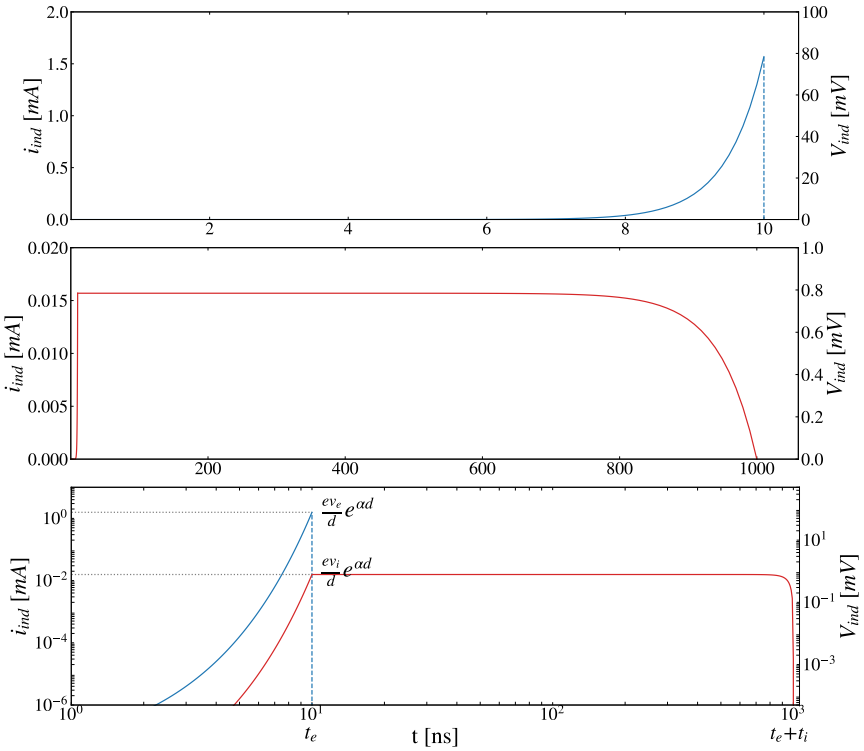

FIGURE 3.9: Current induced in the anode of two parallel plates, considering only the exponential growth of an avalanche initiated by a single electron ($n_{e_0} = 1$) from the cathode, for a gas gain of $e^{\alpha d} = \sim 10^8$. The following values were assumed: gas gap $d = 1$ mm, electron drift velocity $v_e = 100$ µm·ns^{-1}, and ion drift velocity v_i set to 1% of v_e. The top plot shows the electronic component of the induced current, the middle one the corresponding ionic component, and the bottom one combines both contributions in a log-log scale. The Y-axis on the right of each plot shows the corresponding voltage pulse if measured across a 50 Ω resistor.

The vectorial formulation of Equation (3.20), known as the Shockley–Ramo theorem [Sho38, Ram39], is given by:

$$i_{ind} = q\vec{v} \cdot \vec{E}_w. \tag{3.25}$$

where q is the charge of the drifting particle, $\vec{v}$ its instantaneous velocity, and $\vec{E}_w$ the weighting field.

The weighting field $\vec{E}_w$ is obtained by solving Laplace's equation for a given RPC geometry, with the readout electrode of interest set to unit potential (weighting potential V_w=1) and all others grounded (V_w=0), as discussed in Subsection 5.2.3. The induced charge on the electrode can then be computed by integrating $\vec{E}_w$ along the charge path, or equivalently by evaluating the difference in weighting potential V_w between the initial and final positions of the drifting charge, as shown in Appendix B.

It was seen that RPCs operate by relying on the exponential growth of charges drifting through the gas gap to induce signals on readout electrodes, such as strips or pads. It should be noted that these electrodes form the outermost layers of the detector. As pointed out by Santonico in 1981, signal induction is made possible by the fact that all layers between the gas gap and the strips – the resistive and HV electrodes – are transparent to these signals due to their high resistivity. This explains the use of high-resistivity materials, despite their impact on the detector's rate capability, which may be affected by charge accumulation on their surface.

4

Experimental Setup and Instrumentation

The experimental setup used to test the readout method developed in this work comprises three prototypes and one large-area detector, namely: **(i)** a simplified setup, consisting of a single MRPC with two 1 mm gaps and active area of 30×30 cm^2, **(ii)** a double-stack MRPC, each having the same number of gaps and area as the previous prototype, including also an additional FEE for timing measurements, **(iii)** the third configuration, composed of a double-stack tRPC with the same active area as previously, but with improved timing capabilities thanks to its thin multi-gap structure of six gaps 300 µm wide per stack, and **(iv)** the last setup including a double-stack tRPC equivalent to the previous configuration but of much larger area: 130×90 cm^2.

Before describing each setup, the subsequent Section 4.1 provides detailed information on the readout electrodes used to retrieve the induced signals generated by the RPCs, including the Printed Circuit Board (PCB) specially designed to decouple the number of FEE channels from the detector area. Afterwards, a comprehensive description of all the electronics used in this study, spanning from the FEE to the DAQ board, can be found in Section 4.2. The different prototypes and large-area detector are then described from Section 4.3 onwards.

4.1 Readout Electrodes

The readout electrodes, also known as pick-up electrodes[1], collect the current pulses induced by the passage of ionizing particles through the sensitive volume. The generated signals are then relayed to the FEE and subsequently, after amplification, to the DAQ board. The readout electrodes used with the prototypes and the large-area detector can be seen in Figure 4.1, and the detailed specifications of each board are given in Table 4.1.

(a) Thin-strip PCB (b) Wide-strip PCB (c) Ground plane

(d) Thin-strip PCB (e) Wide-strip PCB (f) Ground plane

FIGURE 4.1: Pick-up electrodes and ground planes used with the prototypes (top) and the large-area detector (bottom). All the strips are made of copper on top of a PCB substrate[2].

4.1.1 Thin-Strip Readout Electrode

The readout PCB shown in Figure 4.1a comprises 120 thin strips 1.54 mm wide, which are read out by charge-sensitive amplifiers that integrate the current pulses induced from

[1] the terms readout board and readout PCB are also used interchangeably throughout this document.
[2] Flame Retardant 4 (FR4) with a thickness of ∼1.5 mm (∼1.0 mm bakelite for the large-area detector).

	Thin-Strip PCB		Wide-Strip PCB		Ground Plane	
	Prototype	Large-Area	Prototype	Large-Area	Prototype	Large-Area
Length [mm]	360	1370*, 970†	380	1390	412	1420
Width [mm]	303.8	912.9*, 1339.6†	303	913	360	970
Strip number	120	360*, 528†	5	15	–	–
Pitch [mm]	2.54		61.0		–	
Interstrip [mm]	1	1.54	2		–	
FEE type	charge-sensitive preamps		current-sensitive preamps		–	
Measured quantity	charge		charge, time		–	
Extracted quantity	fine 1D position		coarse 2D position, event time		–	

* Longitudinal thin strips (aligned with the wide strips), providing a position along the X-axis.
† Transverse thin strips, providing a position along the Y-axis.

TABLE 4.1: Detailed information on the readout electrodes and ground planes used with the prototypes and wide-area detector: dimensions, type of preamplifiers connected to each board, physical quantities measured by the respective FEE and corresponding derived quantities.

both the electronic and ionic components of the avalanches. The readout board provides, via charge interpolation, the fine position in a single dimension, perpendicular to the strips. However, when using two pick-up boards, located below and above the detector, with the strips oriented in orthogonal directions, a 2D fine position is achieved. Moreover, as further detailed, to decrease the density of electronic channels, the 120 strips are not directly connected to the FEE, they first go through a PCB (see Figure 4.2) that reduces the number of channels by grouping several strips in parallel.

An equivalent thin-strip readout board was used with the large-area detector, with the primary change being the number strips: 360 for the longitudinal thin strips and 528 for the transverse ones (Figure 4.1d).

4.1.2 Wide-Strip Readout Electrode

Figures 4.1b and 4.1e show the readout boards, throughout this study referred to as 'wide-strip readout electrodes', which consists of five and fifteen large strips, each 5.9 cm wide, respectively. The wide strips are read out by current-sensitive amplifiers, providing time and charge measurements via the Time over Threshold (ToT) method, using only the electronic part of the induced signal. While only one end of the strips of the thin-strip boards are connected to preamplifiers, both ends of the wide strips are instrumented with electronics, enabling a two-dimensional measurement of the raw position of the events, along and perpendicular to the wide strips, as explaining in Subsection 4.2.4.

4.1.3 Ground Electrode

The output signal of the RPCs includes high-frequency components extending up to the GHz range due to the fast electronic component of the avalanches, which induces in the readout strips pulses lasting a few nanoseconds[3]. To maintain the integrity of the signal during its propagation along the strip lines, two ground planes, like the ones shown in Figures 4.1c and 4.1f, were positioned as close as possible to the thin-strip readout electrodes: one just below the thin-strip board located under the RPCs, and the second one above the thin strips located on top of the stack (refer to Sections 4.3 to 4.5 for a detailed description of the readout electrodes and ground plane positions in the different sub-setups).

The combination of the wide-strip readout electrode, an RPC, and a ground plane on the opposite side can be viewed as an Multiconductor Transmission Line (MTL) carrying signals up to microwave frequencies, with the RPC acting as an inhomogeneous dielectric. While the current pulses propagate along the strips, a return path must be provided as close as possible to the signal path to ensure effective signal transmission and limit both losses and distortion. The primary function of the ground plane is to provide the path of the return current flowing through the strips, just as with a coaxial cable, where the outer conductor serves as return path for the current passing through the inner conductor.

Although outside the scope of this document, a good signal integrity can be achieved when the cross-sectional geometry remains the same along the transmission line, maintaining a constant characteristic impedance of the line. Moreover, structures that interrupt the propagation of the electromagnetic fields along the current path (strips) and the return current path (ground plane) must be avoided since such disruptions could delay the signal transmission. In fact, in the setups where the time of the events was measured, the wide-strip readout board was located between two RPCs. With this arrangement, both detectors contribute to the induction of signals in the wide strips and in such case, two return paths must be provided for the reasons outlined above. The return path at the bottom of the stack could be done via the thin-strips themselves, given their alignment with the wide strips. In contrast, on the top of the stack the thin strips are oriented transversely relative to the wide strips. In this case, the presence of the ground plane above the thin strips provides a continuous path for the return current avoiding interruptions caused by the interstrip between the thin strips. Without ground plane, the electric field lines from the induced pulse in the wide strips would not have a defined termination point. They would spread out more broadly into the surrounding space, seeking other nearby conductive paths. The uncontrolled spread of electric and magnetic fields, in turn,

[3]time related to the collection of the avalanche electrons in a gas gap of the order of 1mm.

would lead to an increase of the signal degradation, namely with higher Electromagnetic Interference (EMI) levels and the crosstalk with nearby components and with other strips could be aggravated. Further details on the importance of a well-defined return path for the transmission of high-frequency signals can be found, for instance, in [Edw16]. For in-depth information on the signal propagation and the application of the MTL theory to the RPC case, where the current source occurs inside the strip itself, refer to [Fon13] and the references therein.

4.1.4 Signal Merging Printed Circuit Board

The 120 strips of the thin-strip readout electrodes used with the prototypes (Figure 4.1a) could be connected directly to 120 charge-sensitive amplifiers, allowing for submillimeter-resolution measurements of ionizing particle hits along one dimension within the sensitive area of approximately 30×30 cm^2. Using two orthogonally oriented thin-strip boards to retrieve the two-dimensional position of the events, the number of preamplifers would increase to 240. For larger detector areas, required for instance in High Energy Physics (HEP) and MST applications, the number of FEE channels would easily reach prohibitive values due to cost constraints. Indeed, knowing that the electronics is the driving cost of the detector, the density of FEE channels remains a prominent challenge and constraint for the construction of large RPCs.

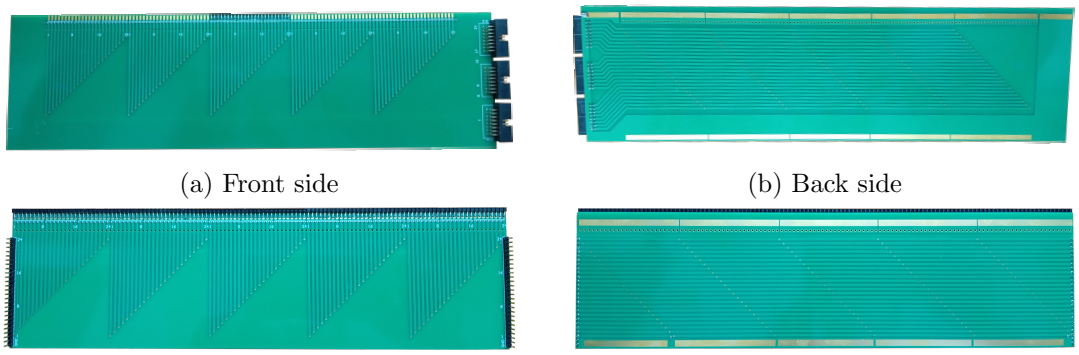

(a) Front side (b) Back side

(c) Front side (d) Back side

FIGURE 4.2: Signal Merging Printed Circuit Board (SMPCB) connecting thin strips in parallel before linking them to the FEE. Top: SMPCB used with the prototypes. Bottom: SMPCB with daisy chain links on both sides, designed for the large-area detector.

As an attempt to address the open issue raised in the previous paragraph, a new PCB was designed with the initial goal of keeping the number of electronic channels as low as possible when scaling up the sensitive area of the detector. With this board,

hereafter designated as SMPCB, the 120 thin strips, sequentially numbered from 1 to 24, are arranged into M=24 groups of N=5 strips wired in parallel (see Figure 4.2). The primary result of this codification is the reduction to one fifth the number of FEE channels needed to read out 120 strips (M channels for M × N strips), which can also be seen as enabling a 5-fold increase of the detector area, while keeping the number of channels unchanged.

The SMPCB routes signals from N strips into a single track, transmitting them to the respective electronic channel without any processing. With this approach, the sensitive area of the detector can be extended even further while maintaining the same number of preamps. This is accomplished by simply increasing the number of thin strips connected in parallel (N), as performed with the large-area detector described in Sections 4.6. Compared to the prototypes, N was increased from 5 to 15 for the thin-strip readout board with longitudinal strips (X) and from 5 to 22 for the board with transverse strips (Y) (shown in Figure 4.1d). In this way, despite the substantial increase in area, the same 24 preamps were employed for each dimension to read out the same 24 groups of thin strips, though each had additional strips connected in parallel. The SMPCB depicted in Figures 4.2c and 4.2d enables a daisy-chain arrangement for successive increases in N.

With the described technique of grouping together strips of the thin-strip readout electrodes, each channel of electronics reads out simultaneously several thin strips, leading inevitably to the following ambiguity: a current pulse arriving to a preamp could have been induced in any of the strips grouped in parallel. To determine in which strip the signal was in fact induced, the wide-strip readout electrode must be included to the setup. This additional readout board provides a coarse two-dimensional position of each interaction within the detector, allowing for the unequivocal identification of the strip where the interaction occurred, thus resolving the uncertainty created by the SMPCB.

A diagram showing the combination of all the previously mentioned readout electrodes can be seen in Figure 4.3. Each layer of strips was stacked vertically, with an RPC between each of them (see Sections 4.3 to 4.6 for a clearer view of the several layouts). The different readout boards depicted in Figure 4.3, from the bottom to the top, are:

- thin-strip readout electrode (X) with the strips connected to an SMPCB which reduces the number of channels to only 24 by grouping the strips in parallel. Each channel is afterwards read out by a charge-sensitive amplifier;

- wide-strip readout electrode with strips aligned to those on the first board. Both ends of the strips are connected to current-sensitive amplifiers. The board must be designed in such a way that the pitch of the wide strips corresponds approximately

to the width of the thin-strip set connected to separated electronic channels;

- second thin-strip readout electrode (Y), with the strips oriented perpendicularly to those on the previous boards. After passing through a second SMPCB, each channel is also fed to a charge-sensitive amplifier.

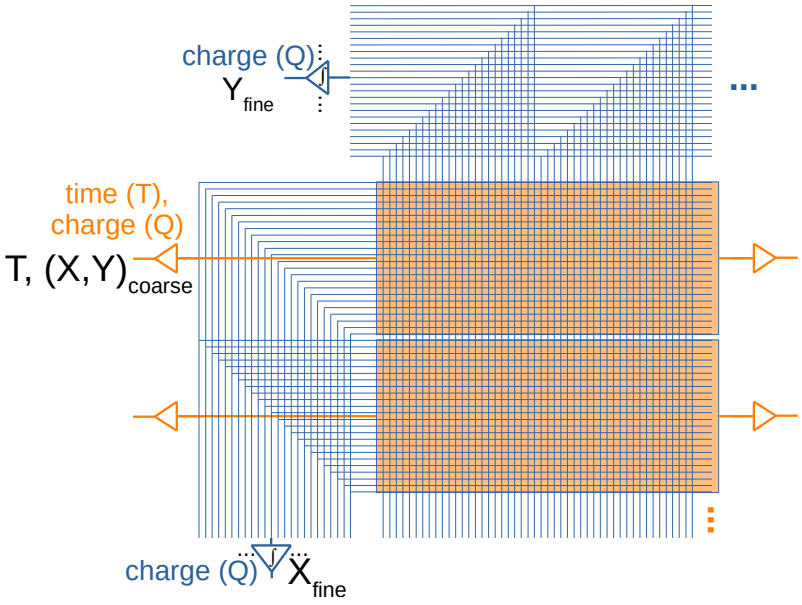

FIGURE 4.3: Schematic representation of the pick-up strips and the associated electronics. The thin strips (depicted in blue) are grouped in parallel with two SMPCB, one for each orthogonal direction. The wide strips that are used for disentanglement between groups of thin strips, are illustrated in orange. For the sake of simplicity, only two sets of 24 strips are represented for each thin-strip readout board.

4.2 Front-End Electronics

Two types of FEE were utilized in the present work: **(1) charge-sensitive amplifiers** connected to the thin-strip readout electrodes and used to integrate the induced current pulses over a few microseconds, corresponding to the time needed for both components of the generated ion-electron pairs to reach the respective resistive electrodes; **(2) current-sensitive amplifiers** for the readout of the wide-strip pick-up electrode, to simultaneously extract the time and charge of the events using only the electronic component of the avalanches. Both front-ends were connected to the DAQ board as illustrated by the block diagram in Figure 4.4, and described in the next subsections.

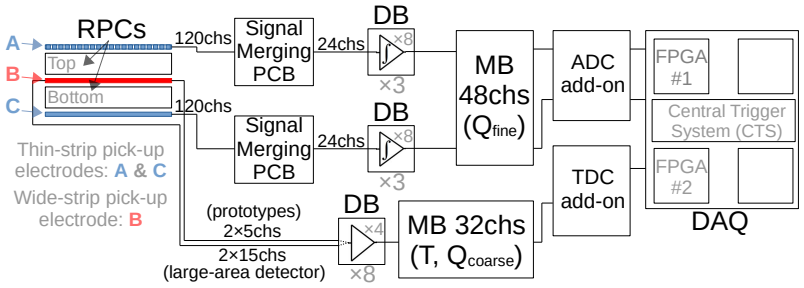

FIGURE 4.4: Full block diagram of the chain from the detector to the DAQ board.

4.2.1 DAQ & Add-On Boards

The DAQ system was based on the multi-purpose Trigger Readout Board - v3 (TRB3). Designed at GSI (Darmstadt, Germany), the TRB3 is a Field-Programmable Gate Array (FPGA)-based platform which includes: the Central Trigger System (CTS) unit with trigger and logic functionalities in the central FPGA, plus four peripheral FPGAs with a 32-channel Time-to-Digital Converter (TDC) implemented in each of them, featuring a RMS time resolution between two channels under 20 ps [Nei13]. The peripheral FPGAs provide flexible connectivity to modular expansion cards (add-on boards or simply add-ons) to ensure a wide range of applications. In this way, an Analog-to-Digital Converter (ADC) add-on[4], was connected to one of the peripherals for pulse analysis, as well as a TDC passive add-on for connectivity purpose to the respective FEE. Figure 4.5 shows the TRB3 and the add-on boards employed over the course of this work.

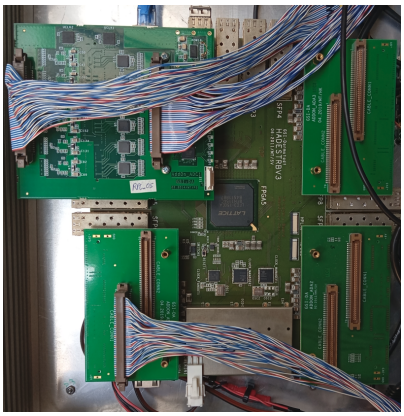

FIGURE 4.5: DAQ board (TRB3) with the peripheral FPGAs connected to an ADC add-on board (top-left) and three TDC passive boards.

[4]equipped with twelve 4-channel AD9219, featuring a resolution of 10 bits and sampling rate of 40 MHz. With a full-scale input range of 2 V peak-to-peak, the smallest change in input voltage that can be distinguished by the ADC AD9219 (Least Significant Bit (LSB)) is 2 V / 2^{10} = ∼1.95 mV.

4.2.2 Charge-Sensitive Amplifiers

The current pulses induced in the strips of the thin-strip pick-up boards were integrated using a custom-designed FEE which consists of six 8-channel Daughterboards (DBs) and a 48-channel Motherboard (MB) (see Figure 4.6). Each DB uses four bipolar operational amplifiers AD8599 (ultralow noise amplifiers with 10 MHz bandwidth) configured as integrators. An N-channel Junction Field-Effect Transistor (JFET) PMBFJ112 is used as part of the op-amp negative feedback loop and to regulate current flow based on the input signal, functioning as a voltage-controlled current source. The integration process extends over several microseconds, producing a voltage signal proportional to the total collected charge, which includes the charge induced from the movement of both carriers in the avalanches – electrons and ions. This FEE maximizes, in this way, the SNR and therefore enhances the resolution in computing the event position. The integration time constant was set to 100 µs, at least 10 times greater than the time required for the slower carriers to cross the gas gap[5]. After integration, the pulses were sent directly for digitization without further shaping, being digitally processed afterwards, as mentioned in the next subsection.

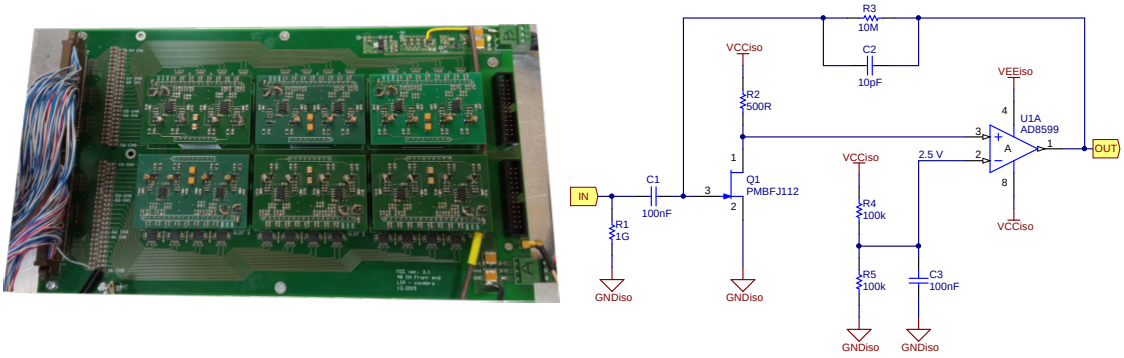

(a) Top view of the MB with 6 DBs. (b) Schematics of the integration stage.

FIGURE 4.6: Custom-designed FEE used to integrate the induced signals coming from the thin-strip readout electrodes.

As shown in the block diagram of Figure 4.4, the 48 charge amplifiers were connected to an add-on board equipped with 10-bit ADCs (see the previous section). Figure 4.7 provides two calibration curves performed for the corresponding signal path: the first curve correlates the input charge[6] at the entrance of the 48-channel MB with the voltage

[5] for an electron drift velocity around ∼100 µm/ns (see Subsection 3.2.2), electrons nead around 10 ns to traverse a gas gap of 1 mm (for common electric fields of 50-100 kV/cm); assuming an ion drift velocity 100-1000 lower, the last positive ions arrive a few microseconds later at the opposite electrode.

[6] measured using a capacitor of known capacitance (C_{in} = 1 pF) simulating the fast electronic part of the induced signal, and a resistor in parallel (R_{in} = 100 kΩ) for the ionic component. The total input

measured directly at its output (i.e., after the integration process), while the second one correlates the same input charge with the number of ADC bins obtained from the 10-bit AD9219 converters, at the end of the electronic chain.

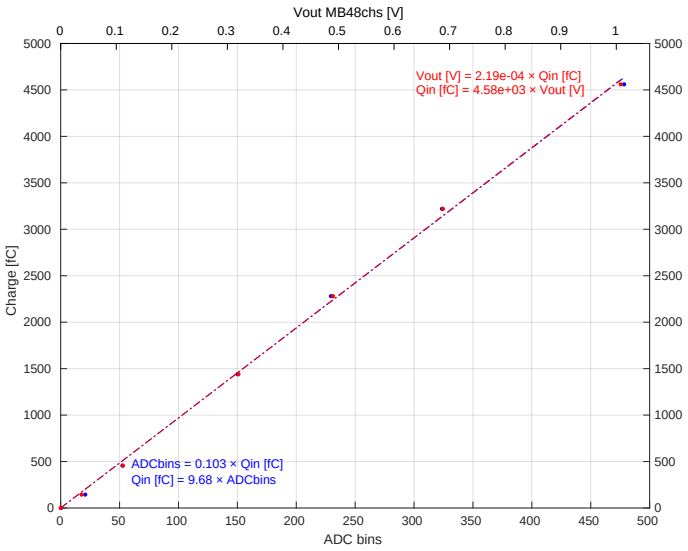

FIGURE 4.7: Calibration curves for the charge-sensitive amplifiers.

4.2.3 Digital Pulse Processing

To determine the amplitude of the analog pulses after amplification, 40 ADC samples were collected per signal waveform. With a sampling rate of 40 MHz and a downsampling[7] factor set to 32, the temporal window of each ADC waveform corresponds to 32 µs (800 ns/sample).

During the post-processing analysis, a digital filter algorithm was applied to measure the height of the waveforms relative to their baselines. The well known trapezoidal filter [Jor94] was selected because it effectively provides the signal amplitude[8] while attenuating the high-frequency noise. The trapezoidal filter can be easily implemented without requiring significant computing resources. It can be viewed as the subtraction of two moving averages, one on each side of a sliding window called the gap region G. The free parameters of the trapezoidal filter can be defined as follows:

charge is accordingly calculated from: $Q_{in} = Q_{1pF} + Q_{100k\Omega} = V_{in} \times C_{in} + V_{in} \times t/R_{in}$, where V_{in} and t represent the input voltage and duration of the provided input pulse, respectively.

[7] number of samples summed before storage in the buffer.

[8] the maximum value of the trapezoidal pulse corresponds to the signal amplitude with respect to the baseline, which in turn is proportional to the collected charge.

- L: the number of input samples used to compute each moving average, usually referred to as the 'length' of the moving average windows;
- G: the number of input samples in the gap region between the two average windows.

The output values of the digital filter are then obtained applying recursively the Equation (4.1) to the input waveform samples X. Given that the length of the filter window is 2L+G, the index k ranges from 2L+G to the last input sample.

$$Y_{trapezoidal} = \frac{1}{L}\left(\sum_{i=k-L+1}^{k} X_i \; - \sum_{j=k-2L-G+1}^{k-L-G} X_j\right) \tag{4.1}$$

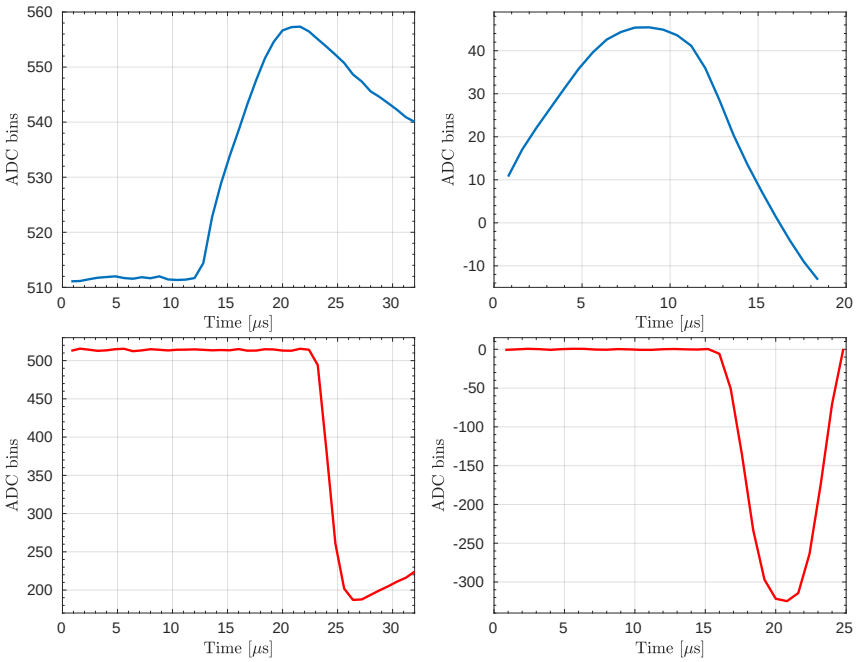

FIGURE 4.8: Top: on the left, the input waveform (0.8 µs/ADC sample) from an RPC with two 1 mm gaps, and on the right, the corresponding trapezoidal filter response using as parameters L=3 and G=12. Bottom: input waveform (left) and filter output (right) with L=3 and G=4, obtained from an RPC with six 0.3 mm gaps. For a processed waveform with amplitude of, for instance, approximately 320 ADC bins (10240 if including the downsampling factor of 32), and applying the calibration curve provided in Figure 4.7, the corresponding input charge is ∼3.1 pC ($Q_{in}[fC] = 9.68 \times 320$).

Two examples of input signals and the corresponding output responses of the trapezoidal filter are illustrated in Figure 4.8. Both waveforms were obtained using the RPCs

developed for the current work, which are further described. For the first waveform (positive polarity), the collection of charge extended over approximately 10 sample points, corresponding to a duration of ∼8 µs, in line with the expected time needed for the slower carriers to cross the 1 mm gas gap of the respective RPC[9]. On the other hand, the second one (negative polarity) has a sharper rise time, corresponding to an integration time of 4 µs. Indeed, in this second case, the RPC gas gaps have a width of only 0.3 µm.

For the measurements conducted throughout this work, the parameter G of the trapezoidal filter was set to twelve input samples, long enough[10] to cope with the different rise times. On its side, the number of points per average (parameter L) was limited to three input samples to avoid smoothing the signal over too long periods.

Finally, a set of scripts was developed from scratch to unpack and process the data files generated by the DAQ board, including all the ADC and TDC measurements.

4.2.4 Current-Sensitive Amplifiers

As previously mentioned, the thin-strip readout electrodes were instrumented with charge amplifiers to integrate the current pulses induced in the different strips. Precise spatial information in the transverse direction to the strips is then achieved through charge interpolation. The FEE connected to the wide-strip readout board, in turn, includes fast current-sensitive amplifiers providing timing information with a resolution below 35 ps (σ) [Bel10]. A measure of the collected charge in the strips is also obtained through the ToT technique, as detailed below.

Initially developed for the RPC-TOF of HADES experiment at GSI [Bel10], the FEE coupled to the wide strips consists of two types of boards: **(i)** up to eight 4-channel DBs, each with an analog and a digital stage, designed for negative input signals, and Low-Voltage Differential Signaling (LVDS) digital output carrying simultaneously the time and charge information of the events, and **(ii)** a 32-channel MB providing, among others, power and communication to the DAQ board, namely: the LVDS signal from each channel, the setting of the discriminator thresholds, and also a multiplicity output signal giving the number of firing channels, useful for trigger logic. Both FEE boards can be seen in Figure 4.9, including the block diagram of the amplification stage of a single DB channel.

As seen in the diagram of Figure 4.9, the input pulse is first amplified by the fast 2.1 GHz BGM1013[11] in order to deal with the fast component of the RPC signals[12]. After the

[9] As previously noted, assuming $v_{drift}^{ions} = \sim 10^4 - 10^5$ cm/s, the transit time of the ions through the gas gap should last up to 10 µs.

[10] 12 samples × 0.8 µs/sample = 9.6 µs

[11] a Silicon Monolithic Microwave Integrated Circuit (MMIC) amplifier with voltage gain of ∼35.

[12] for a pulse of a few nanoseconds generated by the electronic component of the avalanche, the signal

first level of amplification, the analog signal is routed into two branches: one for timing and the other for charge measurements. In the first path, the amplified signal follows directly to the high-speed MAX9601 comparator, which features a 500 ps propagation delay and latch enable (LE) functionality. If the pulse's amplitude exceeds the voltage threshold set in the comparator, it generates a digital signal which leading edge provides the time information of the event. The respective trailing edge is controlled by the comparator's latch enable, after a minimum delay (or width) of 50 ns to avoid the re-triggering of the comparator. On the second branch, the signal from the BGM1013 is integrated by the OPA690 operational amplifier configured as integrator with an RC time constant set to 40 ns. The output of the integrator is then connected to the comparator's latch disable (LE/) through a resistor, allowing for a ToT measurement using the integrated signal: depending on the integrated charge, more or less time is needed for the LE/ signal, during the discharge phase, to intercept the LE baseline[13], and when this occurs, the trailing edge of the digital output is generated. In this way, the comparator's latching time (i.e., the width of the output signal) is correlated with the collected charge, managing to encode in the same digital output pulse both the time and charge information. Additional details on the charge to width procedure can be seen in [Bel10].

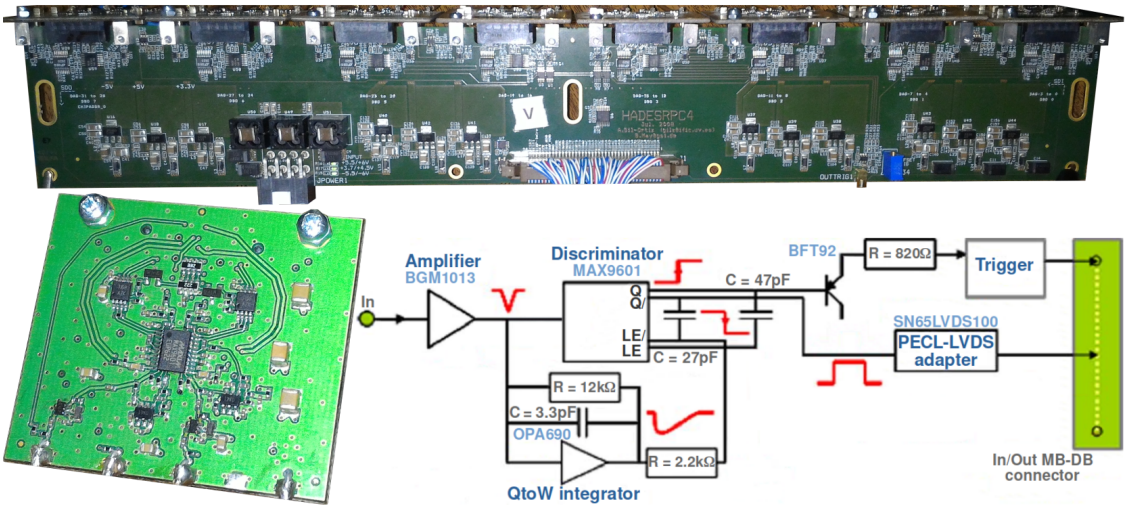

FIGURE 4.9: Top: MB with 8 DBs connected perpendicularly (located at the upper part of the picture) and used to amplify and digitize the analog pulses coming from the wide strips. Bottom: on the left, a DB with two amplification channels on each side of the PCB, and on the right, the block diagram of a DB channel. Adapted from [Bel10].

includes frequencies extending into the GHz range.

[13] the LE is also connected to an external DC level (not shown in the block diagram), corresponding to the charge to width threshold, used to adjust its baseline.

As Illustrated in Figure 4.4, the LVDS output of the FEE connected to the wide-strip readout board is routed to a TDC implemented in one of the peripheral FPGAs of the TRB3 board. At the end of the data chain the collected information from each TDC channel corresponds to the times of the leading and trailing edges of the received LVDS signals. Moreover, since both ends of the wide strips, referred to as the front (f) and back (b) sides throughout this work, were instrumented with the mentioned FEE, two quantities can be directly computed from the leading times: **(1)** the time of the event

$$T = \frac{T_f + T_b}{2}, \tag{4.2}$$

and **(2)** its longitudinal position[14] along the strips

$$Y = \frac{T_f - T_b}{2}. \tag{4.3}$$

The collected charge in each strip is also available using the leading and trailing times, as shown in Equation (4.4).

$$Q = Q_f + Q_b = (T_{trailing} - T_{leading})_f + (T_{trailing} - T_{leading})_b \tag{4.4}$$

Hence, the event position in the transverse direction to the wide strips (X-axis) is also known, given by the strip with the higher charge or through charge interpolation, as performed with the thin strips. However, because of the pitch of the wide strips (6.1 cm), the spatial information derived from the time measurements is, in this case, referred to as the raw or coarse position of the events.

Multiple calibrations are required before being able to use the time and charge information provided by this FEE, namely:

- **fine time**: the time measurement from each TDC channel on the DAQ board is performed using a fine time measurement block and two counters, the coarse and epoch counters, with granularities of 5 ns and 10.24 µs, respectively. In turn, the granularity of the fine time is not fixed and depends, among others factors, on the temperature. In order to achieve the temporal resolution of 20 ps, the fine time information of each channel must be calibrated measuring the lower and upper bin limits of the fine time during a run with enough statistics. While the lower bin value sets the offset for the temporal origin, the range of bins correlates with the maximum fine time duration of 5ns. Once the fine time has been calibrated for each channel,

[14] a position expressed in nanoseconds, which can be converted into length units, knowing the propagation velocity of the induced signal, as mentioned further.

the time of the event can be computed using: $T_{hit} = T_{epoch} + T_{coarse} - T_{fine}$. For the sake of exactness, the final event time is achieved subtracting a common temporal reference corresponding to the time of the trigger generated by the CTS (based on the required logic) and called 'reference time': $T_{event} = T_{hit} - T_{refTime}$. Further details can be obtained directly from the TRB3 manual [GSI].

- **Y position**: as previously mentioned, the longitudinal position along the wide strips is obtained by subtracting the measured leading times at both strip extremities. Depending, for instance on the path length of the signals, that may vary from strip to strip, a positional offset must be computed in order to have the wide strips centered at the midpoint of the Y-axis. It is then added as a constant k to Equation (4.3): $Y = k + (T_f - T_b)/2$. Taking into account all the event positions obtained along one strip, given by definition in units of time (ns), and knowing the length of the induced region[15], the propagation velocity of the induced signal along the wide strips can be determined. The value of 171 mm/ns was obtained and used throughout this study.

- **event time**: as in the preceding point, to compare times from different wide strips, an equivalent offset must be included in Equation (4.2): $T = k' + (T_f + T_b)/2$.

- **charge pedestal**: the minimum charge required to trigger the discriminator must be aligned to a common reference point to enable the comparison between values from different channels. As previously mentioned, a minimum signal length of 50 ns is applied between the leading and trailing edges of the lowest pulse amplitude firing the MAX9601 discriminator in the FEE. An additional stretching is applied at the level of the peripheral FPGA, resulting in an approximate duration of 80 ns for the lowest measured charge. Each TDC channel has its own pedestal, whose value must be subtracted in Equation (4.4) before applying the calibration curve to convert the charge units from nanoseconds to Coulombs: $Q = Q_f + Q_b - Q_{pedestal}$.

- **charge**: Figure 4.10 shows the charge calibration curve that relates the charge[16] injected at the entrance of a DB channel to the corresponding width of the LVDS signal ($T_{trailing} - T_{leading}$).

[15] limited by the shortest length of the: strip, gas gap or conductive layer where the HV is applied.

[16] measured as with the charge-sensitive amplifiers, using a capacitor of known capacitance and a parallel resistor to simulate both the electronic and ionic components of the induced signal.

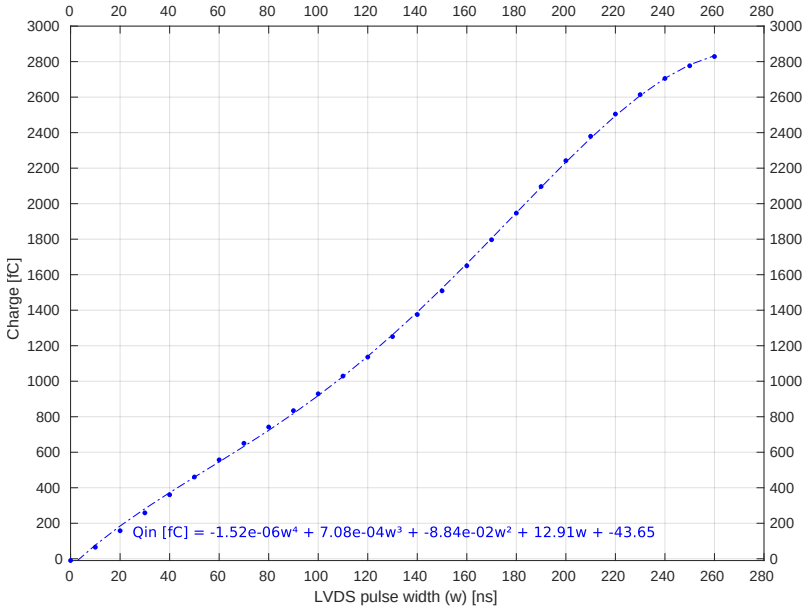

FIGURE 4.10: Calibration curve for the current-sensitive amplifiers.

4.3 Single MRPC Prototype

The first prototype consists of an MRPC with two gas gaps 1 mm wide, separated by three float glass electrodes 2 mm thick and with bulk resistivity ρ in the order of $10^{12}\,\Omega.cm$ (see Figure 4.11). The outermost resistive electrodes are coated with a resistive paint of surface resistivity[17] R_s around $10^7\,\Omega.sq^{-1}$, with a twofold purpose: to increase the conductivity of the outer surface and to facilitate connections to the High-Voltage Power Supply (HVPS). Resistive and HV electrodes are confined inside a closed Polypropylene (PP) box with 1mm-thick walls and feedthroughs for gas and HV supply.

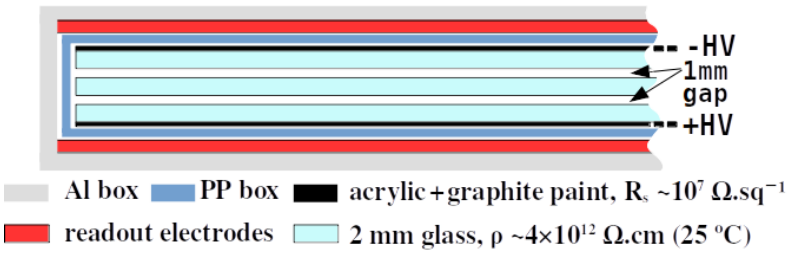

FIGURE 4.11: Layer diagram of the MRPC used in the 1st prototype.

[17] while the bulk resistivity ρ comes with the unit $\Omega.cm$, the surface resistivity R_s is usually given in ohm per square: Ω/sq or $\Omega/\square$; the relationship between both quantities can be expressed as: $R_s = \rho/t$, where t is the sheet or film thickness in centimeters.

The approach of using PP for the encapsulation of the sensitive volume was tested for the first time in 2021-2022, as reported in [Sar23a]. This study highlights the excellent water vapor and atmospheric gas blocking properties of the PP that enabled the operation of an MRPC of almost 2 m^2 with an ultra-low gas flux consumption around 1 $cm^3/min/m^2$ (one volume exchange each 1.5 days).

Directly in contact with the external walls of the PP box are the bottom and top thin-strip readout electrodes (see Sub-section 4.1.1), each constituted by 120 copper strips with a 2.54 mm pitch and interstrip of 1 mm, on top of a PCB substrate 1.4 mm thick (see Figure 4.12). When a ionizing particle passes through the detector, the charge induced in the thin strips are transmitted to the FEE via an SMPCB specially designed to reduce the number of channels from 120 to one-fifth of this value, as described in Sub-section 4.1.4. Moreover, since the strips of the bottom and top readout PCBs were aligned in the same direction, the present prototype could only measure the position of the crossing particles in one direction (transverse to the strips). At last, the MRPC was installed inside an aluminium enclosure for robustness purpose while aiming to minimize external EMI.

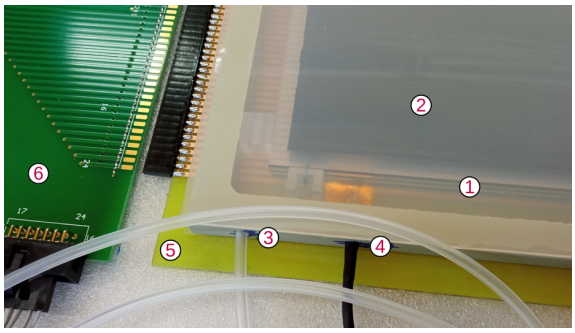

FIGURE 4.12: Detailed view of the MRPC illustrating: the resistive electrodes inside the PP box (1) and the top resistive layer (2) (painted using the airbrush technique), the gas (3) and HV (4) feedthroughs, the bottom readout electrode (5) with a partial view of the 120 strips, each measuring 36 cm in length. Part of the SMPCB (6) is also visible on the left side of the picture.

The detector was flushed with 1,1,1,2-tetrafluoroethane[18] ($C_2H_2F_4$) in open gas loop, with a flux around 30 $cm^3/min/m^2$.

Based on the HV scan shown in Figure 5.1, and in order to reach an efficiency close to 100%, the nominal HV of the MRPC was set to ± 6.0 kV, corresponding to an electric field in the gas gaps on the order of 60 kV/cm[19].

[18] also known as R-134a or Freon 134a, among many other denominations.

[19] E_{gap} = V/d = 2 × 6.0 kV ÷ (2 gaps × 0.1 cm/gap).

4.4 Double MRPC Prototype

With the second prototype, the wide-strip readout PCB along with a second MRPC, were added to the detector stack, as depicted in Figure 4.13. A detailed view of the stack layers can be seen in Figure 4.14.

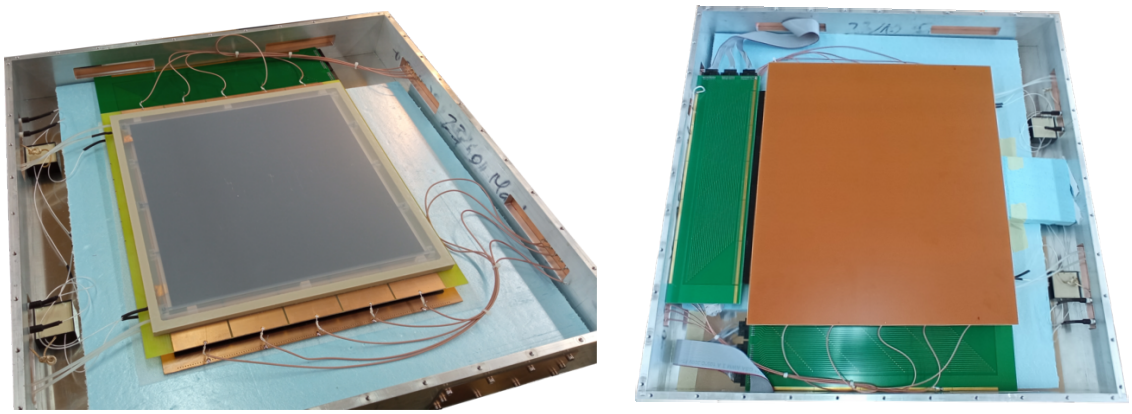

(a) (b)

FIGURE 4.13: (a) Stack of two MRPC with the ground plane at the top of the stack removed for better visibility of the underlying layers. (b) Full configuration, including thin-strip readout electrodes and ground planes bottom and top. Two SMPCBs grouping together the thin strips transversely oriented are also visible in the image.

The introduction of the wide-strip readout PCB implies using an additional FEE, making this configuration somewhat more complex, however, the benefits are twofold: **(1)** the new readout board resolves the ambiguity raised by adding thin strips in parallel, by providing an additional 2D positional information of the interactions in the detector (as described in Sub-section 4.1.4), and **(2)** it also enables the measurement of the time of events, useful for TOF applications.

In the arrangement depicted in Figure 4.13a, ground electrodes were used without thin-strip readout electrodes with the purpose of evaluating the impact of the presence of discontinuities (the interstrips in the thin-strips readout boards) in the return path of the current pulses induced in the wide strips, as first introduced in Sub-section 4.1.3. The results are presented in the next chapter.

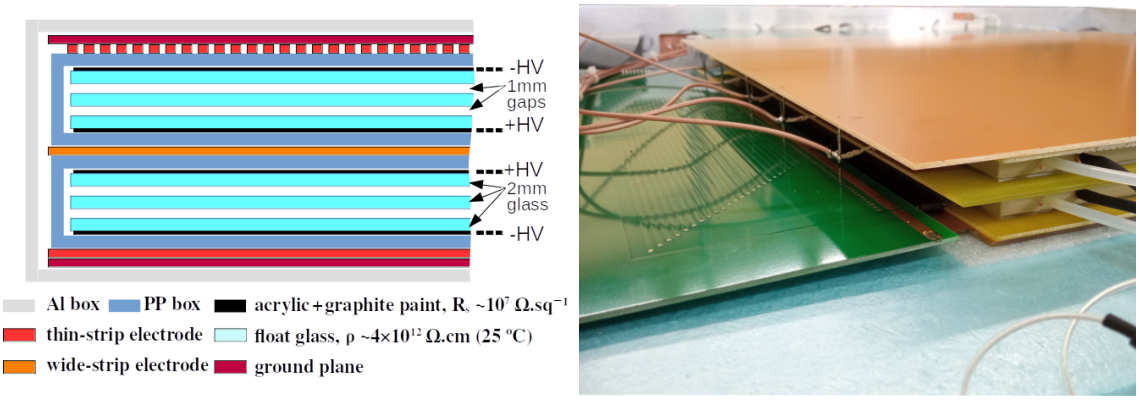

(a) Layer diagram with two MRPCs.

(b) Close-up of the stack layers.

FIGURE 4.14: Layer diagram and stack layer view of the 2nd prototype. The thin strips at the bottom of the stack are aligned with the wide strips at the center; in turn, the thin strips on the upper readout board are transversely oriented with respect to the previous ones.

The operational parameters used in this setup were the same as those in the previous one, namely in terms of the provided gas and its respective flux. In turn, as an attempt to keep the detector gain[20] constant during acquisition runs that could last more than a month, the HV was dynamically adjusted every 15 minutes, as a function of the atmospheric pressure and temperature, in accordance with the following Equation (4.5):

$$HV = \frac{E/N \cdot d_{gap} \cdot P}{k \cdot T}, \tag{4.5}$$

with E/N being the reduced electric field expressed in Townsend[21] (Td), d_{gap} the total gas gap thickness in centimeters, k a constant ($\sim$0.01381 $mbar \cdot cm^3 \cdot K^{-1}$), P and T the local atmospheric pressure and temperature given in millibars and Kelvin, respectively. Refer to Appendix A for further details. The nominal reduced field was fixed at 240 Td, corresponding to an HV similar to the one applied in the previous setup (see Figure 5.1).

A final remark to highlight that due to the polarity[22] of the electronics connected to the readout electrodes, the HV was configured to position the anodes[23] at the center of

[20] a constant gas gain $e^{\alpha d}$ can be achieved trying of stabilize the first Townsend coefficient (α), which in turn depends on the reduced electric field (E/N); d being the gas gap thickness, E the electric field strength (constant for parallel plate geometries) and N the gas number density (the number of molecules or atoms per unit volume as mentioned in Subsection 3.2.1). In the context of the ideal gas law, the gas number density can be written as $PV = nk_BT \Leftrightarrow N = n/V = P/k_BT$ (n denoting the total number of particles; V, P and T the corresponding gas volume, pressure and temperature; and k_B the Boltzmann constant).

[21] $1\,Td = 10^{-17}\ V \cdot cm^2$ (see Subsection 3.2.2).

[22] bipolar for the FEE connected to the thin strips and negative for the related to the wide strips.

[23] positive HV electrodes, where the avalanche electrons migrate.

the stack (see Figure 4.14a), hence inducing negative pulses into the wide strips.

4.5 Double tRPC Prototype

The rationale behind this third configuration was to extend the detector's timing capabilities and evaluate the possibility of using the novel SMPCB in applications requiring high time resolution (below 100 ps (σ)). The improvement with this setup is therefore related to the detector itself, migrating from MRPCs to tRPCs, i.e., to detectors specially designed for precise measurements of time. The following design and operational requirements (not necessarily an exhaustive list) must be fulfilled in order to potentially achieve a time resolution close to the state-of-the-art[24]:

- the tRPC must be operated with a high gas gain, achieved by raising the reduced electric field E/N; the applied HV increases accordingly, as given by Equation (4.5);
- the charge carrier production is controlled by narrowing the gas gap width to a few hundred micrometers, which in turn decreases the local voltage drop across the gaps. A beneficial side effect of reducing the size of the gas gaps is therefore an increase in the counting rate capability of the tRPC (lower time to recover from the local partial discharge effect), however at the expense of reducing the induced charge[25];
- the number of gaps might have to increase since smaller gaps leads to a lower probability of primary ionizations, contributing to an efficiency loss. A tRPC is therefore also an MRPC, but the reverse is not necessarily true;
- increasing the number of gaps (and consequently the number of resistive electrodes) as an attempt of generating more avalanches has nevertheless the downside effect of increasing the distance between readout electrodes (reduction of the weighting field $\vec{E}_w$). As a result, the induced charge on the readout electrodes decreases, contributing also to an efficiency loss. A possible approach is to reduce the glass thickness which, in turn, has some drawbacks, particularly with regard to the detector robustness and the increased challenges in the assembly process;
- by operating the detector at a higher gas gain, additional care must be taken with the gas mixture. The number of streamers must be controlled adding for instance a few percents of sulfur hexafluoride (SF_6) to the mixture, avoiding in this way

[24] for tRPCs, a few tens of picoseconds [Fon00, An08].

[25] reduction in the number of clusters, and thus in the number of charge carriers in the gas gaps, results in smaller induced pulses on the pick-up electrodes.

the disruptive effects of such discharges in the sensitive volume (e.g. the efficiency loss related to the localized drop in HV on the anode because of the accumulation of electrons from the streamers). The mechanism by which the SF_6 significantly reduces streamers is related to its relatively high electron affinity (see Subsection 3.2.2), as described here [Cam98, Abe00]. Another quenching[26] gas frequently added (but not in the current setup), this time to suppress Ultraviolet (UV) photons produced during the streamer phase, is the isobutane (methylpropane (C_4H_{10})) due to its high-absorption UV coefficient. The isobutane keeps the avalanches confined to a spatially limited zone by preventing the formation of secondary discharges related to the production of photoelectrons[27] [Abb18].

For comparison, the changes listed below were made in order to migrate from the MRPCs of the previous setups to the tRPCs used in the current one:

- the width of the gas gaps was reduced from 1 to 0.3 mm;
- the number of gas gaps per RPC was increased from 2 to 6;
- the thickness of the resistive electrodes was reduced from 2 to 1.1 mm;
- the reduced electric field E/N was raised from 240 to ∼380 Td, thereby achieving an efficiency close to 100%, in line with the previous MRPCs, and a percentage of streamers of a few percent, as discussed in the next chapter;
- the applied HV increased from approximately ±6 kV (∼6.0 kV/gap, ∼60 kV/cm) to around ±8.5 kV (∼2.8 kV/gap, ∼94 kV/cm), being dynamically adjusted every 15 minutes, as previously performed;
- the provided gas mixture was changed from pure Freon 134a to 95.5% only with 4.5% of SF6. A significant gas flux was used (above 250 $cm^3/min/m^2$) due to a hardware limitation of a mass flow controller.

Figure 4.15 provides additional details on the various stack layers in this arrangement with tRPCs.

[26] the term quenching is used here to denote the process of reducing the growth of electrical discharges, even if its primary action is on electrons rather than photons.

[27] free electrons created inside and outside the avalanches, by UV photons in turn produced during the de-excitation of atoms and molecules; these UV photons have enough energy to produce further ionizations.

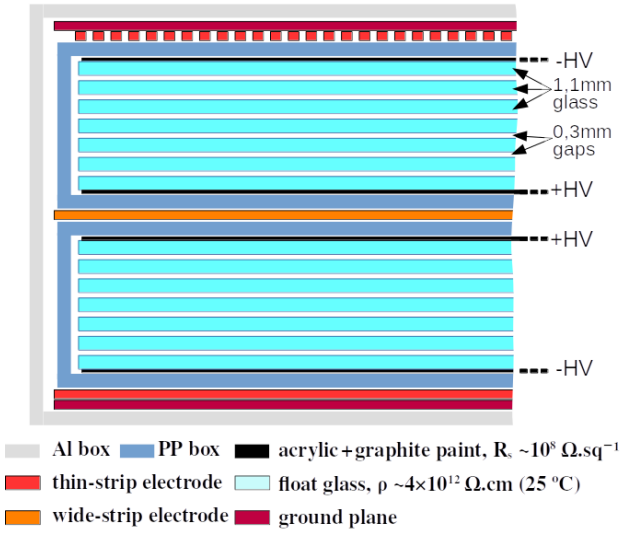

FIGURE 4.15: Layer diagram of the 3rd prototype which includes two tRPCs.

4.6 Large-Area Double tRPC

The fourth and last setup features tRPCs with a sensitive area of 130×90 cm^2 (see Figure 4.16), 13 times larger in area than the previous prototypes. Taking advantage of the developed codification that decouples the required number of FEE channels from the readout area, the instrumentation of these large tRPCs required only 20 additional preamplifiers, despite the considerable increase in the number of thin strips: from 240 to 888 (see Table 4.2).

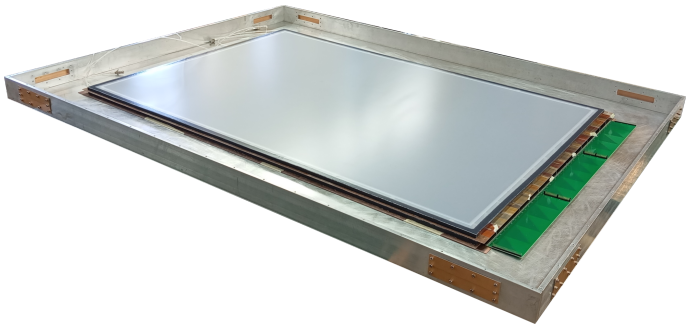

FIGURE 4.16: Partial view of the large-area detector. At the bottom of the stack: three SMPCBs connected in a daisy-chain configuration, creating 24 groups of 15 thin strips wired in parallel (360 longitudinal thin strips in total); the wide-strip readout board is also visible just below the top tRPC. The thin-strip readout board and ground plane located at the top of the stack were removed for better visibility of the underlying layers.

	Thin-Strip Readout Boards				Wide-Strip Readout Boards			
	Thin Strips		FEE channels		Wide Strips		FEE channels	
	Long.*	Trans.†	Long.	Trans.	Long.	Trans.	Front	Back
Prototype tRPCs	120	120	24	24	5	–	5	5
Large-Area tRPCs	360	528	24	24	15	–	15	15

* Long.: longitudinal
† Trans.: transverse

TABLE 4.2: Summary of the number of strips and FEE channels for the different setups and readout boards. Despite the significant increase in area from the prototypes to the large-area tRPCs (13 times larger), only 10+10 new preamps were needed to readout 10 additional wide strips, corresponding to a 1.3-fold increase of FEE channels (from 58 to 78).

While the layer diagram depicted in Figure 4.15 also applies to the large-area tRPCs, its reduced electric field was set to 360 Td (∼2.7 kV/gap, ∼90 kV/cm), slightly below the value set for the smaller tRPCs. Refer to Section 5.1 for additional details.

Finally, owing to the change in the gas system from the previous configuration, the gas flux was significantly reduced to only 20 $cm^3/min/m^2$, with the mixture adjusted to 99% of Freon 134a and 1% of SF6.

5 Experimental Results

This chapter assesses how the previously described codification, based on SMPCBs, affects the detector performance. To this end, the chapter addresses three main operational parameters: the detector's efficiency and its resolution in both position and time, with each aspect discussed in a dedicated section. When possible, a comparison is made between the different setups tested in this work. The correct and unequivocal reconstruction of particle hits within the detectors is also assessed by producing 2D reconstruction maps of the projected images of scintillators used for external triggering. Details of these reconstructed maps are further evaluated.

5.1 Efficiency

Most often, including for the measurements of detector efficiency, the MRPCs and tRPCs were operated during days or weeks with cosmic rays, using a coincidence trigger generated externally by two plastic scintillators[1] (Bicron BC420) located directly above and below the detector plane. A trigger generated by the RPCs themselves, referred to as self-trigger mode[2], was occasionally used to evaluate their background counting rate,

[1] parallelepipeds 8×3×2 cm^3, each coupled to two Photomultiplier Tubes (PMTs) Hamamatsu H6533. The trigger required a coincidence among the four PMTs within a 5 ns time window.

[2] trigger generated by the coincidence of at least one channel on both ends of the wide strips.

i.e., the rate of self-generated signals occurring over the whole sensitive area even in the absence of external ionization, also known as dark count rate [Abb18].

As previously mentioned, the electronic chain connected to the thin strips consists of charge-sensitive amplifiers relaying the integrated signals to 10-bit ADCs in the DAQ board. The ADCs digitize the analog pulses at a 40 MHz sampling rate (one sample taken every 25 ns) and 32 samples are summed up (downsampling) before being stored in the buffer. As a result of the digitization process, the data stream ends-up with one sample every 25×32=800 ns per FEE channel, consisting of discrete values ranging[3] from 0 to $2^{10}-1$, with the baseline positioned at the center of the scale (see for instance Figure 4.8).

For both thin-strip readout boards, the total charge per event is determined by summing the charges (amplitude of the post-processed waveforms) collected from all 24 electronic channels connected to the corresponding readout board via an SMPCB. An event where all channels register only noise inevitably produces a certain charge, corresponding to the sum of the amplitudes of waveforms caused by the electronic noise around each baseline. A total charge threshold must therefore be established, below which a coincidence trigger indicates that a ionizing particle was detected by both scintillators but the RPCs failed to identify it, contributing to the inefficiency measured by the respective readout PCB.

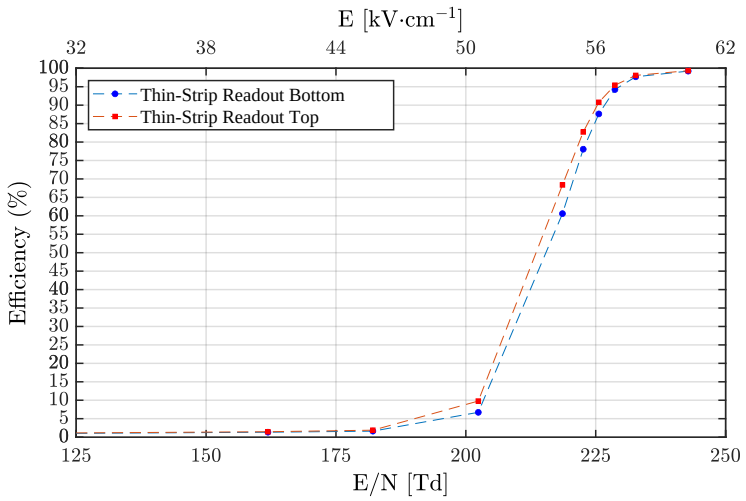

FIGURE 5.1: MRPC efficiency (single MRPC prototype) measured with the thin-strip readout electrodes bottom and top, as a function of the reduced electric field (E/N) expressed in Townsend (Td) (lower X-axis). The related field values are provided in kV·cm^{-1} on the upper X-axis.

For the detection efficiency shown in Figure 5.1 the total charge threshold was set to an average value of 2–3 ADC bins per channel (∼25 fC/ch). Finally, the efficiency was

[3] from 0 to $(2^{10}-1)\times 32$ when accounting for the downsampling factor of 32.

computed for each readout board, as the ratio of the number of events seen by the MRPCs to the total number of coincidences[4].

An equivalent HV scan performed for the tRPCs is shown in Figure 5.2. In this case, the efficiencies achieved with both the thin and wide strips are reported. It should be noted that in the present configuration, with the wide-strip readout PCB located at the center of the stack, both RPCs induce signals on the wide strips. On the contrary, the signals in each thin-strip readout board are induced from the closest RPC only. Therefore, the fact that both RPCs contribute to the signal induction in the wide strips helps to counterbalance a possible lack of sensitivity, since the FEE connected to these strips only uses the electronic part of the induced signals (see Section 4.2).

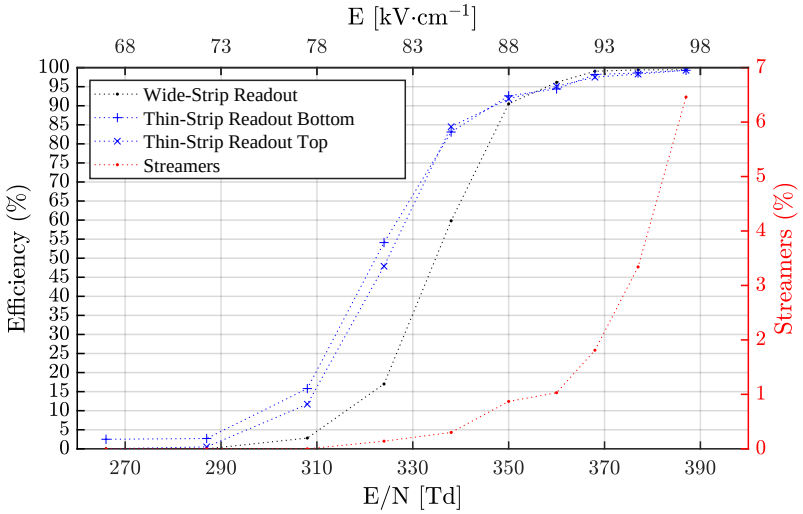

FIGURE 5.2: tRPC efficiency (30×30 cm^2 prototype) obtained from the wide- and thin-strip readout electrodes. The percentage of streamers is shown on the right-hand Y-axis.

As outlined earlier, a total charge threshold of around 2–3 ADC bins per channel was set for the signals induced in the thin-strip readout electrodes. In turn, for the wide-strip readout electrodes, the charge threshold is established directly at the beginning of the electronic chain (see for instance Figure 4.9), with the MAX9601 discriminator threshold having been set at -40 mV. In this way, only a pulse with negative polarity and amplitude above 40 mV (∼23 fC/ch[5]), coming from a wide strip, can generate an LVDS signal in the respective electronic channel. Here, to state that the RPCs detected the ionizing particle that triggered the scintillators, at least one digital pulse[6] must have been recorded in

[4]requiring detection by all four PMTs, to significantly reduce the probability of random coincidences.

[5]obtained using Equation (5.16), with the BGM1013 amplifier (amplification factor ∼35 V/V, 50 Ω input impedance) upstream the discriminator, and assuming a pulse duration of 1 ns.

[6]the leading and trailing times of the signal.

both the front and back sides of the detector. Having both the leading and trailing edges of the LVDS pulses enables the computation of the charge of the induced signal via the ToT method, as described in Subsection 4.2.4, which in turn allows the rejection of pulses generated by capacitive crosstalk[7], as these pulses are characterized by having zero charge.

The percentage of streamers obtained using the double tRPC prototype is also plotted as a function of the reduced field in Figure 5.2. The streamer level – above which the charge of an event, computed as shown in Equation (4.4), is considered a streamer – was set to 100 ns, i.e., ∼1 pC according to the calibration curve provided in Figure 4.10 (approximately 10 times greater than the charge collected from a typical avalanche).

Finally, the reduced field was chosen throughout this work to achieve efficiencies close to 98% with all tested RPCs. As an exception, the large-area detector was operated with an efficiency around 94–95% to limit the percentage of streamers, which was initially significantly high (above 20%). This percentage of streamers gradually decreased, reaching a value close to 6% after two month of operation. Nevertheless, the reduced field was kept constant over the entire campaign to avoid altering the detector's gain. The high efficiencies presented in this section indicate that the readout method based on SMPCBs does not affect the RPC efficiency, as the measured values ($> 95\%$) are consistent with the typical performance expected for this type of detector.

5.2 Spatial Resolution

The spatial resolution[8] of an RPC, i.e., its ability to precisely determine the position of ionizing events, can be subdivided into two main contributions:

$$\sigma^2_{x\_total} = \sigma^2_{x\_FEE} + \sigma^2_{x\_detector}, \tag{5.1}$$

where σ_{x_FEE} represents the contribution from the readout electrode and the attached FEE, while $\sigma_{x\_detector}$ corresponds to the component associated with the detector itself[9], i.e., the stacked layers inside the detector.

Two independent positional measurements were preformed with the setups tested in this work, namely the fine position obtained from the thin-strip readout PCBs and the coarse position from the wide-strip readout PCB. The resolutions achieved with both measurements, related to the first component of Equation (5.1), are described in the

[7] signals induced by capacitive coupling between the strip carrying the primary signal and surrounding strips.

[8] evaluated throughout this document by the standard deviation of the corresponding distribution.

[9] due to statistical fluctuations of the processes occurring in the gas gaps, e.g.: primary ionization and avalanche development.

next two subsections. In turn, the usual approach to include the detector component is using a residual-based method, which requires at least three detector planes[10] arranged vertically, in a configuration often referred to as telescope or tracker since it allows to reconstruct particle trajectories. Given that only one detector was available in each setup tested throughout this work, the residuals approach could not be applied, however, the component related to the detector is known to have a small contribution to the total resolution. Based on previous works with similar multi-gap RPCs (e.g. [Bla12]), one can assume this contribution to be well below 100 µm.

5.2.1 Transverse to the Thin Strips

In a simple binary readout system, the electronics registers whether a strip was hit (1) or not (0). The event position is then estimated at the center of the fired strip. Assuming that only one strip fires per event, the hit positions can be modeled by a continuous uniform distribution over the pitch width. The PDF of this uniform distribution (Equation (5.2)) is shown in Figure 5.3.

$$f(x) = \frac{1}{p}, \quad for \quad -p/2 \leq x \leq p/2 \tag{5.2}$$

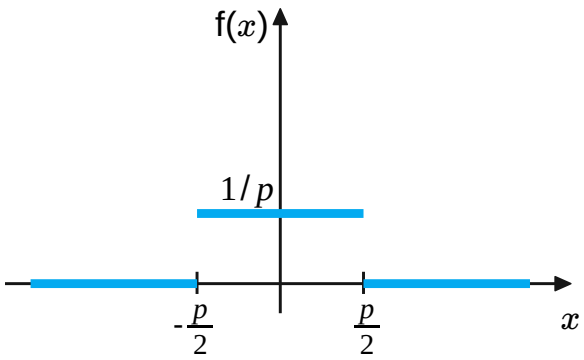

FIGURE 5.3: PDF of a uniform distribution across the strip pitch (p), corresponding to the probability density of hit positions within the fired strip of a binary readout system.

Let X be the continuous random variable representing the position of the particle hits, assumed to be uniformly distributed over the pitch width. Its variance can then be computed using Equation (5.3).

[10] for each event, a linear fit is performed using the measured positions from all but one plane; all the fitted positions at the missing plane are then subtracted from the measured hits, yielding the residuals. The standard deviation of the residuals distribution provides an estimate of the detector resolution.

$$\sigma_X^2 = E[X^2] - E[X]^2 \tag{5.3}$$

The first and second moments of X are derived in Equations (5.4) and (5.5), respectively.

$$E[X] = \int_{-\infty}^{+\infty} x f(x)\, dx \;= \int_{-p/2}^{p/2} x \frac{1}{p}\, dx \;= 0 \tag{5.4}$$

$$E[X^2] = \int_{-\infty}^{+\infty} x^2 f(x)\, dx = \int_{-p/2}^{p/2} x^2 \frac{1}{p}\, dx \;= \frac{p^2}{12} \tag{5.5}$$

The spatial resolution of the binary readout system, obtained by combining the previous results, is expressed by Equation (5.6).

$$\sigma_X = p/\sqrt{12} \tag{5.6}$$

This result shows that the resolution of the readout electrode is related to the size of its segmentation. It also sets an upper bound for the resolution that would be achieved if the induced signal were not shared across multiple strips. For the thin-strip readout electrodes, with a pitch of 2.54 mm, the contribution to the spatial resolution from the readout electrode alone would be around 0.730 mm, and ∼17.6 mm for the wide-strip electrodes with a 61 mm pitch.

If charge sharing occurs over multiple strips, the spatial resolution can be significantly improved using interpolation techniques such as charge centroiding. The default charge-sharing model used in this work is the centroid algorithm, which estimates the event position by computing the weighted average of the positions of the strips with induced charge, as shown in Equation (5.7).

$$x_{event} = \frac{\sum (x_i \cdot Q_i)}{\sum Q_i} \tag{5.7}$$

The weighting factor (Q_i) corresponds to the collected charge in each strip, while x_i is the central position of the respective strips. Other interpolation methods tested for reconstructing the image of scintillators projected onto the RPCs are presented in Subsection 5.2.3.

To assess the effective spatial resolution achieved by applying the centroid algorithm to the thin-strip readout electrodes, the single MRPC prototype was used. As mentioned in Section 4.3, in this setup the strips of the bottom and top thin-strip electrodes were aligned in the same direction, allowing the interaction point to be measured twice along this axis, once on each electrode. The distribution of the difference between both measurements for

each event provides insight into the spatial resolution of the thin-strip readout electrodes, as explained next. The position measurements are obtained from two independent readout electrodes, with strips connected to separate electronic channels. However, the induced signals originate from the same MRPC. As a result, the standard deviation obtained from the difference in positions measured by both readout electrodes excludes common noise contributions from the detector[11] and any systematic error. Therefore, the obtained standard deviation corresponds only to the contribution from the readout electrodes and their associated FEE.

Based on the formula for the propagation of uncorrelated errors (Equation (5.8)) and assuming equal contributions from both position measurements, the uncertainty in each individual measurement adds in quadrature, as shown in Equation (5.9).

$$\sigma^2_{f(x)} = \sum_{i=1}^{n} \left(\frac{\partial f(x)}{\partial x_i} \right)^2 \sigma^2_{x_i} \tag{5.8}$$

$$\sigma_{\Delta x} = \sqrt{\sigma_x^2 + \sigma_x^2} = \sqrt{2} \cdot \sigma_x \tag{5.9}$$

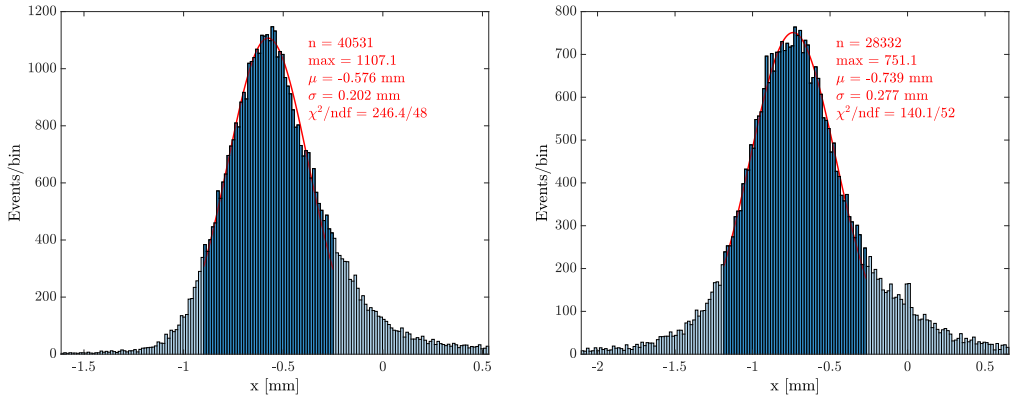

(a) (b)

FIGURE 5.4: Distributions of position differences measured by both thin-strip readout electrodes with strips oriented identically: (a) with only 24 thin strips connected to the FEE; (b) with all the strips connected to the electronics (24 groups of 5 strips wired in parallel).

Figure 5.4a shows the distribution of position differences obtained from both thin-strip readout electrodes, when each electronic channel was connected to only one strip, i.e., before grouping strips in parallel[12]. A second run was performed after connecting all

[11] explaining why the detector's contribution to the spatial resolution must be obtained using a residual-based method, as previously explained.

[12] only 24 out of the 120 strips of the thin-strip readout electrodes were connected to the respective

the thin strips to the FEE. The resulting distribution is shown in Figure 5.4b.

As stated in Equation (5.9), the contribution from each readout electrode, including the respective FEE, is obtained by dividing the total spatial resolution of the distributions given in Figure 5.4 by $\sqrt{2}$. By doing so, a deterioration in spatial resolution from 143 to 196 µm was observed when connecting five thin strips instead of only one to the same electronic channel. An expected degradation, as extending the strip length or adding more strips in parallel leads to a higher input capacitance (see below). This increase in capacitance directly affects electronic noise[13]: the output noise of the preamplifier scales approximately linearly with the input capacitance [Leo94], degrading the SNR and, consequently, the spatial resolution, as observed experimentally.

Capacitance Measurements – Single MRPC Prototype

The capacitance C of parallel plates varies directly with the area A and inversely with the plate separation d, following:

$$C = \varepsilon \frac{A}{d}, \tag{5.10}$$

where ε is the permittivity of the dielectric.

An increase in charge collection area, due to joining strips in parallel, should therefore proportionally increase the total capacitance. This was verified by measuring the capacitance of a thin strip for both previously mentioned configurations, namely: **(i)** the run with a 1:1 ratio between the number of electronic channels and thin strips (connecting only 24 strips to each SMPCB), and **(ii)** the run with 1:5 ratio, i.e., with 5 parallel strips per channel (connecting all 120 strips to each SMPCB). The same methodology was applied in both cases: the capacitance was measured using a high-precision capacimeter[14] between a thin strip of the top readout electrode and the aluminium case at the bottom of the stack. Thus, the ground represents one of the capacitor plates being measured, while the second plate corresponds to one or five thin strips of the readout electrode linked to the corresponding SMPCB. Moreover, the dielectric of the capacitor is mainly composed of glass and freon, corresponding to the MRPC at the center of the stack (see Figure 4.11).

Based on the averaged values listed in Table 5.1, the capacitance of the readout system increased by a factor of ∼1.9 due to the transition from one to five thin strips per electronic

SMPCB. The remaining strips were grounded to prevent electrical isolation, which could lead to unwanted charge accumulation.

[13] random fluctuations superimposed on the detector signal.

[14] Vitecom 75-VA501.

	1 strip per preamp	5 strip per preamp	ratio
Top readout electrode + SMPCB	86 ± 3 pF	165 ± 11 pF	1.9 ± 0.1
Top readout electrode only	18 ± 4 pF	97 ± 11 pF	5.4 ± 1.3

TABLE 5.1: Average capacitances obtained with the single MRPC prototype, comparing values with a single strip vs. five strips per electronic channel. The second row shows values after subtracting SMPCB and cable contributions (68 ± 3 pF), which are common to both configurations.

channel. However, these values include contributions from the SMPCB and the connection cable to the FEE, which were also measured, yielding a total average of 68 pF for both contributions after disconnection from the readout electrode. After subtracting the SMPCB and cable components, a final capacitance ratio of ∼5.4 was obtained, consistent with Equation (5.10) and the 5-fold increase in strip area.

Evaluation of Electronic Noise – Single MRPC Prototype

The electronic noise was also compared between the two previously described configurations. One way to evaluate noise is to quantify fluctuations in the waveforms of integrated pulses obtained at the end of the electronic chain, i.e., after ADC digitization. The first 10 of 40 ADC samples were averaged to compute the baseline level of the waveforms, corresponding to the first 8 µs[15] of the 32-µs window, as described in Subsection 4.2.3.

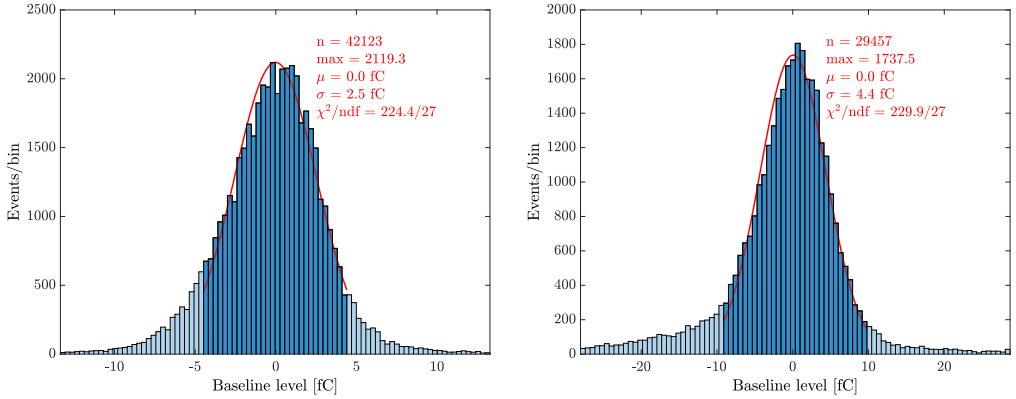

(a) (b)

FIGURE 5.5: Baseline distributions of one channel of the 48-channel MB. The baseline levels were evaluated from the first 10 samples of the ADC waveforms: (a) with only 24 thin strips connected to the FEE; (b) with all the strips connected to the electronics (24 groups of 5 strips wired in parallel).

[15] 10 samples x 25 ns/sample x 32 (downsampling).

	1 strip per preamp	5 strip per preamp	ratio
Average baseline noise [fC]	2.5 ± 0.8	4.9 ± 0.9	2.0 ± 0.7

TABLE 5.2: Baseline noise obtained with the single MRPC prototype, averaged over all channels of the 48-channel MB. The comparison is made between values for a single strip vs. five strips per electronic channel.

The spread of the baseline level, quantified by the standard deviation of the corresponding distribution, provides an indication of the electronic noise in the system. As an example, Figure 5.5 shows the baseline distributions of the first channel of the 48-channel MB, when connected to only one thin strip (5.5a) and to five thin strips (5.5b).

As illustrated in Figure 5.5, the standard deviation of the baseline distribution increased by a factor of ∼2 due to the transition from one to five thin strips per electronic channel. This increase matches that observed for the total capacitance of the readout system (Table 5.1) and is consistent with the approximately linear relationship mentioned above between electronic noise and capacitance. Finally, the overall electronic noise of all 48 channels was quantified by averaging the standard deviations of their baseline distributions. This resulted in a similar increase of a factor of ∼2 between the two configurations (see Table 5.2).

Spatial Resolution vs. Charge Range

As seen previously, for the configuration with only one thin strip per electronic channel, a spatial resolution of 143 µm could be achieved using the centroid method, representing a significant improvement over the value (730 µm) obtained from Equation (5.6) for a binary readout system with the same strip pitch. It was also observed that a larger strip area leads to higher electronic noise, degrading both the SNR and the spatial resolution of the readout system.

An increase in strip pitch would reduce the number of FEE channels but inevitably lower the final spatial resolution. Conversely, increasing the signal amplitude improves spatial resolution, at least to a certain extent. This is illustrated in Figure 5.6, where the spatial resolution is plotted against event charge.

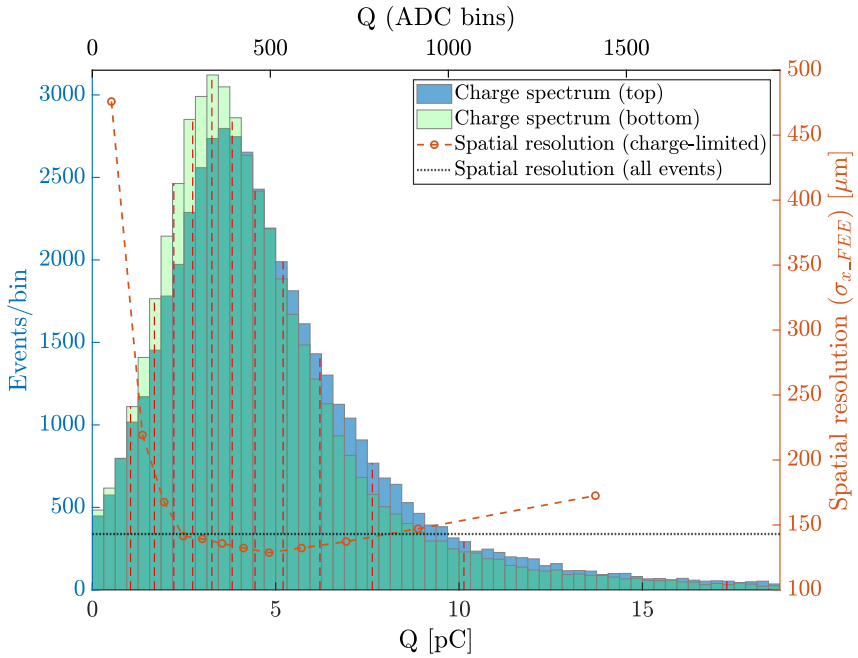

FIGURE 5.6: Spatial resolution as a function of the event charge. Left axis: charge spectra of top and bottom thin-strip readout electrodes obtained with the single MRPC prototype, with each electronic channel connected to a single strip; right axis: spatial resolution obtained from position difference distributions, computed for several charge ranges. The charge boundaries (vertical dashed lines) were chosen to ensure approximately 2000 events per interval[16]. The horizontal dotted line corresponds to the previously mentioned 143 µm resolution, achieved without charge restrictions.

The figure shows that events with lower charge lead to significantly worse spatial resolution due to the deterioration in SNR. On the other hand, for higher charge values, spatial resolution worsens again, though at a lower rate. This trend might be related to charge buildup, ultimately leading to streamer formation and broader induced signals.

Evaluation of Electronic Noise – Large-Area Detector

As done previously with the single MRPC prototype, the electronic noise of the large-area detector was evaluated by computing the fluctuations in the ADC waveforms of the induced signals in the thin-strip PCBs. Figure 5.7a shows, as an example, the baseline distribution of the first channel of the 48-channel MB. Its standard deviation aligns with the average value obtained from all 48 channels connected to both thin-strip electrodes: 22.7 ± 2.5 fC. This baseline noise result corresponds to an increase by a factor of approximately 4.6 compared to the value obtained with the smaller prototype, where five strips

[16] all events must satisfy the charge restriction for both the top and bottom readout electrodes.

were connected per preamplifier (see Table 5.2).

The increase in baseline noise of the large-area detector was also compared to the expected rise in capacitance of each thin strip. The capacitance was therefore measured between a thin strip of the top readout electrode and the ground below the top tRPC. A value of 1700 ± 30 pF was obtained, 10 times higher than the 165 pF measured with the single MRPC prototype (see Table 5.1). The capacitance scaled approximately with the increase in detector area, which is 13 times larger than the prototypes[17]. The baseline noise, in turn, increased at a slower rate, rising by approximately half as much as the capacitance.

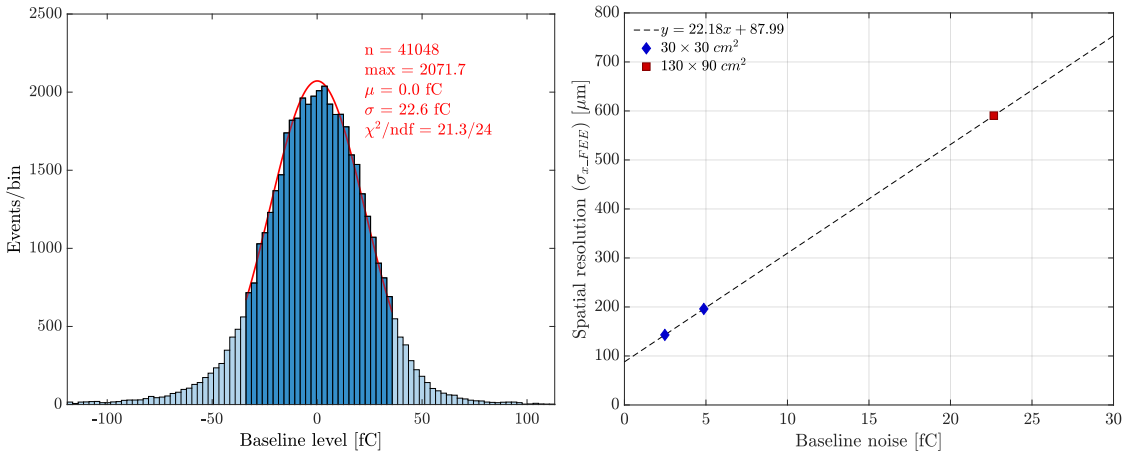

(a) (b)

FIGURE 5.7: (a) Baseline distribution of one channel of the 48-channel MB for the large-area detector. (b) Rough estimate of the spatial resolution of the large-area detector, assuming a linear relationship with electronic noise.

Earlier in this subsection, the impact of the thin-strip readout electrodes and their FEE on spatial resolution was evaluated for both a single strip and five strips connected in parallel. Assuming a linear relationship between the spatial resolution of the readout electrodes and the electronic noise, this result from the smaller prototype can be used to extrapolate the same quantity for the large-area detector. This is shown in Figure 5.7b, where two spatial resolution (σ_{x_FEE}) measurements of the single MRPC prototype were used to establish the assumed linear relationship with electronic noise. For a baseline noise of 22.7 fC obtained with the large-area detector, the expected spatial resolution should therefore be slightly below 600 µm.

[17] the large-area detector is 13 times larger than the smaller prototypes (130×90 cm^2 vs. 30×30 cm^2), but the SMPCB contribution is also included in the measured capacitance, and this contribution increased by only 5 times, as 5 SMPCBs were used in a daisy chain with the top readout electrode.

The results reported in this subsection, comparing areas, capacitances, electronic noise, and spatial resolutions between setups, are summarized below:

i) 1 strip vs. 5 strips connected to each FEE channel in the single MRPC prototype:

- the ratio of areas for charge collection increased by a factor of 5 when only the top readout electrode is considered. Including the area of a strip from the SMPCB (always present, whether 1 or 5 thin strips are connected per FEE channel), the total area increased only by a factor ∼2.4;
- the measured capacitance followed this increase in area: factors of ∼5.4 and ∼1.9 for the top readout electrode only, and when the SMPCB is also included, respectively;
- the electronic noise of the baseline increased by a factor of ∼2.0 (SMPCB included);
- in turn, the spatial resolution degraded by only a factor of ∼1.4, which was interpreted as a linear relationship between spatial resolution and baseline noise, including an initial offset as shown in Figure 5.7b.

ii) single MRPC prototype (with all strips connected to the electronics) vs. large-area detector:

- the ratio of areas between detectors increased by a factor of 13; measuring the exact strip area yields an increase of ∼9.4 (SMPCBs included);
- the measured capacitance followed this increase, being ∼10 times higher than that of the prototype;
- the electronic noise of the baseline increased by only a factor of ∼4.6, about half the increase in capacitance and detector area.
- in conclusion, the spatial resolution of the large-area detector was estimated to be around 600 µm, based on the linear relationship previously established with the MRPC prototype.

5.2.2 Longitudinal to the Wide Strips

Effect of Pulse Rise Time on Spatial Resolution

As discussed earlier in Subsection 4.2.4, the longitudinal position of an event along the wide strips is computed by subtracting the times measured at both strip ends (Equation (4.3)). The spatial resolution achieved with this time subtraction is therefore detector-independent, at least to some extent. Any time fluctuation from the detector itself is

subtracted, as it is common to both measurements (in a similar way to the subtraction of positions mentioned in the previous subsection), leaving only the contribution of the wide-strip readout electrode and the respective FEE (the σ_{x_FEE} term of Equation (5.1)). However, a second-order effect can be considered: the electronics' contribution decreases for signals with a sharper rise time. In fact, due to random fluctuations, signals with the same amplitude will usually not cross the discrimination threshold (leading-edge triggering) at the same time. As shown in Equation (5.11), this timing jitter σ_{time}, caused by electronic noise, increases with the amplitude of the fluctuations σ_{noise} and is inversely proportional to the slope of the signal dV/dt at the triggering point [Leo94].

$$\sigma_{time} = \frac{\sigma_{noise}}{\left|\frac{dV}{dt}\right|} \tag{5.11}$$

Induced signals with sharper rise times lead to more precise triggering, reducing the impact of electronic noise on timing jitter: the faster the rise time, the smaller the timing jitter[18]. This can also be seen in Figure 5.8, where projecting the amplitude of the signal fluctuations onto the horizontal time scale yields the corresponding fluctuations in time.

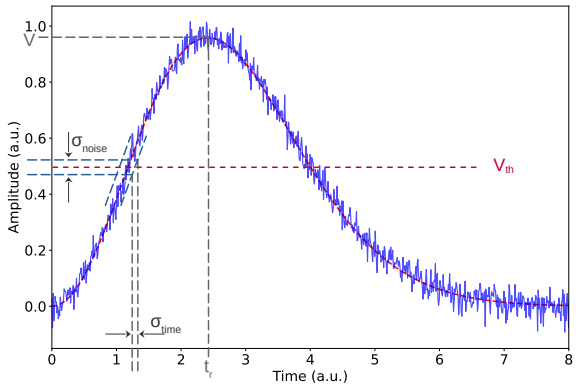

FIGURE 5.8: Timing jitter σ_{time} caused by electronic noise σ_{noise} in a generic pulse. The timing error depends on the slope of the signal at the discrimination threshold V_{th}.

To operate the double tRPC prototype and the large-area double tRPC, the reduced electric field was significantly increased compared to that of the previous MRPC prototypes. This increased the detector gain and the drift velocity of charge carriers, consequently increasing the slope of the leading edge of the induced pulses in these timing detectors (see Figure 5.9). As mentioned above, the same FEE was then less affected by timing jitter when used with tRPCs, ultimately enhancing spatial resolution along the

[18] while timing jitter occurs even for pulses of equal amplitude, the walk effect introduces timing inaccuracy due to the variability in pulse amplitude. This effect will be introduced in Section 5.3.

wide strips (obtained through the subtraction of times, as also previously mentioned). This could explain the removal of 'ghost images' in the 2D reconstruction of the scintillators, which were only visible along the wide strips with the double MRPC prototype, as discussed in Subsection 5.2.3.

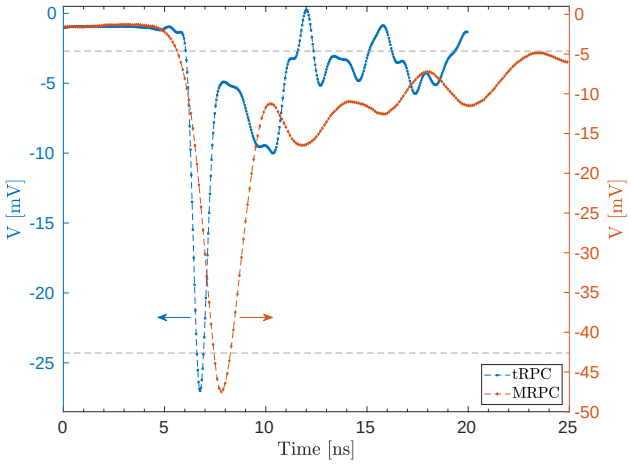

FIGURE 5.9: Comparison of the induced signals obtained with MRPCs and tRPCs, amplified[19] directly at the detector output. The primary ionizations originated from 0.511 MeV and 1.275 MeV gamma rays from an Na-22 source placed above the detector to enhance the event rate. The negative pulses (averaged over 500 pulses) were induced in a wide strip by the electronic component of the avalanche as it moves toward the anode. The signal induced by the ionic component moving in the opposite direction is not visible on this time scale. The rise times of the MRPCs and tRPCs, measured from 10% to 90% of the pulses amplitude (horizontal dashed lines), are 1.9 ns and 0.56 ns, respectively.

The slope of the induced signal in Equation (5.11) can be roughly approximated as:

$$\frac{dV}{dt} \approx \frac{\Delta V}{\Delta t} = \frac{V}{t_r}, \tag{5.12}$$

with V being the positive pulse amplitude and t_r the total rise time (0%–100% of V), as shown in Figure 5.8. Substituting this result into Equation (5.11), an approximate formula for timing jitter as a function of the total rise time and SNR (V/σ_{noise}) is obtained:

$$\sigma_{time} \approx \frac{\sigma_{noise}}{\frac{V}{t_r}} = \frac{t_r}{SNR}. \tag{5.13}$$

Based on Figure 5.9, the rise time t_r is around 1 ns (0%–100% of V) for the tRPCs and approximately three times higher for the MRPCs. The random fluctuations can be estimated at around 1–2 mV[20], resulting in an SNR of approximately 25–50 and a rough

[19] using a BGA2712 MMIC amplifier with flat 21 dB gain up to 2.6 GHz (voltage gain of ∼11).

[20] from the observation of the averaged pulses of Figure 5.9, an upper value of the fluctuation is around

timing jitter estimate on the order of a few tens of picoseconds for the tRPCs (20–40 ps), and three times this value for the MRPCs. The value obtained with the tRPCs is in line with the expected FEE time resolution of 35 ps (see Subsection 4.2.4).

Effect of Top Ground Plane Removal on Induced Signal

As mentioned in Subsection 4.1.3, both the top and bottom RPCs contribute to signal induction in the wide strips, while the ground planes above and below the thin strips provide the return paths for these induced signals. The entire structure of the double MRPCs or tRPCs can be roughly seen as two transmission lines (more precisely two MTLs) stacked one above the other: the bottom one extends from the bottom ground plane to the wide-strip readout electrode, while the top transmission line spans from the wide strips to the top ground plane.

A comparison of induced signals measured directly at the detector output was made using the double tRPC prototype with and without the top ground plane. One tRPC was turned off at a time to check whether the absence of the ground plane affected signal propagation from both detectors in the same way. Figure 5.10 shows the amplified signals averaged over 500 pulses. By changing the horizontal scale of the oscilloscope[21] from 2 to 400 ns/division, it was possible to visualize the fast and slow components of the signals. Each subfigure includes an inset showing a zoomed-in region of the signals. Based on the observation of the different pulses, it can be concluded that without the top ground plane:

- the induced signals exhibited increased pulse width and fluctuations, with the latter especially visible in the ionic component of the signal;
- signals from both the top and bottom tRPC were affected, but the impact was greater on the signal from the top tRPC.

While beyond the scope of this thesis, for a lossless transmission line the phase velocity v_p is given by Equation (5.14), where L and C are the inductance and capacitance per unit length, respectively. In turn the characteristic impedance of the transmission line, also neglecting losses, is given by Equation (5.15). [GD11, Edw16, Leo94]

$$v_p = \frac{1}{\sqrt{LC}} \tag{5.14}$$

$$Z_0 = \sqrt{\frac{L}{C}} \tag{5.15}$$

$0.1 \times \sqrt{N}$ mV, yielding ∼2 mV for N = 500 measurements.

[21] 1 GHz bandwidth 10 GSa/s oscilloscope (TDS7104 Tektronix).

The signal degradation after removing the top ground plane was evident, resulting in wider pulses and some degree of temporal desynchronization between the signals from both tRPCs. As a first-order explanation, removing the top ground plane increased the distance to the nearest ground reference, thereby reducing the capacitance to ground of the top transmission line. As a result, the phase velocity increased, causing signals from the top detector to propagate faster than those from the bottom detector. Additionally, the increased fluctuations in the ionic component are likely caused by signal reflections due to the change in characteristic impedance after removing the top ground plane.

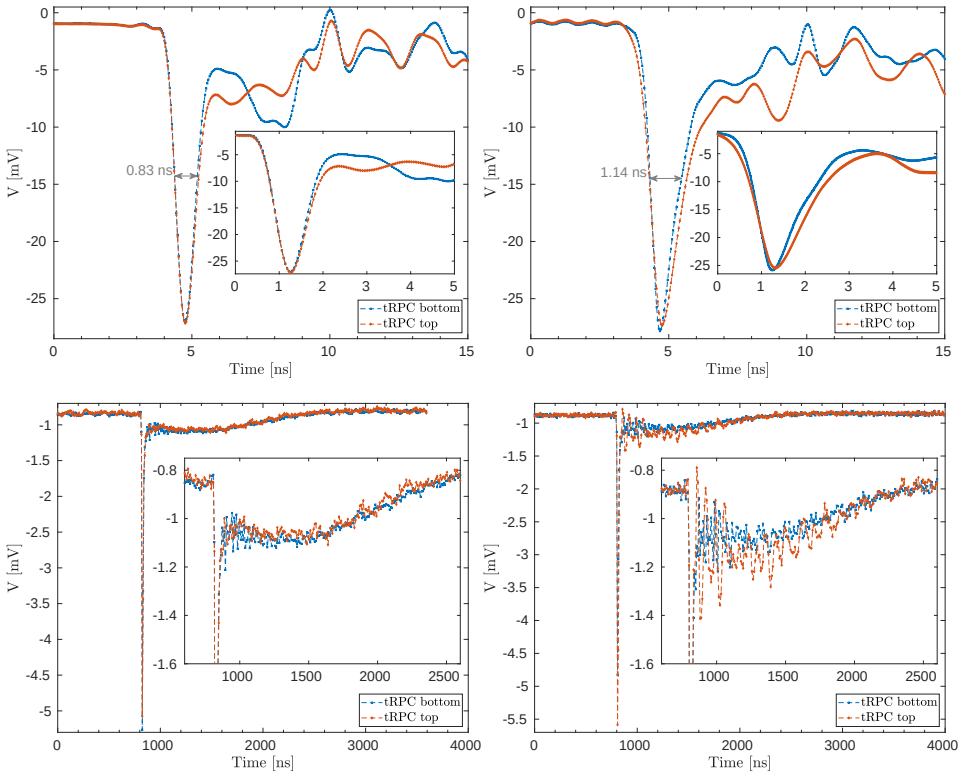

FIGURE 5.10: Induced signals amplified (∼11 V/V gain) directly at the output of the double tRPC prototype. Top: on the left, pulses related to the fast component of the signal, induced separately by the tRPC bottom and top[22] (one RPC turned off at a time); on the right, same as on the left but after removing the top ground plane. Unlike the other subfigures, this inset shows a separate measurement at 500 ps/div instead of a zoomed-in view. Bottom: fast and slow components of the induced signals with (left) and without (right) top ground plane.

The signals induced in the wide strips, depicted in Figure 5.10, can also be used to compare the electronic and ionic contributions to the total collected charge. Since the pulses were measured across a 50 Ω resistor, the collected charge is related to the measured

[22] the pulse from the tRPC top is the same as that shown in Figure 5.9.

voltage as shown in Equation (5.16).

$$q(t) = \int i(t)\,dt = \frac{1}{R}\int v(t)\,dt \tag{5.16}$$

The charge from the electronic component can therefore be estimated from the area of the corresponding pulse in Figure 5.10:

$$Q_{e^-} \approx \frac{25\,mV \times 1\,ns}{50\,\Omega} = 500\,fC. \tag{5.17}$$

Equivalently, for the ionic component:

$$Q_{ion} \approx \frac{0.2\,mV \times 1200\,ns}{50\,\Omega} = 4800\,fC, \tag{5.18}$$

showing that the ions migrating toward the cathode induce ∼10 times more charge than the electrons moving in the opposite direction. Both values of Q_{e^-} and Q_{ion} include the ∼11 V/V amplification factor of the BGA2712. Ions induce a charge ∼10 times larger than that of electrons, but collected over a time ∼1000 times longer[23], resulting in a current 100 times lower:

$$I_{ion} = \frac{\Delta Q_{ion}}{\Delta t_{ion}} \approx \frac{10\,\Delta Q_{e^-}}{1000\,\Delta t_{e^-}} = \frac{1}{100} I_{e^-}. \tag{5.19}$$

Spatial Resolution Measurements

The spatial resolution along the wide strips was evaluated using the double MRPC prototype, comparing results from its full configuration to those obtained after removing the thin-strip readout electrodes, to assess their impact on the return paths of the previously mentioned transmission lines.

Signals were induced in the wide strips using a 'flat injector', made of a 1 mm-wide flat copper conductor. Most of the injector was shielded with adhesive copper tape, leaving only a small end of the flat cable (∼2 mm) outside the shielding to enable signal induction into the wide strips via capacitive coupling. The unshielded end of the injector was placed directly below the wide-strip readout electrode, emulating signal induction from the MRPC.

Signals composed of a sharp negative pulse followed by a slower ion tail similar to those shown in Figure 5.10, were sent through the flat injector. A position map of the induced signals in the first wide strip, with and without thin-strip readout electrodes, is depicted in Figure 5.11a. The events induced in the wide strip exhibit a broader distribution along the

[23] due to their mobility being about 2-3 orders of magnitude lower than that of electrons.

strip when the thin-strip PCBs are present in the setup. This result highlights a potential degradation of the transmission line, with signal propagation along the return path likely affected by the presence of thin strips.

The propagation velocity of the induced signals in the wide strips was also evaluated using the flat injector (see Figure 5.11b). Its initial position was measured, as well as after two consecutive translations of 5 cm along the wide strip. Knowing the positions of the induced signals, expressed in nanoseconds as obtained via Equation (4.3), and the corresponding translations in millimeters, the propagation velocity could be computed: v_p = 50 mm / 0.295 ns = 169.5 mm/ns. The obtained result closely matches the 171 mm/ns value used throughout this work[24], as mentioned in Subsection 4.2.4.

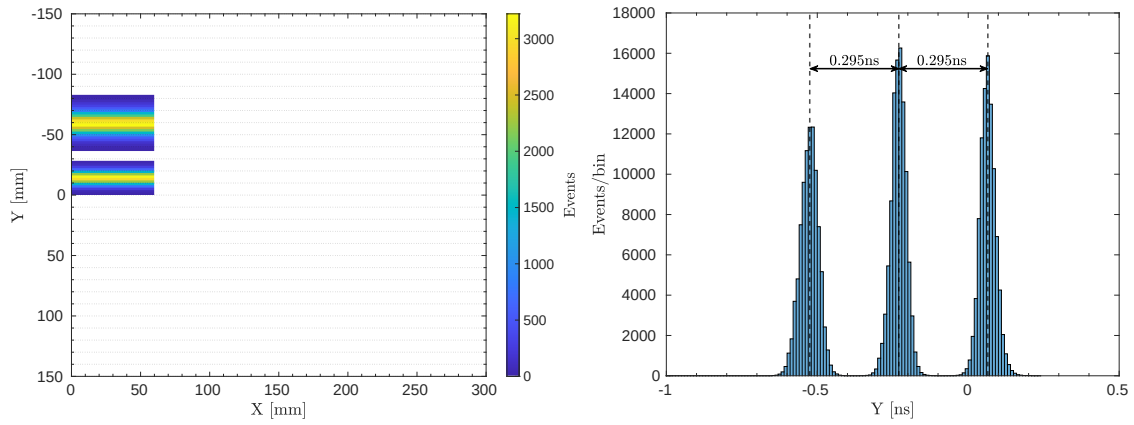

(a) (b)

FIGURE 5.11: (a) Position map of the induced signals with and without thin-strip readout electrodes. Two runs with a similar number of events, but located at different positions along the first wide strip, were selected for comparison: the events in the upper part of the wide strip correspond to measurements with thin-strip PCBs included in the setup, while the lower ones were obtained without them. Along the Y-axis, a 2 mm bin was used, while in the orthogonal direction, the bin size corresponds to the wide strip width (6 cm). (b) Evaluation of the propagation velocity of the induced signals in the wide strips. The shifts between the peaks correspond to 5 cm translations of the flat injector along the wide strip.

The spatial resolution along the wide strips was evaluated by fitting the position distributions of the induced signals along the Y-axis. Figure 5.12 presents an example of the fit obtained for each setup configuration. The standard deviations, averaged over multiple runs for each setup configuration, are given in Table 5.3.

[24] which is also in the same order of magnitude as the typical 50 Ω coaxial cables: ∼200 mm/ns (5 ns/m) [Leo94]; as a side note, this value corresponds to approximately 0.6c, with the speed of light in vacuum: c ∼300 mm/ns.

	Longitudinal spatial resolution
Without thin-strip readout electrodes	4.2 ± 0.3 mm
With thin-strip readout electrodes	5.9 ± 0.4 mm

TABLE 5.3: Longitudinal spatial resolution along the wide strips with and without thin-strip PCBs.

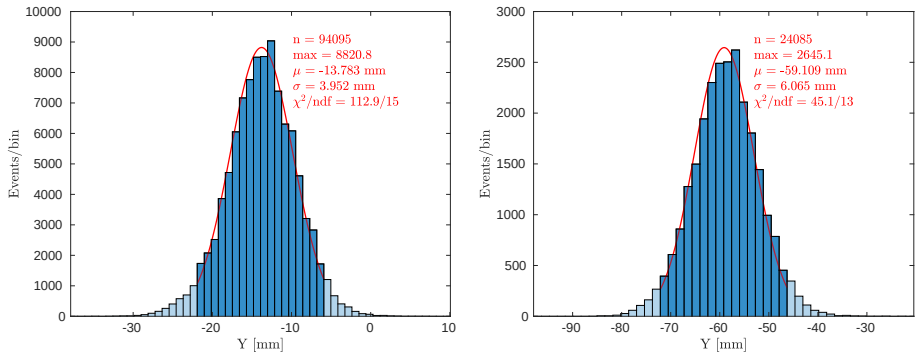

(a) (b)

FIGURE 5.12: (a) Spatial distribution of the induced signals from the flat injector positioned below a wide strip, after the removal of the thin-strip readout electrodes from the double MRPC prototype. (b) Same measurement, but with the complete setup configuration, including the thin-strip PCBs.

The values of Table 5.3 align with the expected spatial resolution, given the time resolution of the respective FEE (35 ps, see Subsection 4.2.4), and by applying the error propagation formula for uncorrelated errors (Equation (5.8)) to Equation (4.3):

$$\begin{aligned}
\sigma_Y^2 &= \left(\frac{\partial Y}{\partial T_f}\right)^2 \sigma_{T_f}^2 + \left(\frac{\partial Y}{\partial T_b}\right)^2 \sigma_{T_b}^2 \\
\sigma_Y^2 &= \left(\frac{1}{2}\right)^2 \sigma_{FEE}^2 + \left(-\frac{1}{2}\right)^2 \sigma_{FEE}^2 \\
\sigma_Y &= \sqrt{\frac{1}{2}\,\sigma_{FEE}^2} = \frac{\sqrt{2}}{2}\,\sigma_{FEE} = \frac{\sqrt{2}}{2} \times 35 \quad [ps] \\
\sigma_Y &= \frac{\sqrt{2}}{2} \times 35\,ps \times \frac{171\,mm}{1000\,ps} \approx 4.2 \qquad [mm].
\end{aligned} \tag{5.20}$$

This theoretical value of 4.2 mm (σ) for the longitudinal spatial resolution, based on the known time resolution of the FEE, was the basis for the choice of several parameters for the detectors tested in this work, namely:

- **wide-strip pitch**: the primary role of the wide-strip electrode is to identify which of the thin strips, wired in parallel, was induced with a signal. Assuming a spatial

resolution of 4.2 mm (σ), the wide strips can identify nearly all events within a range of $\pm 4\,\sigma$, which corresponds to $8 \times 4.2 = 33.6$ mm. Therefore, thin strips wired in parallel (i.e., strips connected to the same electronic channel) and transversely aligned with respect to the wide strips should be separated by more than ∼3.5 cm to be unequivocally distinguished. Adding a safety margin of 1–2 cm implies that parallel thin strips should be separated along the wide strips by 5–6 cm. Parallel thin strips, longitudinally aligned with the wide strips, must also be distinguished. Thus, the wide-strip pitch must match the spacing determined by the longitudinal resolution, with a final safety value set to ∼6 cm.

- **thin-strip pitch**: with 48 ADC channels available per add-on board connected to the DAQ (24 channels for each dimension), an optimal pitch of ∼60 mm / 24 = ∼2.5 mm was opted for both thin-strip electrodes to ensure precise 2D spatial resolution.

The approximate results obtained with Equation (5.13) indicated that the FEE time resolution achieved with an MRPC could be worse than expected. The longitudinal spatial resolution of 5.9 ± 0.4 mm (σ), as given in Table 5.3 and measured with the full configuration of the double MRPC prototype, confirms the previous result. The range of $\pm 4\,\sigma$ still falls within the safety value of 6 cm, but with a margin of only ∼1 cm. If the FEE time resolution degrades during a cosmic-ray run to, for example, ∼60 ps, this margin would no longer be sufficient, as shown using Equation (5.20). This fact might explain the 'ghost images' observed along the wide strips in the image reconstruction of the scintillators. These artifacts were specific to this setup and disappeared after switching to tRPCs, as discussed in the next Subsection.

Finally, in case of limited time resolution from the FEE connected to the wide strips, the solution would be to increase the number of ADC channels or the thin-strip pitch, followed by a larger wide-strip pitch. However, both solutions have downsides: increasing the number of electronic channels would raise cost and complexity, while a larger strip pitch would negatively impact spatial resolution.

5.2.3 2D Reconstruction Maps

This subsection examines whether the technique of reducing FEE channels by joining strips in parallel enables the successful and unambiguous determination of the 2D position of MIPs passing through the detector. The effectiveness of combining information from the thin-strip and wide-strip readout electrodes was evaluated by reconstructing the projected image of the scintillators used for external triggering and positioned directly above and below the RPCs. For each ionizing event registered by both scintillators, a 2D position

was assigned, provided that the RPCs simultaneously detected the particle. The spatial distribution map of events achieved over time can then be seen as a 'projected shadow' of the scintillators on the RPCs. Additionally, the details visible on the reconstructed image of the scintillators can be used to infer the spatial resolution of the detector. This method could be applied to the setups that included both thin and wide strips, namely: the double MRPC and tRPC prototypes and the large-area RPC. Long runs with cosmic rays, lasting several weeks, were therefore performed for each of the mentioned setups, also enabling time resolution measurements, as discussed in the next and final subsection.

Event Positioning Algorithm with Thin and Wide Strips

Several attempts were made before establishing the current algorithm, which utilizes information from both thin and wide strips to determine the precise event position. For each ionizing particle passing through the detector, the thin-strip readout electrodes provide a transverse position relative to their strips. By the fact of having N thin strips connected in parallel, each position can actually be viewed as N different positions $((X_{fine1},...,X_{fineN}),(Y_{fine1},...,Y_{fineN}))$. In contrast, the wide-strip readout electrode provides only one coarse position per event in both dimensions (X_{coarse},Y_{coarse}). The final 2D position (X_{final},Y_{final}) is simply determined by selecting the N-position that minimizes the distance to the corresponding coarse position.

As mentioned earlier in this chapter, the default charge-sharing model used in this work was the centroid algorithm. A relevant input parameter for the centroid method is the window size, which defines the number of strips to be included in Equation (5.7). This parameter can be determined from the detector charge profile, selecting a number of strips based on its width to exclude regions with minimal signal contribution or predominantly noise. Figure 5.13a shows two numerical simulations of charge profile, one for each type of geometry used in this work. The induced charge pattern on the thin strips was numerically calculated using the following approach:

- the electric potential V and electric field $\vec{E}$ were computed for a specific detector geometry by solving Gauss's Law, which, when written in its differential form, takes the expression:

$$\nabla \cdot (\varepsilon \vec{E}) = \rho, \tag{5.21}$$

where ρ and ε denote the charge density and the permittivity[25] across the different

[25] $\varepsilon = \varepsilon_r \varepsilon_0$, with ε_r the relative permittivity of each layer, and $\varepsilon_0 = \sim 8.85 \times 10^{-12}$ F/m the vacuum permittivity.

layers in the detector, respectively. Since $\vec{E} = -\nabla V$, and in the absence of trapped charges in the detector ($\rho = 0$), Equation (5.21) reduces to the Laplace equation in inhomogeneous media:

$$\nabla \cdot (\varepsilon \nabla V) = 0. \tag{5.22}$$

This partial differential equation was solved using the finite element method for a simplified two-dimensional geometry, with the X-axis corresponding to the direction transverse to the thin strips and the Y-axis spanning across all the RPC layers (resistive electrodes ($\varepsilon_r = 4$), gas gaps ($\varepsilon_r = 1$), and the PP ($\varepsilon_r = 3$) layers at the top and bottom of the detector). The geometry was sufficiently large along the X-axis to neglect edge effects.

- the boundary conditions for the thin strips were defined in accordance with the Shockley–Ramo theorem (introduced earlier in Subsection 3.2.3), which involves the concepts of weighting potential $\mathrm{V_w}$ and weighting field[26] $\vec{E}_w$. Specifically, the central strip was assigned a weighting potential $\mathrm{V_w} = 1$, while all other strips were set to 0. Under these conditions, solving Equation (5.22) for the detector geometry yields the weighting potential $\mathrm{V_w}$, and computing its gradient gives the weighting field $\vec{E}_w$ throughout the detector. These two quantities are not the actual electric potential $\mathrm{V_{det}}$ and field $\vec{E}_{det}$ applied to the detector; rather, they serve solely as a convenient means to compute the induced charge on the thin-strip readout electrodes. The ion-electron pairs generated in the gas gaps follow the field lines of the applied electric field $\vec{E}_{det}$. In contrast, $\vec{E}_w$ depends only on the materials and geometry of the detector, and it dictates how charge motion influences the signal on the readout electrode.

- the motion of a carrier of charge q along the gas gap (assumed to occur only along the Y-axis) induces a charge Q_{ind} on the readout electrode, which was computed by integrating the weighting field along the Y-direction $E_{w,y}$, with the integration limits corresponding to the start y_1 and end y_2 of the gas gap, as given by Equation (5.23).

$$Q_{ind} = q \int_{y_1}^{y_2} E_{w,y}\, dy \tag{5.23}$$

Alternatively, the induced charge can be obtained as the product of the carrier charge

[26] in the Shockley–Ramo theorem the weighting potential is defined to be dimensionless and its gradient – the weighting field – has units of m^{-1}, as mentioned in Appendix B.

and the difference in the weighting potential at the boundaries of the gas gap:

$$Q_{ind} = -q\,\Delta V_w = q\,(V_w(y_1) - V_w(y_2)). \tag{5.24}$$

Either Equation (5.23) or Equation (5.24) can be used to obtain the charge profiles shown in Figure 5.13a. The respective derivations are provided in Appendix B.

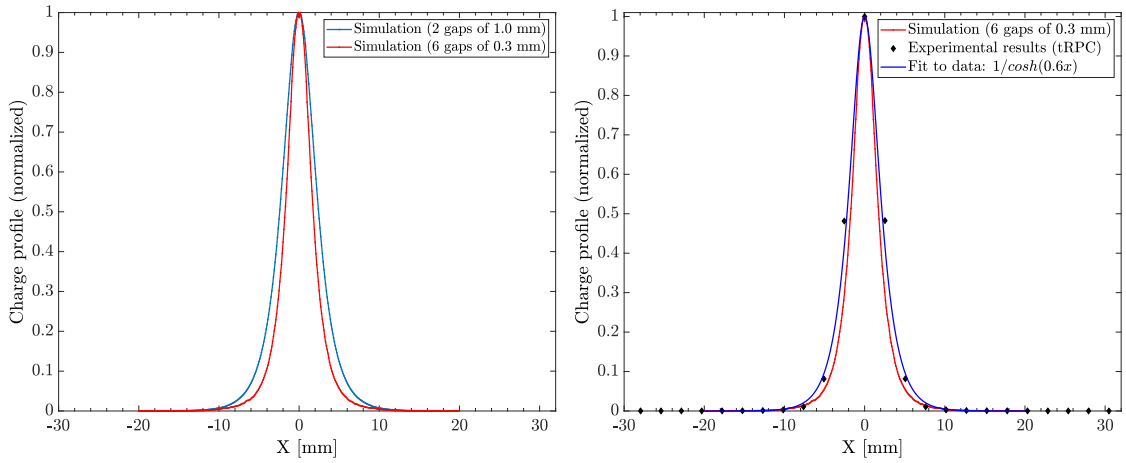

(a) (b)

FIGURE 5.13: (a) Numerical simulations of the charge profile induced in the thin-strip readout electrode for an MRPC (two 1 mm gaps) and a tRPC (six 0.3 mm gaps), highlighting that most of the induced charge is contained in a region of ∼1.5 cm. The total charge profile is the sum of the individual contributions from each gap. (b) Experimental results of the charge collected in the 24 thin strips (24 data points), obtained with a tRPC during a four-week cosmic-ray run. A $\cosh^{-1}$ fit to the measurements is also presented, along with the corresponding simulated profile, replicated from (a) for better comparison.

To compare with simulations, Figure 5.13b presents the experimental data obtained with the double tRPC prototype[27] during a cosmic-ray run of several weeks. Measurements and simulations show good agreement, further indicating that the window size for applying the centroid algorithm should include approximately 10 thin strips.

An hyperbolic secant fit to the data points is also shown in the Figure 5.13b, which, in its full form, can be written as:

$$Q_{fit}(x) = A\,sech\left(\frac{x - x_0}{\delta}\right) = \frac{A}{cosh(\frac{x-x_0}{\delta})}, \tag{5.25}$$

[27] as previously mentioned, the signal collected in each thin-strip readout PCB originates only from the closest RPC, as the wide-strip electrode between the RPCs act as a barrier, with the electric field lines terminating on their surface.

where the scaling factor A was set to 1, the strip position x_0 to 0, and δ, related to the profile width and having units of length, was adjusted to fit the experimental points ($1/\delta = 0.6$). Additional information on the exponential fall-off of the charge profile and the corresponding sech fit can be found in [Pum69, Aie14].

A final step is required before applying the centroid method and visualizing the event maps of the scintillator positioned above and below the RPCs. As previously shown in Figure 4.2, a pattern of 24 strips is repeated N times on the SMPCB to connect the thin strips in parallel. Due to this repeated structure, the strips at both ends (strips 1 and 24) are physically adjacent. In the event of an ionizing interaction near the transition between strips 1 and 24, the charge is apparently induced in two separate groups: one at the beginning and one at the end of the strip pattern. However, since strip 24 is physically adjacent to strip 1, these groups are effectively part of the same profile of charge. To address the issue of apparent charge splitting, a circular shift is applied to the strip pattern. The shift repositions the strip with the maximum charge to the center of the pattern (position 12). This ensures that the centroid calculation is based on a consistent (unsplit) distribution. After computing the fine position, a shift in the opposite direction must be applied to obtain the final effective position of the ionizing interactions.

2D Event Map – Double MRPC Prototype

By combining all information from the thin and wide strips, it was possible to reconstruct the 2D position map of the observed events. Figure 5.14a shows the projected shadow of the 8×3×2 cm^3 scintillators on the MRPCs, obtained through the centroid algorithm applying the following filtering criteria:

- subtraction of the background contribution to ensure Q = 0 at the strip positions when no event is present. Otherwise, the reconstructed positions tend to be systematically closer to the strip centers rather than the interstrip regions, leading to an artificial increase in events at the strip centers.
- removal of events with multiplicity[28] above two (M > 2) on the wide strips. Events with charge in three or more wide strips often led to incorrect X_{coarse} or Y_{coarse} estimates;
- filtering out events containing more than one cluster on the wide strips, corresponding to M = 2 events with charge on non-adjacent wide strips.

[28] number of wide strips with charge at both ends in a given event.

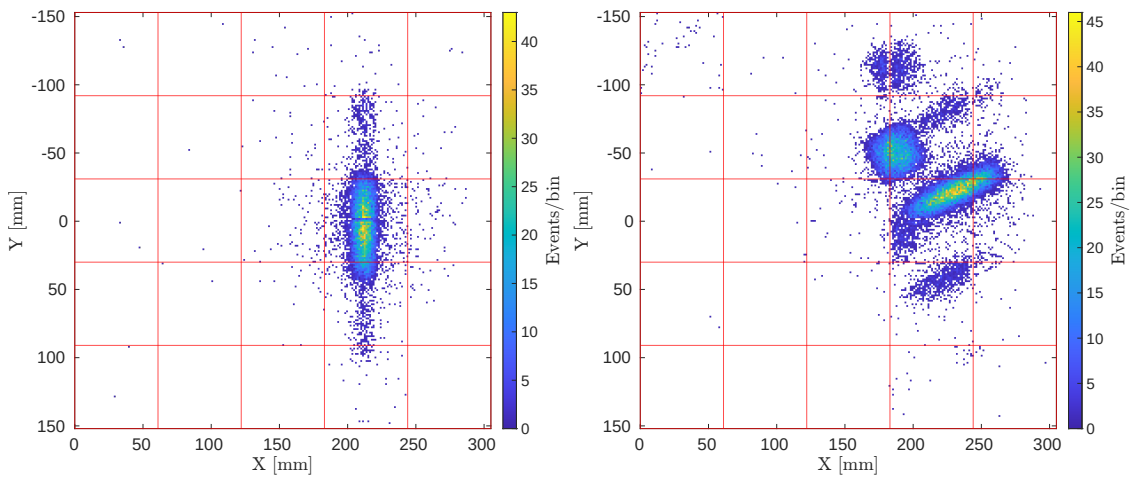

FIGURE 5.14: (a) 2D position map of the 8×3×2 cm^3 scintillators, created with a bin size of 1.3 mm in both dimensions. With the 3 cm side aligned vertically, the scintillators project a shadow of approximately 8 cm × 2 cm on the MRPCs. The red lines indicate the boundaries between repeated groups of 24 thin strips in both horizontal and vertical directions. (b) Same as (a), for a run that also includes 4×4×1 cm^3 scintillators, allowing for better visualization of the ghost images along the Y-axis.

For Figure 5.14b, a second set of plastic scintillators was added to the setup and included in the trigger logic. Each 4×4×1 cm^3 scintillator was coupled to a Silicon Photomultiplier (SiPM) (C-Series from ON Semiconductor) and, as with the previous scintillators, they were placed on both sides of the MRPCs.

The main features observed in Figures 5.14a and 5.14b are as follows:

- the nylon monofilament spacers, installed transversely to the wide strips between the glass resistive electrodes, are visible at y = -1.2 mm (see Figure 5.14a). The presence of 1 mm-diameter fishing lines between the glass electrodes completely inhibits gas ionization at this location. The lack of events observed at the spacer location thus indicates the level of detail achieved in the reconstructed image of the scintillators. The spatial resolution of the MRPCs is therefore expected to be at least on the millimeter scale, as inferred from the smallest observed detail. For better visualization of the absence of events at the spacer location, Figure 5.15 shows the projection of the 2D event map (Figure 5.14a) onto the Y-axis. A clear reduction in the number of events is observed at the location of the 1 mm gas gap spacers.

- events with misattributed positions are visible around the correct location of the scintillators. However, a higher concentration of points is located in two regions extending along the Y-axis, before and after the main location, resulting in two

ghost images of the scintillators. These ghost features are even more evident in Figure 5.14b and could not be suppressed by the previously mentioned filtering procedure. These artifacts indicate that the longitudinal position Y_{coarse} provided by the wide strips[29] is too far from the true event location, leading to the event being assigned to an incorrect thin strip. Moreover, since the ghost images disappeared after migrating to tRPCs while retaining the same readout electrodes and electronics, this suggests that the spatial resolution along the wide strips improved with these detectors – an improvement that can be attributed to the reduction in timing jitter, as described in Subsection 5.2.2.

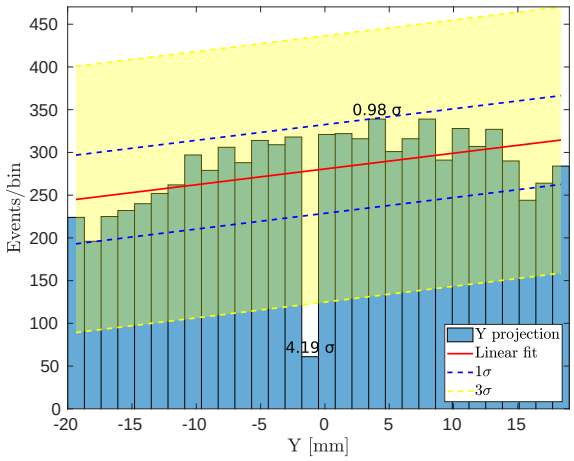

FIGURE 5.15: Projection of the 2D event map from Figure 5.14a onto the Y-axis. A significant reduction in the number of events at y = -1.2 mm is observed due to the presence of the 1 mm gas gap spacers.

2D Event Map – Double tRPC Prototype

Long runs with cosmic rays were also conducted using the double tRPC prototype, enabling the reconstruction of 2D position maps as before. Figure 5.16a displays the projected shadows of: **(i)** the same 8×3×2 cm^3 scintillators coupled to PMTs, and **(ii)** two 4×4×1 cm^3 scintillators joined side by side and read out by SiPMs, corresponding to scintillators with total dimensions of 8×4×1 cm^3 located on both sides of the tRPCs. Figure 5.16b shows the results of a second run, where all scintillators are positioned differently to assess the consistency of the algorithm applied across various regions.

[29] obtained through the subtraction of times measured at both strip ends (see Equation (4.3)).

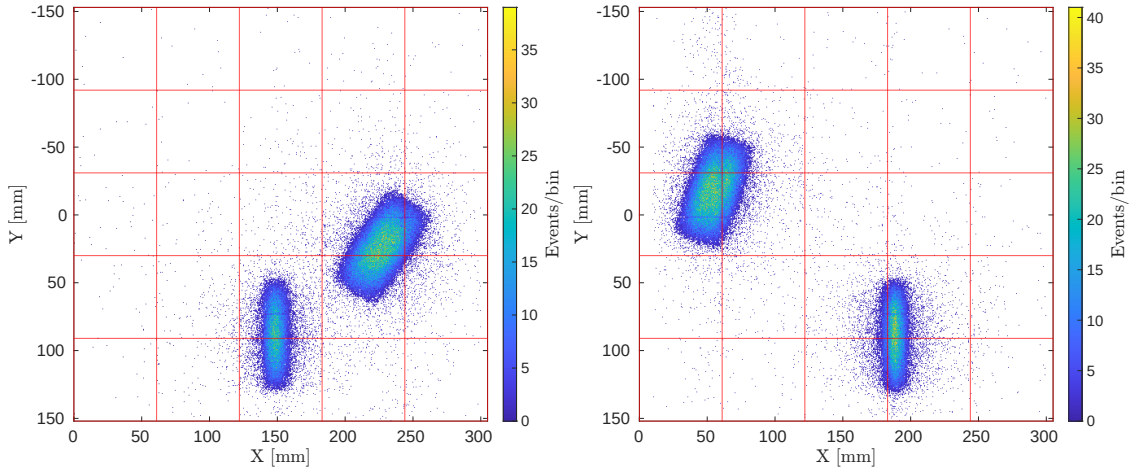

(a) (b)

FIGURE 5.16: (a) 2D position map of the 8×3×2 cm^3 and 8×4×1 cm^3 scintillators with a 0.6 mm bin size in both dimensions. (b) Same as (a) with scintillators repositioned.

As discussed before, applying the same event positioning algorithm and filtering procedure to the tRPCs eliminated the ghost images, reinforcing that the faster signal response of these detectors improved spatial resolution along the wide strips. Notably, the nylon monofilament spacers, now with a diameter of only 300 µm (1 mm for the MRPCs), remain visible at two distinct locations: y = 1.7 mm and y = 73.1 mm. This last result indicates that, despite thin strips being grouped in parallel by SMPCBs, a submillimeter 2D spatial resolution was achieved with the double tRPC prototype. Figures 5.17a–5.17d show the projections of the position maps from Figure 5.16 onto the Y-axis, allowing for better identification of the locations of the respective monofilament spacers.

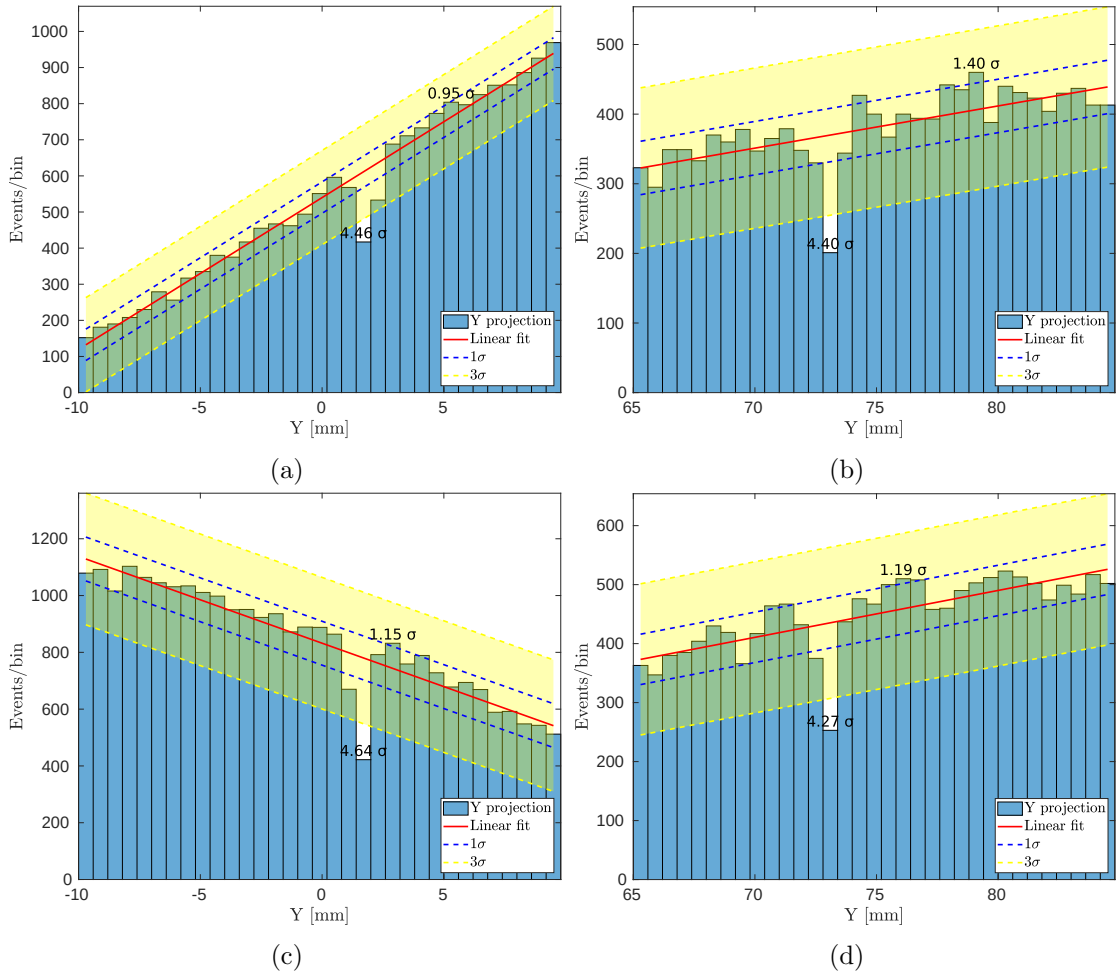

FIGURE 5.17: (a) & (b) Projection of the 2D event maps from Figure 5.16a onto the Y-axis. (c) & (d) Same as (a) & (b) for Figure 5.16b. In all cases, the locations of the 300-µm gas gap spacers are clearly identified.

2D Event Map – Large-Area Detector

A 2D position map was also created using the large-area tRPCs and the 8×3×2 cm^3 scintillators. The full map, covering approximately 130 cm × 90 cm, can be seen in Figure 5.18. As in the previous event maps, the red lines mark the boundaries between repeated groups of 24 thin strips in both dimensions (X,Y). If the readout codification based on the SMPCBs were not applied, only a small square in the full map could be instrumented with the 48 ADC channels currently in use. Moreover, for comparison, the area of the previous prototypes corresponds to 5×5 squares in this map, an area that is approximately 13 times smaller than the current tRPCs.

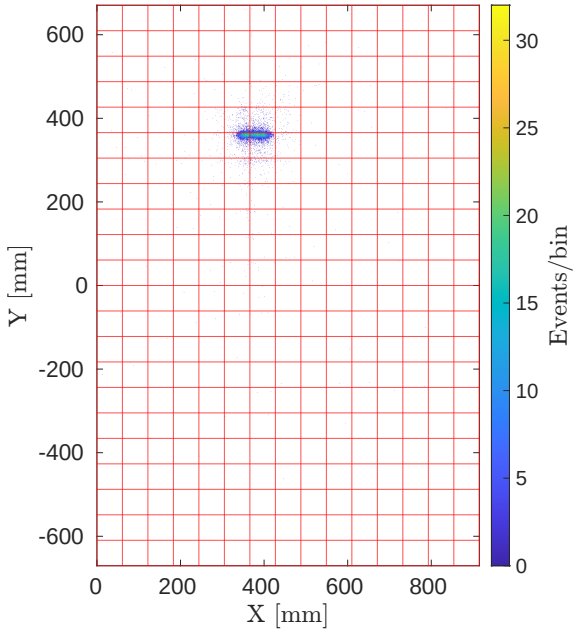

FIGURE 5.18: 2D position map of the 8×3×2 cm^3 scintillators over the full detector area, created with a 1.0 mm bin size in both dimensions.

Whereas the previous prototypes used 24+24 electronic channels to read out 120+120 pick-up strips, the same channels now read out a total of 888 strips: 360 longitudinally and 528 transversely. In the longitudinal direction, each channel is connected to 15 strips in parallel, each ∼130 cm in length, resulting in a total strip length of about 20 m. A similar strip length of 20 m per FEE channel is achieved in the transverse direction by joining 22 strips of ∼90 cm. Migrating to the large-area detector, the increase in capacitance was thus inevitable, along with its impact on electronic noise, as explained earlier in Subsection 5.2.1. Nevertheless, despite the expected and observed signal degradation, the 300-µm nylon spacers were also visible in the current event map. A zoomed-in view of the 2D map is shown in Figure 5.19a for better identification of the spacer location, while Figure 5.19b presents the respective projection onto the X-axis. For the zoomed-in view, an additional filter was applied to remove bins with only a single event, as these may be considered statistically insignificant after weeks of data collection. The impact of the additional filter can be seen by comparing with Figure 5.18 (by zooming into the figure), where the event map was generated without this filter.

Despite the large number of strips connected in parallel, the increase in electronic noise was not enough to compromise the detection of the 300-µm spacers. The absence of events at the spacer location in the reconstructed image of the scintillators indicates that a submillimeter 2D spatial resolution was also achieved with the large-area tRPCs.

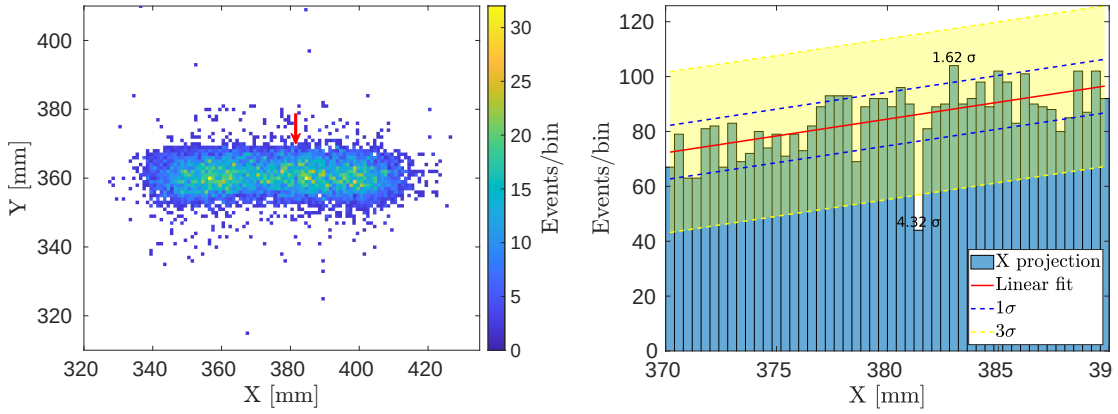

(a) (b)

FIGURE 5.19: (a) 2D position map of the 8×3×2 cm^3 scintillators. The red arrow identifies the location of the spacers installed longitudinally between the glass electrodes. (b) Projection of the 2D event map onto the X-axis, showing a clear reduction in the number of events at the location of the 300-µm gas gap spacers.

Fitting-Based Interpolation Methods

Several alternatives to the centroid algorithm were tested for reconstructing the 2D position maps of the scintillators. Two of them, based on fitting methods and found to provide good results, are presented here, namely:

- a hyperbolic secant fit, as previously shown in Figure 5.13 and defined by Equation (5.25);
- a Gaussian fit, used for its good approximation to the shape of the charge profile induced on the thin strips.

For each event, the charge values collected on the different thin strips were fitted to determine the position of the ionizing event in both dimensions. The 2D event maps obtained by applying the hyperbolic secant and Gaussian fits are shown in Figures 5.20a and 5.20b, respectively. The corresponding event map obtained using the default interpolation method of the centroid algorithm was presented in Figure 5.16a. While the fitting-based interpolation methods yielded good results, none outperformed the centroid approach. This is also confirmed by the respective projections onto the Y-axis (see Figures 5.21a–5.21d), which can be compared with Figures 5.17a and 5.17b.

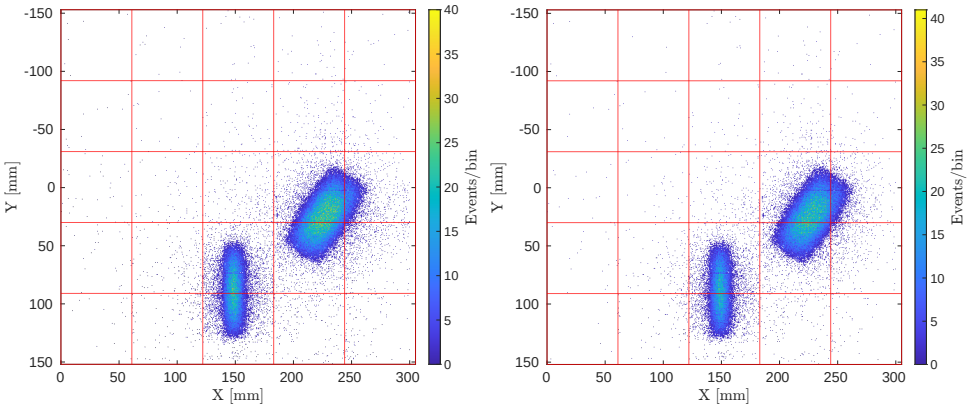

FIGURE 5.20: (a) 2D position map of the 8×3×2 cm^3 and 8×4×1 cm^3 scintillators with a 0.6 mm bin size in both dimensions, obtained using the hyperbolic secant fit. (b) Same as (a) but using the Gaussian fit.

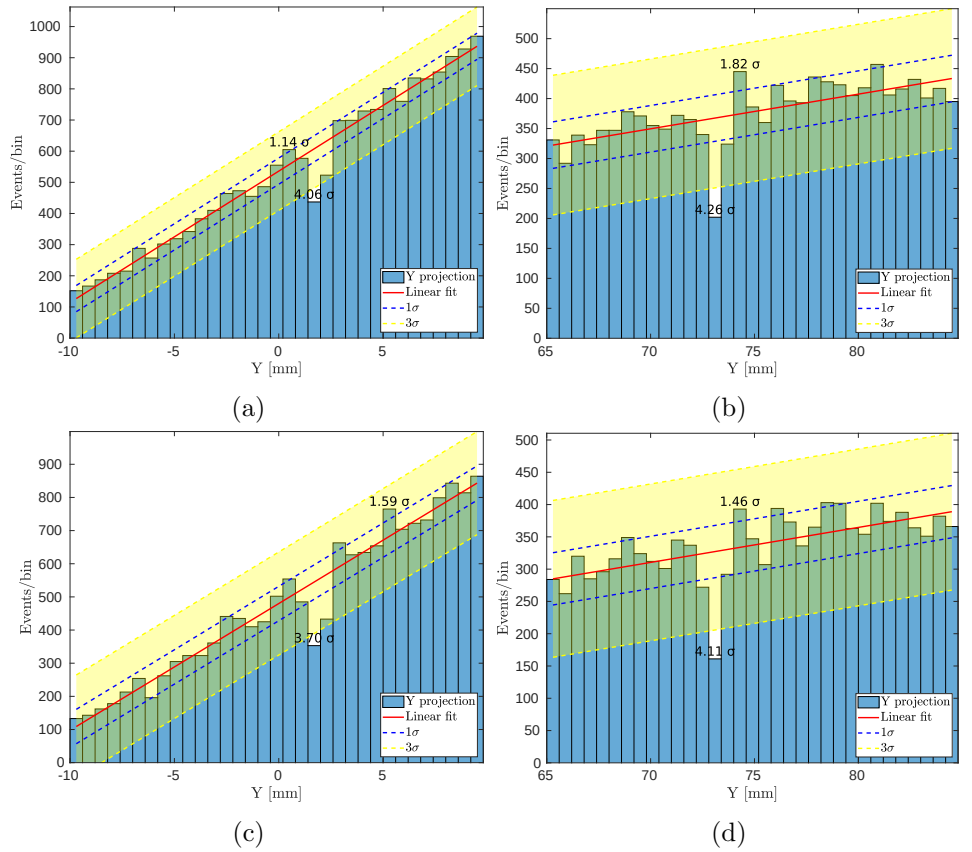

FIGURE 5.21: (a) & (b) Projection of the 2D event maps from Figure 5.20a onto the Y-axis (hyperbolic secant fit). (c) & (d) Same as (a) & (b) for Figure 5.20b (Gaussian fit).

5.3 Time Resolution

A single detector capable of simultaneously providing precise position and time measurements of ionizing events over large areas is particularly valuable. For the MST application, as further discussed in the next chapter, combining particle tracking with temporal information enables the rejection of low-energy muons via the TOF technique, thereby reducing the time required to identify the presence of high-Z materials in large-volume inspections.

As mentioned in Subsection 4.2.4, the current-sensitive electronics connected to the wide strips enable precise time measurements, along with the 2D positional information required by the encoding scheme implemented on the SMPCBs. The time resolution was therefore evaluated for the setups including the wide-strip readout electrode, namely: the double MRPC and tRPC prototypes, and the large-area tRPC. For each setup, the time resolution was inferred by subtracting the RPC time from that of one of the scintillators used in the coincidence trigger during the extended cosmic-ray runs. The RPC time, in turn, was computed as the average of the times measured at both ends of the wide strips, as given by Equation (4.2). The temporal resolution based on times from this formula is detector-dependent, in contrast to the spatial resolution, which is derived by subtracting the same time values (Equation (4.3)), thereby canceling the RPC contribution. Figure 5.22a displays the time distribution obtained for the double tRPC prototype, with a corresponding temporal resolution of 83 ps (σ_{RPC-SC_1}). The resolution achieved with the large-area tRPCs was slightly higher as shown in Figure 5.22b.

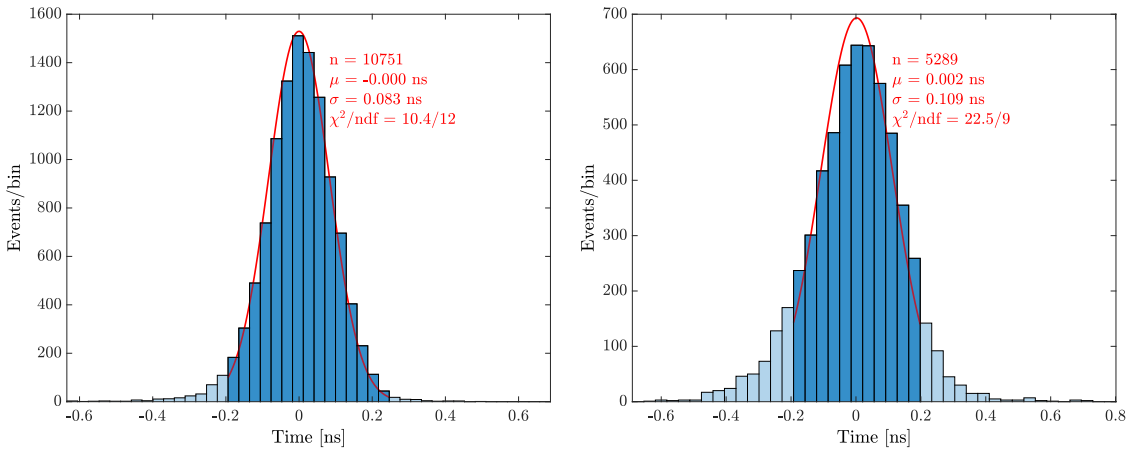

(a) (b)

FIGURE 5.22: (a) Distribution of time differences measured by the double tRPC prototype and a 8×3×2 cm^3 scintillator (SC_1). (b) Same as (a) for the large-area tRPCs.

Setup/configuration	Time resolution (σ)
Double tRPC prototype	65 ps
Double tRPC prototype without GP*	111 ps
Large-area tRPCs	89 ps
Double MRPC prototype	291 ps

* GP: top ground plane

TABLE 5.4: Time resolution values obtained with different setups and configurations.

These timing values also include the scintillator component σ_{SC_1}, which must be subtracted in quadrature to obtain the intrinsic RPC contribution. This can be done by computing the time differences between all detectors (RPC, scintillators 1 and 2 (SC_1, SC_2)) and solving the following system of equations:

$$\begin{bmatrix} 1 & 1 & 0 \\ 1 & 0 & 1 \\ 0 & 1 & 1 \end{bmatrix} \begin{bmatrix} \sigma^2_{RPC} \\ \sigma^2_{SC_1} \\ \sigma^2_{SC_2} \end{bmatrix} = \begin{bmatrix} \sigma^2_{RPC\text{-}SC_1} \\ \sigma^2_{RPC\text{-}SC_2} \\ \sigma^2_{SC_1\text{-}SC_2} \end{bmatrix}. \tag{5.26}$$

As a result, the final time resolution achieved for the double tRPC prototype was 65 ps (σ_{RPC}). For the large-area tRPCs, the time resolution obtained over a 50-day acquisition period was 89 ps (σ_{RPC}), a few tens of picoseconds higher than the value achieved with the previous prototype. However, the slight reduction in resolution observed with the larger detector may be attributed to the initial conditioning[30] of the tRPCs, as the resolution gradually improved over time, reaching 73 ps (σ_{RPC}) when considering only the last 10 days of acquisition.

In Subsection 5.2.2, a degradation of the signals induced in the wide strips was reported following the removal of the top ground plane from the double tRPC prototype. A long run with cosmic rays was performed under the same configuration, also registering an impact on time resolution, which deteriorated to 111 ps (σ_{RPC}).

Temporal measurements were also performed with the double MRPC prototype for comparison with a detector not designed for precise timing. Following the same approach as previously, a clear decrease in time resolution was observed in this case: 291 ps (σ_{RPC}).

Table 5.4 compiles all temporal measurements obtained with the different setups for reference. To maximize the resolutions reported in this section and to correct for the systematic effect of time walk, the following procedure was applied:

[30] time spanning days or weeks following the initial application of high voltage to the RPC, during which the current and counting rate progressively decrease. This stabilization process might be related to irregularities on the resistive electrode surfaces, which initially act as localized discharge points and are gradually etched by repeated discharges. [Abb18]

- after computing the scintillators' charge spectra, only events with charges within a window around the main peak of the distribution were selected to exclude outliers, such as anomalous energy deposits from partial crossings of the scintillator or from pile-up;
- also known as slewing correction, the time-walk effect is a systematic shift in the threshold-crossing time that depends on signal amplitude, with larger signals crossing the discriminator threshold earlier. Time walk was corrected by plotting the event times against the corresponding charge. The time vs. charge correlation was then fitted with a polynomial function, and the fitted values were subtracted on an event-by-event basis to flatten the dependence, as shown in Figure 5.23.

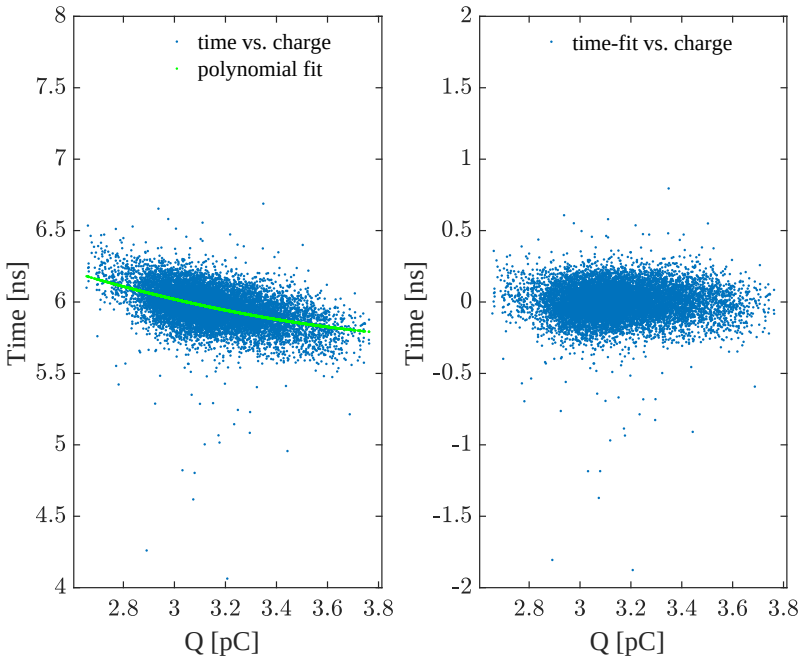

FIGURE 5.23: Example of slewing correction applied to the scintillator charge collected during a long run. Lower charges systematically require more time to cross the discriminator threshold (left). Subtracting a second-order polynomial fit from the event times compensates for this time shift (right). The corrected event times must then be plotted against the RPC collected charge to undergo a second time-walk correction.

For the sake of completeness, Figure 5.24a shows a charge spectrum example of the double tRPC prototype, obtained with the current-sensitive electronics. While this distribution of charges corresponds mainly to ionizations by MIPs throughout all gas gaps (cosmic-ray run), Figure 5.24b shows a charge spectrum obtained with the same detector

in self-trigger mode, where ionizations[31] most often occurs in a single gap.

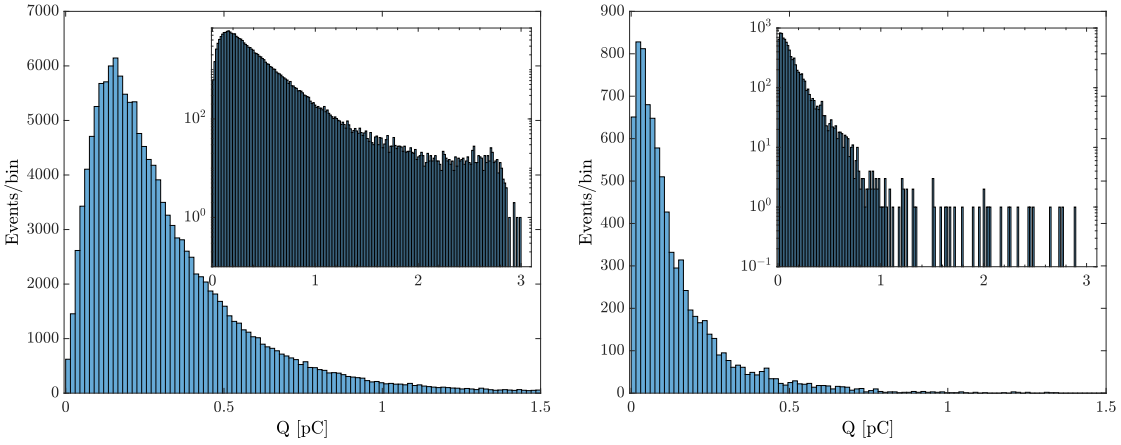

(a) (b)

FIGURE 5.24: Charge spectra of the double tRPC prototype obtained with the current-sensitive electronics connected to the wide-strip electrode, triggering with MIPs (a) and in self-trigger mode (b). The distributions are also shown in the insets with the Y-axis in logarithmic scale.

[31] spontaneous electron emission from a resistive electrode surface starting an avalanche in this gap.

6

Monte Carlo Simulations for MST

In parallel with the development of the SMPCB-based readout method, the use of RPCs to scan large volumes via the MST technique was evaluated. This solution would present several key advantages: **(1)** submillimeter 2D spatial resolution for measuring small scattering angles (on the order of one degree) between incoming and outgoing muon trajectories within the scanned volume, **(2)** sub-100 ps time resolution for TOF rejection of low-energy muons (a few hundred MeV), which undergo strong multiple scattering in all materials, including the RPCs, and **(3)** a significant cost reduction in building large sensitive areas (over 100 m^2 for the shipping container scan), due to two factors: the substantial reduction in FEE channels when using SMPCBs, and the inherently lower cost of the RPC technology.

The approach consisted of performing extensive FLUKA Monte Carlo simulations [Bat15, Ahd22], using the sea-level muon flux as the source term, transported through both a medium-sized volume ($\sim$1 m^3) and a full-size truck geometry ($\sim$150 m^3) (see Figure 6.1). Several geometry variants were simulated, beginning with: **(i)** a simple empty volume filled with air, **(ii)** the same volume including two RPCs on the top side and two on the bottom side, **(iii)** the addition of a floor, truck platform, and shipping container in the case of the large-area geometry, and **(iv)** the inclusion, for the full geometry, of a 10 cm $\times$ 10 cm $\times$ 10 cm block made of aluminium (Al), iron (Fe), tungsten (W), or uranium

(U), placed at the center of the fiducial region.

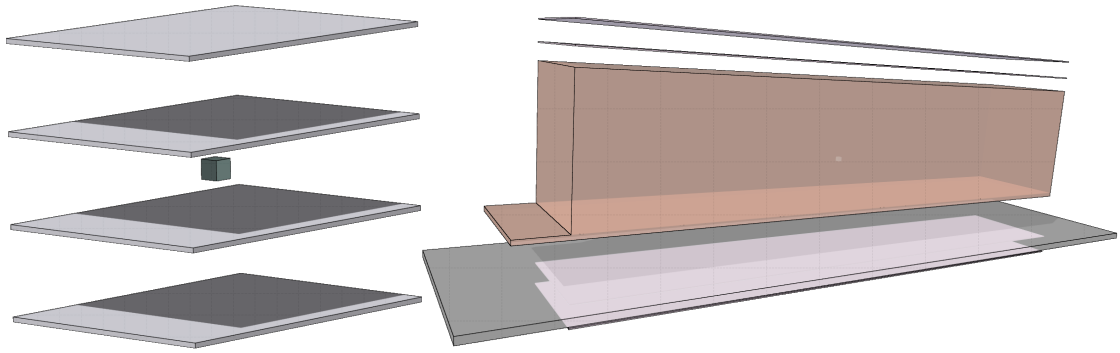

(a) (b)

FIGURE 6.1: (a) Medium-sized geometry including 4 RPCs spaced by 45 cm, each measuring 1.6 m × 1.2 m, and a block of high-Z material inside the volume between the two inner planes (fiducial region). Distance between external RPCs: 1.35 m. The dimensions of the medium-sized geometry are approximately those of the tracker used in the MST scan described in Subsection 2.2.3 (see Figure 2.7). (b) Large-area geometry, also with 2 detector planes on the top and bottom sides, each with 13.7 m × 2.5 m. It includes a 15 cm-thick concrete floor, a truck platform with a thickness of 10 cm and steel walls 2 mm thick, and a shipping containers also made of steel, with 2 mm thick walls and of dimensions: 13.7 m × 2.5 m × 2.9 m. A 10 cm × 10 cm × 10 cm high-Z block is also present inside the container. Distance between external RPCs: 5.45 m. Performed using the FLAIR graphical interface [Vla24].

Based on the FLUKA calculations, the collected data were used to:

- compute the scattering angle distributions of muons within the fiducial region;
- reconstruct the 3D image of the scanned object by plotting directly the midpoint of the common perpendicular (PoCA) between the incident and exiting trajectories;
- estimate the exposure time required to identify high-Z materials after populating a voxelized fiducial region with PoCAs.

Section 6.4 provides further details on these results.

6.1 The FLUKA Monte Carlo Code

FLUKA is a general-purpose Monte Carlo code for simulating the interaction and transport of about 60 particles, including photons and electrons (from 100 eV – 1 keV to thousands of TeV), neutrinos, muons of any energy, hadrons up to 10 PeV, neutrons

down to thermal energies, and heavy ions [Bat15, CER]. The FLUKA code is nowadays used for a wide range of applications, from accelerator shielding to target design, calorimetry, activation, dosimetry, cosmic ray and neutrino physics, radiotherapy, etc [CER]. For cosmic-ray studies, FLUKA provides a Galactic Cosmic Ray (GCR) package, benchmarked against experimental data [Bat07], which enables the simulation of cosmic-ray showers in the atmosphere. It includes:

- two sets of primary spectra from Z = 1 to Z = 28, each corresponding to a different phase of the solar activity (see Section 6.1.3);
- a spherical model of the Earth's geometry, including the surrounding atmosphere divided into 100 layers from 0 to ∼71 km above sea level, each with a different atmospheric depth (see Section 6.1.4);
- a geomagnetic field that modulates the primary spectra based on the provided vertical cutoff rigidity. The chosen geomagnetic model was a centered dipole approximation of the Earth's magnetic field.

One method used in this work to obtain the muon flux at sea level is based on this package, as detailed in Subsection 6.2.1. This approach is called a two-step simulation, as the particle spectra from the first step are provided as input to a second simulation that includes one of the geometries shown in Figure 6.1. The second method is based on a simple muon generator developed for the present study and described in Subsection 6.2.2. After obtaining the muon flux at sea level, FLUKA simulations of MST involving high-Z materials were performed for each geometry in Figure 6.1.

6.1.1 Multiple Scattering Interactions

As mentioned in Chapter 2, muons primarily lose energy through inelastic scattering with orbital electrons (excitation/ionization), while their angular deflection in matter is mainly caused by elastic scattering with nuclei (MCS).

The MCS model implemented in FLUKA [Fer92] is based on Molière theory and has proven to be very robust, giving accurate results for all charged particles, including in backscattering experiments [CER]. The algorithm preserves several correlations, including between the scattering angle and path length corrections (longitudinal displacement), and between the scattering angle and lateral displacement [Fas97]. An optional single scattering mode is also available, e.g. for very thin layers where Molière theory does not apply.

6.1.2 User Routines

Custom input/output user interfaces, known as user routines and written in Fortran 77, are available for more complex sources or specific needs. In the present work, two of them were systematically used:

- **source.f**: the muon flux at sea level, obtained from the first-step simulation or the muon generator, must be provided as a source term in the simulations with the medium- or large-area geometry shown in Figure 6.1. The source routine enables phase-space sampling from a file containing all the information about the particles to be transported, namely particle code and weight, momentum, starting position, and direction;

- **mgdraw.f**: it allows dumping information during particle transport when specific interactions or events, such as boundary crossings, occur. For instance, in the first-step simulation described in Subsection 6.2.1, PCRs are propagated through the atmosphere, and the particle data (momentum, position, direction, etc.) are dumped each time a muon exits the last atmospheric layer and enters the ground. Furthermore, when propagating muons from the first-step simulation into the medium- or large-area geometry, their entering and exiting directions in the fiducial region can be reconstructed from the intersection positions at each detector layer. These crossing positions, along with the particle energy and direction, are also dumped using the mgdraw routine.

6.1.3 Primary Cosmic-Ray Spectra

The ion composition of the galactic flux is derived from a model that predicts GCR energy spectra as a function of solar modulation, developed by NASA [Bad96]. Based on this model, FLUKA provides the energy spectra for all ions from Z = 1 to Z = 28 for two solar phases, corresponding to minimum and maximum solar activity (see Figure 6.2). The spectra are modified to reflect recent data sets, as noted in the FLUKA manual [CER].

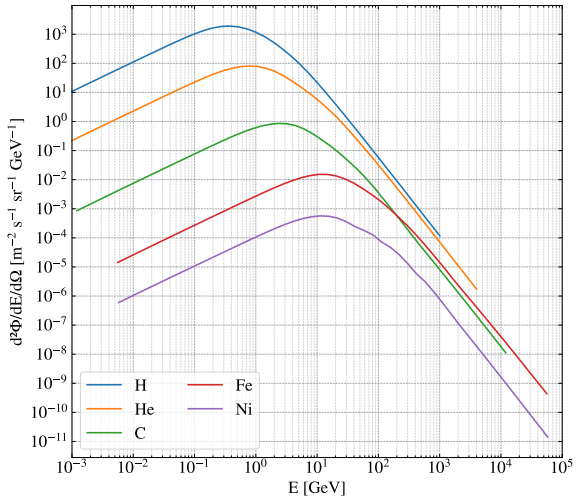

FIGURE 6.2: Differential primary energy spectra at solar minimum for five elements (Z = 1, 2, 6, 26, and 28), retrieved from the FLUKA GCR package, which includes a total of 28 spectra without geomagnetic cutoff, covering ions from Z = 1 to Z = 28. The particle spectra are plotted as a function of kinetic energy per nucleus.

Table 6.1 lists the simulation parameters used to transport the PCRs through the atmosphere.

Parameters	Input Values
Primary ions	$1 \leq Z \leq 28$ (All-particle flux)
Primary energy range	from 100 MeV to 100 TeV
Injection altitude of primaries	∼71 km
Vertical cutoff rigidity	7.5 GV
Geomagnetic cutoff acceptance	7 GV
Geographic latitude/longitude	40.207°N/8.424°W
Surface altitude	105 m

TABLE 6.1: Input settings of the GCR package used to retrieve, from the first-step simulation, the muon flux at sea level.

6.1.4 FLUKA Atmospheric Model

The geometry provided by the GCR package corresponds to a spherical model of the whole Earth, including its surrounding atmosphere. The transport of the PCRs is restricted to a specific slice of the atmosphere, defined by the volume between two truncated cones (see Figure 6.3a). This region, labeled **1** in the figure, contains the atmosphere of interest, being centered at the specified latitude. Its angular span depends on the provided

geomagnetic cutoff acceptance, while the vertical cutoff rigidity must be specified for the required latitude and longitude. A third cone, oriented in the opposite direction to the previous ones (with its vertex outside the Earth, above the North Pole), is used to define the additional regions **2** and **3**. Primary and secondary particles originating from these regions are also taken into account, as they can reach the region of interest.

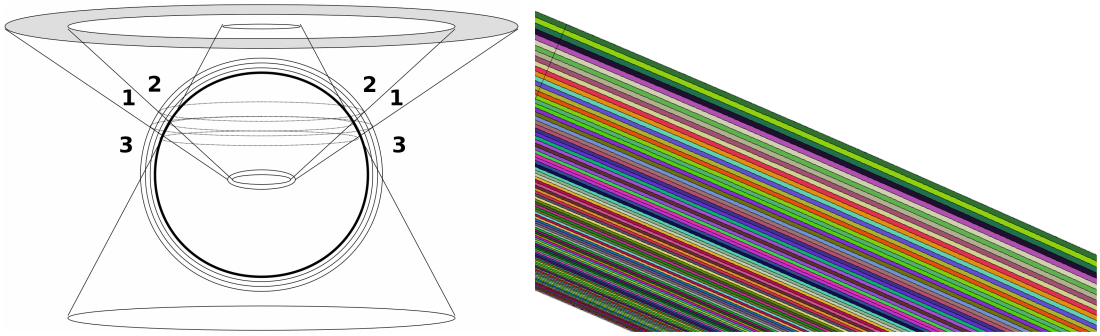

(a) (b)

FIGURE 6.3: (a) Schematic view of the spherical model of the Earth and its atmosphere, as implemented in the FLUKA GCR package. Three truncated cones define the local atmosphere through which PCRs are propagated. The scoring region where the muon flux crossing the Earth's surface is evaluated lies directly below region 1. (b) 100 Atmospheric shells, ranging from 0 to ∼71 km above sea level, each with a corresponding atmospheric depth. The ground is located directly below the bottommost layer shown in the figure.

A partial view of the atmosphere surrounding the Earth is shown in Figure 6.3b. The implemented geometry includes 101 concentric spheres extending up to approximately ∼71 km above ground. Each layer is assigned an atmospheric depth that increases as altitude decreases, following values similar to those shown in Figure 1.2.

6.2 Muon Flux at Sea Level

As previously mentioned, two methods were used to obtain the muon flux at sea level: **(i)** one using the FLUKA GCR module to propagate cosmic rays through the atmosphere and record the position and direction of each muon entering the ground, and **(ii)** the other based on a muon generator developed for the present work. With the muon flux at sea level available, simulations involving RPCs to perform the MST scan of high-Z materials could then be carried out for the medium- and large-sized geometries previously presented. Both methods are described in the next subsections, along with their respective strengths and limitations. A comparison of the resulting muon fluxes is subsequently presented in Subsection 6.3.2.

6.2.1 FLUKA Two-Step Simulation

In the spherical model of the Earth shown in Figure 6.3a, the region 1 was identified as the atmospheric slice where muons entering the ground have their data dumped by the mgdraw.f routine. Figures 6.4a and 6.4c show two views of about 1000 of these events. Each arrow represents the momentum $\vec{P}_\mu$ of a muon moving from the last atmospheric layer into the ground, indicating its location in the Earth and its direction of motion. The arrow length and color represent the momentum magnitude, with the corresponding color bar shown at the bottom of Figure 6.4.

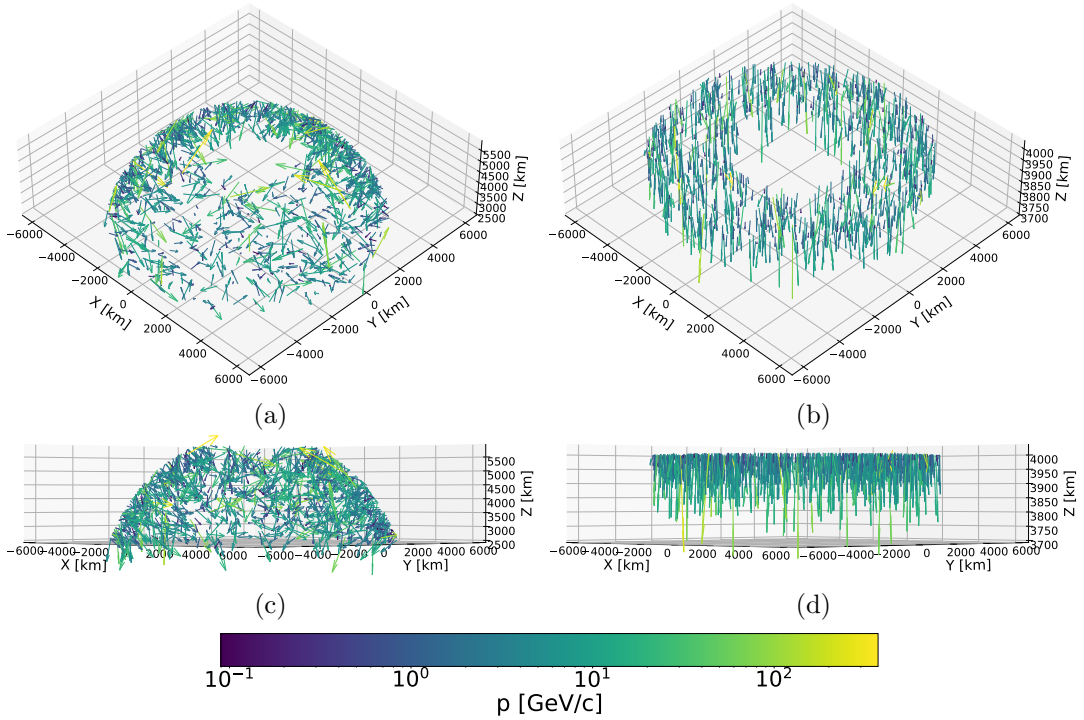

FIGURE 6.4: (a) Momentum vectors of ∼1000 muons hitting the ground, obtained from the first-step simulation using the FLUKA GCR package. (b) Same vectors after rotation by $90° - \theta_{lat}$ to correct for Earth curvature. (c) & (d) Same as (a) & (b), respectively, but shown from a frontal view.

As shown for instance in Figure 6.4c, the muon angular distribution obtained from the first-step simulation is influenced by the Earth's curvature and must be corrected before being used as a source term in the flat geometry of the second-step calculation. In fact, the direction of $\vec{P}_\mu$ at any surface point of the implemented spherical Earth model depends on the respective latitude θ_{lat}. To compensate for this effect, each vector, represented by its direction cosines in the global (X, Y, Z) coordinate system, must be rotated by

$90° - \theta_{lat}$, as illustrated in Figure 6.5. The rotation was performed using the Euler–Rodrigues formula [Dai15], defined by:

$$\vec{P}_{\mu}^{\,'} = \vec{P}_{\mu}\cos\theta^{'} + (\vec{k}\times\vec{P}_{\mu})\sin\theta^{'} + \vec{k}(\vec{k}\cdot\vec{P}_{\mu})(1-\cos\theta^{'}), \tag{6.1}$$

where $\vec{P}_{\mu}$ is the original momentum vector, $\vec{k}$ the unit vector along the rotation axis, and $\theta^{'}$ the rotation angle, i.e., the complement of the latitude as mentioned above. In turn, the rotation axis is defined as the normal vector to the plane containing the Earth's axis (Z-axis in Figure 6.5) and the muon's position on the surface. The rotated vectors $\vec{P}_{\mu}^{\,'}$ obtained using Rodrigues' formula are shown in Figures 6.4c and 6.4d, while the final muon spectra are presented in the Subsection 6.3.2.

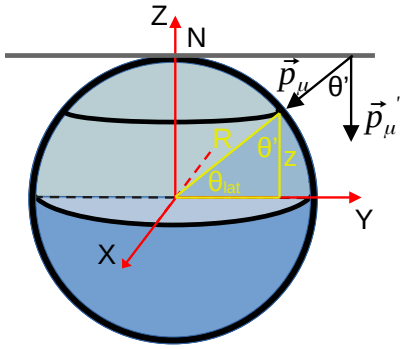

FIGURE 6.5: Schematic representation of the Earth model illustrating the rotation required to transition from a spherical to a planar geometry, preserving the muon angular distribution at sea level.

Based on the first-step simulation, a phase-space file containing all muon parameters at sea level and required for the second step can be generated. Each muon, with its direction corrected for Earth curvature and its position randomly distributed on a plane, can then be propagated downward through one of the geometries illustrated in Figure 6.1. Results of this method are shown in Section 6.4.

6.2.2 Muon Generator

The second method for obtaining the muon flux at sea level is based on a generator designed to reproduce a $\cos^2(\theta)$ zenith angle distribution and a differential energy spectrum proportional to $E_{\mu}^{-2.7}$ for muons above 2 GeV, and flat below this energy. The following assumptions were made: **(i)** independence between energy and zenith angle distributions, and **(ii)** rotational symmetry around the vertical axis (azimuthal angle ϕ).

Muon Energy Distribution

The energy distribution of muons at sea level was defined as a power-law spectrum with spectral index 2.7, according to the relation:

$$\begin{cases} f(E) = \frac{1}{N} \times 2^{-2.7}, & \text{for } 0.1 \text{ GeV} \leq E < 2 \text{ GeV} \\ f(E) = \frac{1}{N} \times E^{-2.7}, & \text{for } 2 \text{ GeV} \leq E \leq 1000 \text{ GeV} \end{cases} \quad [\text{GeV}^{-1}], \tag{6.2}$$

with $f(E)$ the PDF of the muon energy, and $N = \sim 0.473$ $[\text{GeV}^{-1.7}]$ the normalization constant obtained by solving:

$$\int_{0.1}^{1000} f(E)\, dE = \int_{0.1}^{2} \frac{1}{N} \times 2^{-2.7}\, dE + \int_{2}^{1000} \frac{1}{N} \times E^{-2.7}\, dE = 1. \tag{6.3}$$

To generate random values following the energy distribution, the inverse transform sampling method was applied, which requires computing the corresponding CDF and its inverse, the Percent Point Function (PPF). From the PPF, random energy values following the original PDF are obtained by using uniformly distributed random numbers between 0 and 1 as input. Both the CDF and PPF were computed analytically and are provided in Equations (6.4) and (6.5), respectively.

$$\begin{cases} F(E) = \int_{0.1}^{E} \frac{1}{N} \times 2^{-2.7}\, dE, & \text{for } 0.1 \text{ GeV} \leq E < 2 \text{ GeV} \\ F(E) = \int_{0.1}^{2} \frac{1}{N} \times 2^{-2.7}\, dE + \int_{2}^{E} \frac{1}{N} \times E^{-2.7}\, dE, & \text{for } 2 \text{ GeV} \leq E \leq 1000 \text{ GeV} \end{cases}$$

$$\begin{cases} F(E) = 0.325 \times (E - 0.1), & \text{for } 0.1 \text{ GeV} \leq E < 2 \text{ GeV} \\ F(E) = 1 - 1.242 \times E^{(-1.7)}, & \text{for } 2 \text{ GeV} \leq E \leq 1000 \text{ GeV} \end{cases} \tag{6.4}$$

$$\begin{cases} F^{-1}(p) = 3.076 \times p + 0.1, & \text{for } 0 \leq p < \sim 0.618 \\ F^{-1}(p) = \left(\frac{1.242}{1-p}\right)^{1/1.7}, & \text{for } \sim 0.618 \leq p < \sim 1 \end{cases} \quad [\text{GeV}] \tag{6.5}$$

Figure 6.6 shows the resulting energy distribution from sampling 10^6 uniformly distributed random numbers in the [0, 1] interval. The figure also includes the input PDF and its corresponding CDF and PPF.

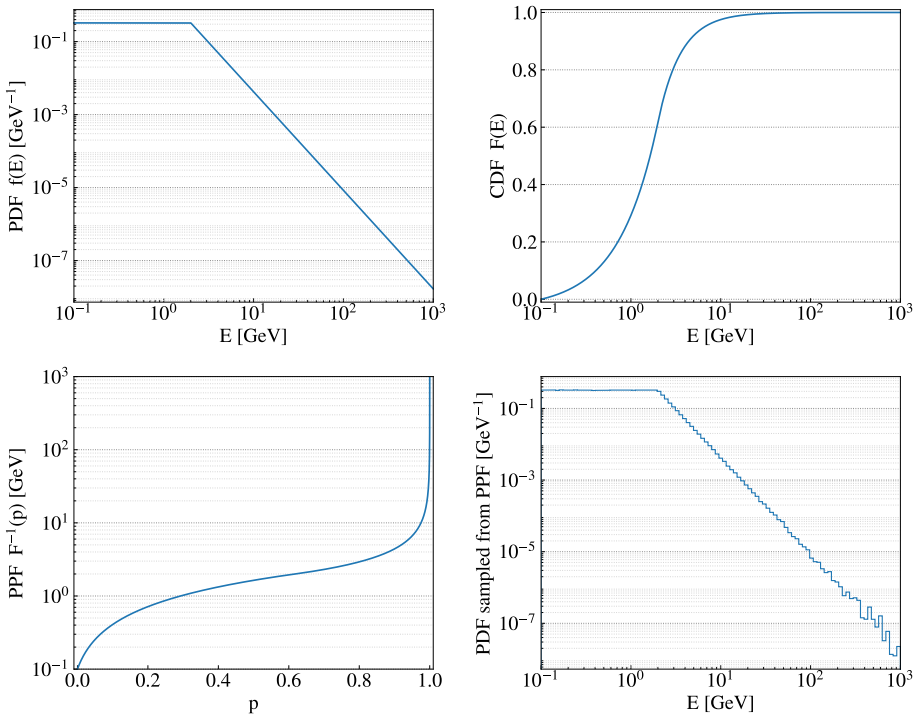

FIGURE 6.6: Random values following an initial energy distribution and generated using the inversion sampling method. Input PDF: defined as a power-law with spectral index 2.7 above 2 GeV and uniform below this energy (top-left). The method involves computing the corresponding CDF (top-right) and PPF (bottom-left). Sampled PDF (bottom-right) obtained by applying the PPF to 10^6 uniform random numbers in [0, 1].

Muon Angular Distribution

The same approach was followed for the angular distribution. In this case, the input PDF must follow a cosine-squared dependence on the zenith angle θ, as shown in Equation (6.6).

$$f(\theta) = \frac{1}{C}\, cos^2(\theta). \quad (\text{rad}^{-1}) \tag{6.6}$$

The normalization constant $C = \pi/4$ (rad^{-1}) is given by:

$$\int_0^{\pi/2} f(\theta)\, d\theta = \int_0^{\pi/2} \frac{1}{C}\, cos^2(\theta)\, d\theta = 1. \tag{6.7}$$

The CDF was also solved analytically (Equation (6.8)) while its inverse had to be computed numerically using the bisection method. In turn, Figure 6.7 shows the angular distribution obtained from 10^6 uniformly distributed random numbers in [0, 1], along with the corresponding input PDF, CDF and PPF plots.

$$F(\theta) = \int_0^{\theta} \frac{4}{\pi} cos^2(\theta)\, d\theta = \frac{2}{\pi}\theta + \frac{1}{\pi} sin(2\theta) \tag{6.8}$$

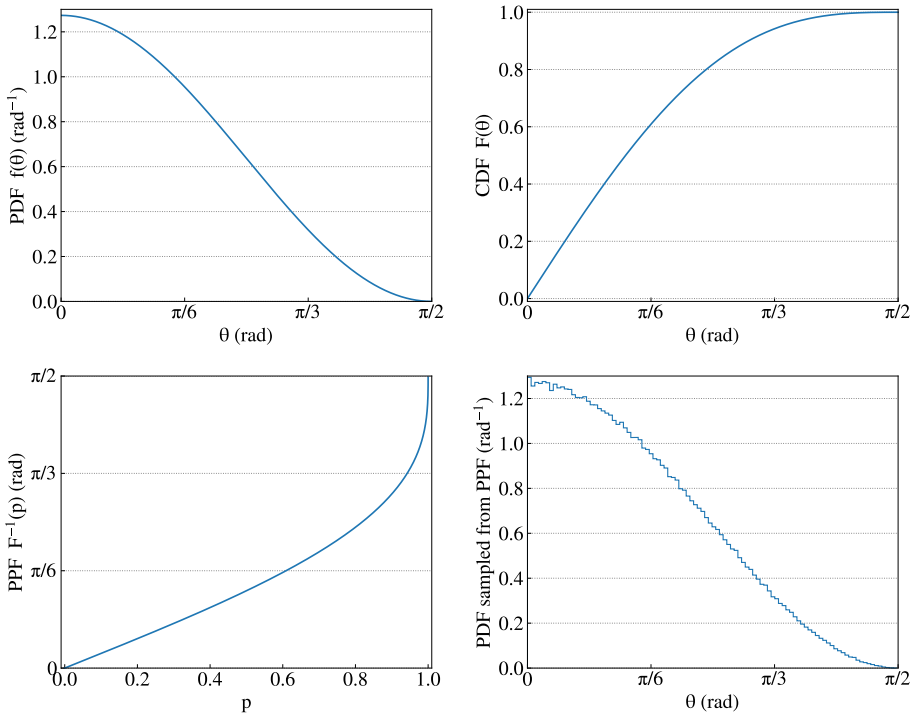

FIGURE 6.7: Random values following the initial angular distribution, generated via the inversion sampling method. Input PDF: based on a $\cos^2(\theta)$ dependence (top-left). Top-right, bottom-left, and bottom-right: the analytically computed CDF, the PPF obtained numerically (bisection method), and the sampled PDF from 10^6 uniform random numbers in [0, 1], respectively.

Muon Phase-Space for FLUKA Calculations

The generator places muons on the surface of a sphere surrounding the geometry of interest. The position and radial direction of each muon are defined by: **(i)** the zenith angle θ, sampled from the angular distribution described above, and **(ii)** the azimuthal angle ϕ, randomly generated with uniform probability between 0 and 360°. To ensure uniform coverage of the geometry while preserving the angular distribution, a random lateral offset (x_0, y_0) is applied to the spherical surface.

A phase-space file combining all the particle information for the FLUKA simulation can finally be created, including:

- the muon energy, sampled from the power-law energy distribution mentioned above;

- the position (x+x_0, y+y_0, z), determined from each (θ, ϕ) pair and including the randomized lateral offsets (x_0, y_0) of the spherical surface source;
- the direction cosines, expressed in the Cartesian coordinate system as cos α, cos β, and cos γ, where α, β, and γ are the angles between the muon direction (defined by (θ, ϕ)) and the positive X-, Y-, and Z-axes, respectively;
- the particle ID corresponding to muons, and the particle weight, set to 1 for all entries.

Figure 6.8 shows an example of 1000 muons generated for the large-area geometry shown in Figure 6.1b.

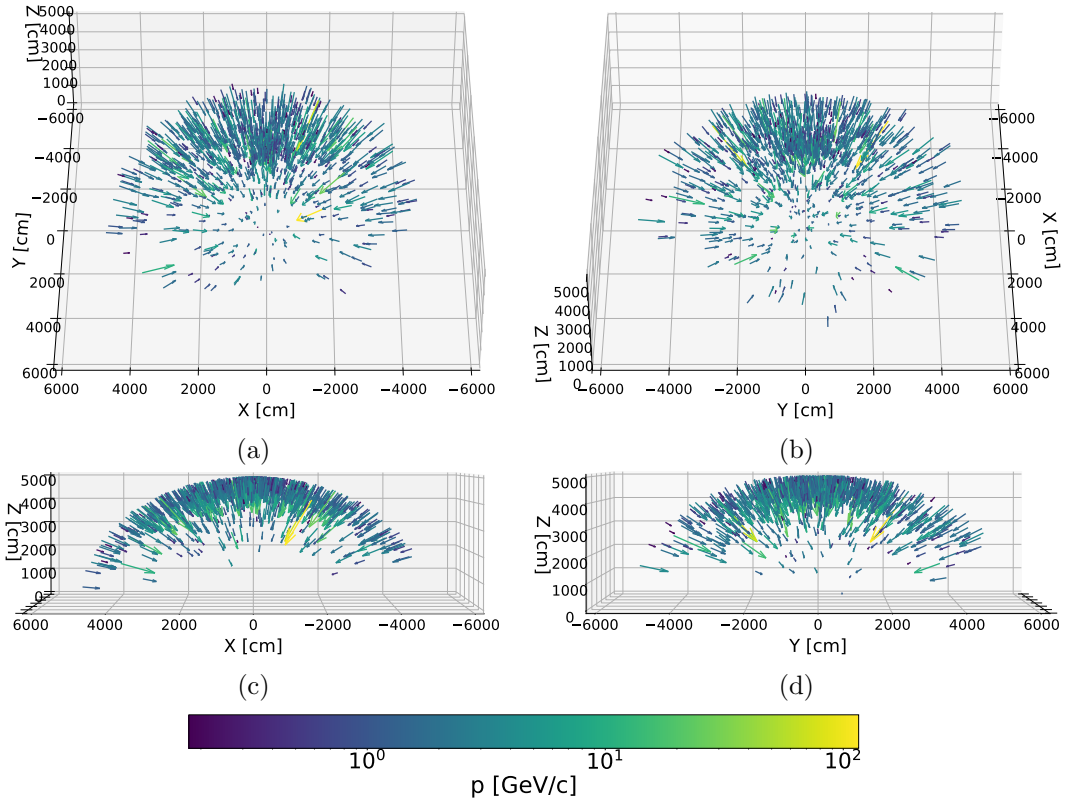

FIGURE 6.8: (a) Momentum vectors of 1000 muons positioned on spheres of radius 50 m, generated for the truck geometry shown in Figure 6.1b. The centers of the spheres are randomly distributed over the area corresponding to the truck location (-125 cm $< x_0 <$ 125 cm; -685 cm $< y_0 <$ 685 cm). (b) Lateral view of the same momentum vectors, corresponding to the side view of the truck. (c) & (d) Same as (a) & (b), respectively, but shown from a frontal view.

6.3 Validation: Calculation vs. Reference Data

In this section, the output from both the two-step simulation method and the muon generator are compared against reference data.

6.3.1 Primary Spectra

In Figure 6.9 the primary energy spectra used in the first-step simulation to obtain the muon flux at sea level (Subsection 6.2.1) are compared with the corresponding GCR spectra from [PDG21]. As shown in the figure, all spectra are in good agreement, which enabled the next validation steps: evaluating the differential muon flux throughout the atmosphere and at sea level.

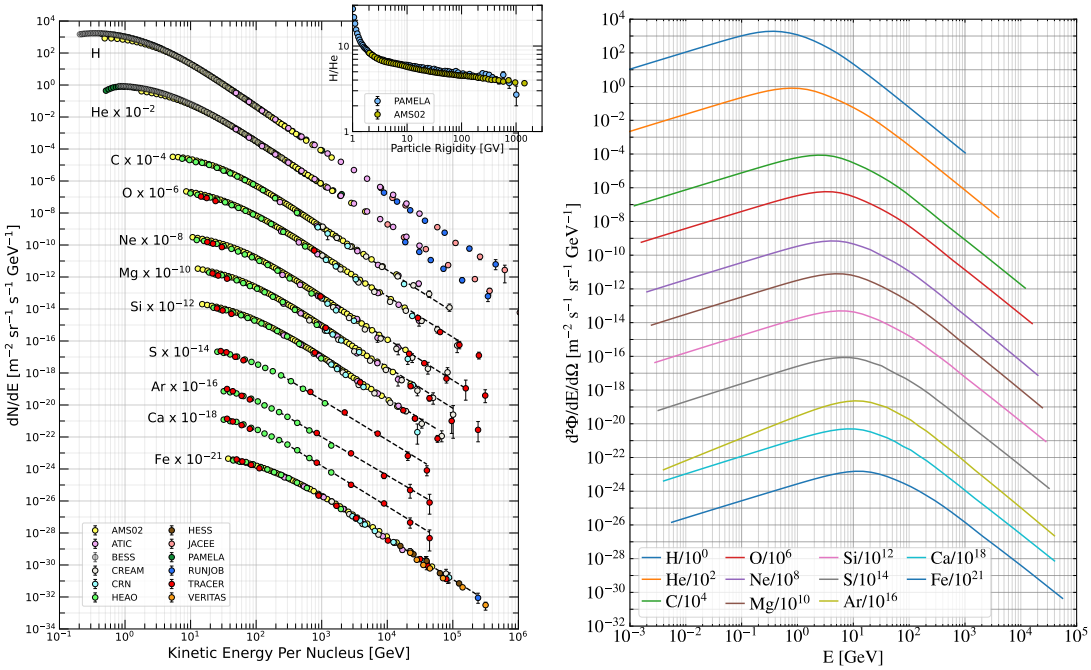

(a) (b)

FIGURE 6.9: (b) Primary energy spectra at solar minimum from the FLUKA GCR package (as in Figure 6.2), scaled (scaling factor indicated in the legend) for direct comparison with the PDG data [PDG21] shown in (a). The particle spectra are, as done before, plotted as a function of kinetic energy per nucleus.

6.3.2 Muon Spectra

In the first-step simulation, the vertical muon flux was evaluated at various altitudes throughout the atmosphere. Figure 6.10b shows the differential angular flux integrated

over energy for muons near the vertical (zenith angle below ∼18°). The muon flux presents, as expected, a maximum between 10 and 15 km and is overall consistent with the calculated vertical flux given by [PDG21] (Figure 6.10a).

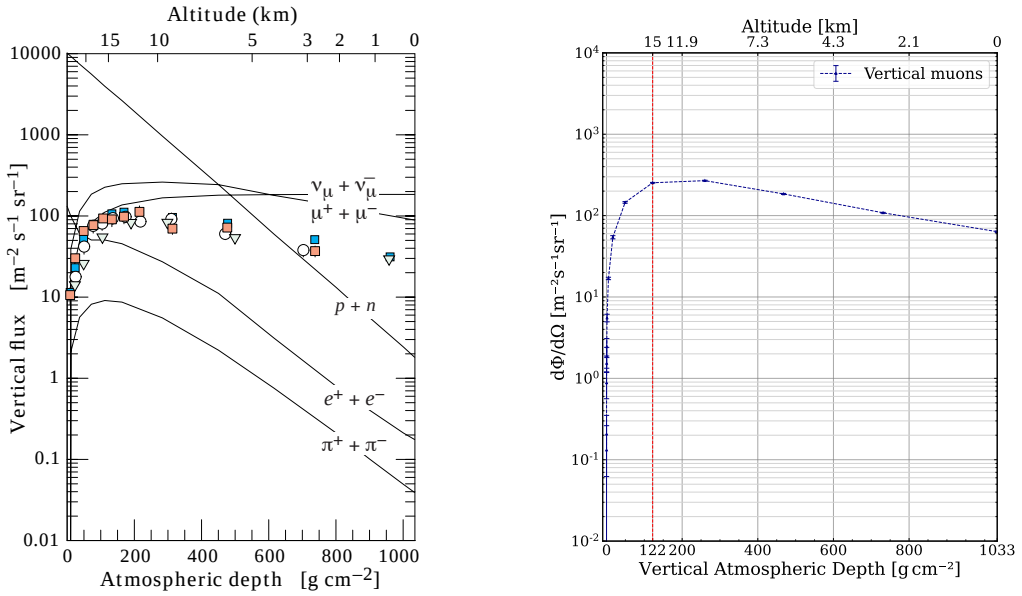

(a) (b)

FIGURE 6.10: Comparison of the vertical muon flux throughout the atmosphere as given by [PDG21] (a) (also shown in Figure 1.5), and the result from the first-step simulation (b).

In turn, Figure 6.11 presents an analytical computation of the muon flux at sea level [Lip93], compared with the spectra of vertical and horizontal muons obtained using both methods developed in this work. As seen from the figure, the two-step simulation method accurately models the muon spectra, showing, for instance, the relative flux enhancement of horizontal muons at higher energies. This result validated the decoupling of the muon angular distribution from the Earth's curvature, as described in Subsection 6.2.1. The difference in flux magnitude observed with the analytical calculation for the horizontal component of low-energy muons likely results from the solid angle aperture chosen for that component. Because the zenith angle coverage does not vary linearly with solid angle, two different binnings were used in these simulations: a $2\pi/20$ sr division, with the first bin corresponding to the vertical component, and a $2\pi/5$ sr division, with the horizontal component taken from the last bin. This choice resulted in zenith angle ranges of ∼18° and ∼12° for the vertical and horizontal bins, respectively. The spectra from the muon generator, in comparison, highlight the assumption of energy-angle independence made in Subsection 6.2.2, and show the clear decrease following the $E^{-2.7}$ power law for energies

above 2 GeV. The generator overestimates the vertical and horizontal components of low-energy muons, but the average spectrum (integrated over 2π sr), shown by the black curve in the figure, is consistent with the two-step method.

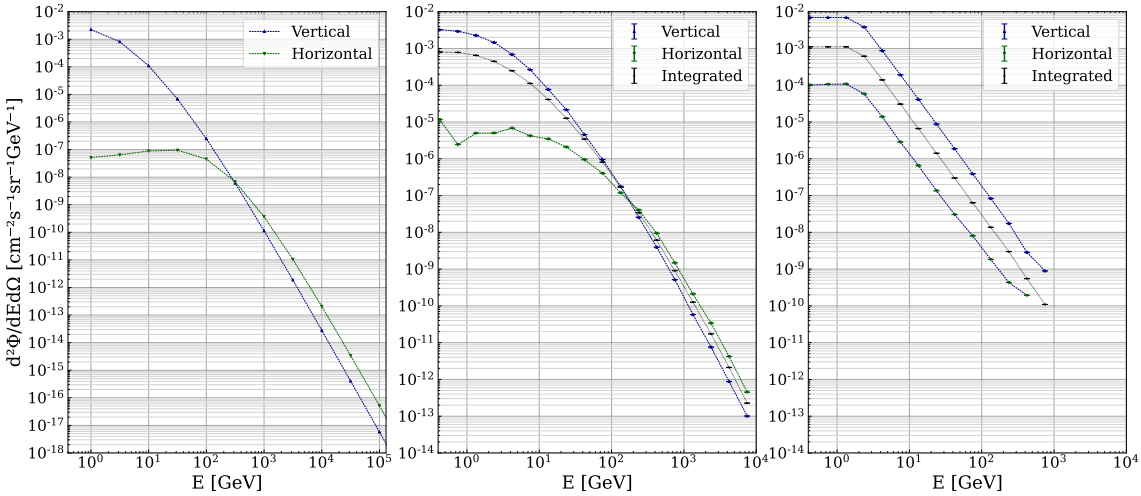

FIGURE 6.11: (left) Analytical calculation of the muon flux at sea level for vertical ($\theta = 0°$) and horizontal ($\theta = 90°$) directions [Lip93] (also shown in Figure 1.6). (center) Vertical ($0° < \theta < \sim 18°$), horizontal ($\sim 78° < \theta < 90°$), and average muon spectra at sea level obtained from the two-step simulation method. In accordance with the phase-space file generated from the first-step simulation, approximately 5×6 million muons were sampled on a plane directly above the geometry shown in Figure 6.1a. (right) Same as (center) but using the muon generator. Muons were sampled on spheres of radius 10 m with random (X, Y) centers distributed across the same geometry (-60 cm $< X <$ 60 cm and -80 cm $< Y <$ 80 cm). All simulated spectra were normalized to the expected muon flux at sea level, 170 muons·m^{-2}·s^{-1} (see Chapter 1). For the flux integrated over solid angle, values were also divided by 2π sr to match the units cm^{-2}·s^{-1}·sr^{-1}·GeV^{-1}.

The results presented so far highlight distinct strengths and limitations of the two approaches used to evaluate the differential muon flux at ground level, namely:

- the two-step method involves a longer procedure, as it first requires propagating GCRs through the atmosphere. Then, the angular distribution of the resulting muons at sea level must be corrected for Earth's curvature before being transported into a second simulation with the geometry of interest;
- the muon generator, in turn, requires only: **(i)** the number of muons to be transported, **(ii)** the radius of the spheres where these muons are placed, and **(iii)** the area over which the sphere centers are randomly distributed;
- while the vertical and horizontal muon spectra from the two-step simulation are more realistic, those from the muon generator capture only the basic features of the real spectra.

The spectra from both methods were used in simulations involving the MCS of muons in high-Z materials within medium- and large-sized geometries, and the results were similar. The following subsection compares scattering distributions obtained from each muon spectrum.

6.3.3 Scattering Angle Distribution

Scattering angle distributions for several materials were obtained using the muon flux at sea level provided by both the two-step simulation method and the muon generator. For the geometry shown in Figure 6.1a, the angular deviation of muons entering and exiting the 10 cm × 10 cm × 10 cm block between the two inner RPCs was measured. This shift corresponds to the nonprojected deflection angle θ_{space}, as introduced in Chapter 2. By defining the initial direction of motion (at the point where the muon enters the high-Z material) as the Z-axis, two orthogonal directions, X and Y, can be established, forming an orthogonal reference frame (see Figure 6.12). The vector defining the direction of the outgoing muon can then be projected onto the XZ and YZ planes. The angles between the unit vector along Z (initial muon direction) and each projection correspond to the projected angular deflections $\theta_{plane,x}$ and $\theta_{plane,y}$, respectively.

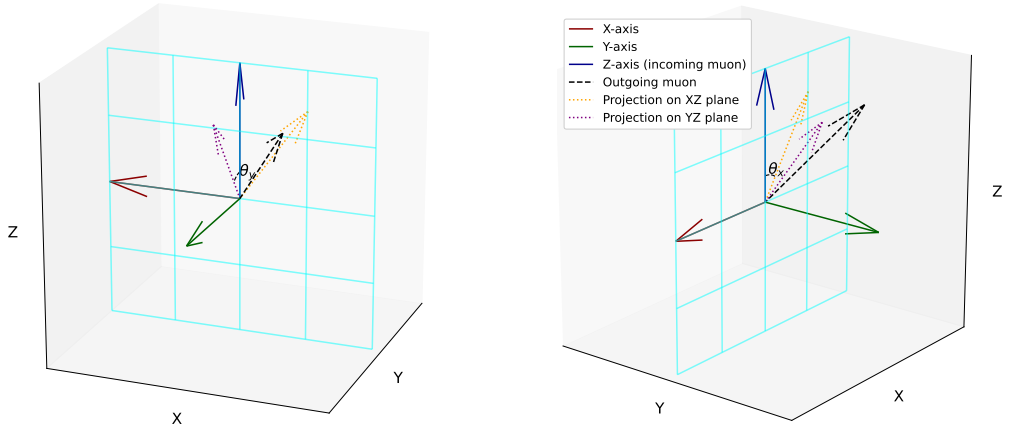

FIGURE 6.12: 3D schematic of the incoming (Z-axis aligned) and outgoing muon directions, illustrating the projected angular deflections $\theta_{plane,x}$ and $\theta_{plane,y}$ in the XZ and YZ planes, respectively. Two views, rotated about the Z-axis, are shown, with both the incoming and exiting directions positioned at the frame origin for clarity.

As mentioned in Chapter 2, the angular deflection of muons traversing a material approximately follows a normal distribution with non-Gaussian tails. The standard deviations of the $\theta_{plane,x}$ and $\theta_{plane,y}$ distributions (the projected angular distributions as defined above) can be estimated using the Lynch & Dahl formula (Equation (2.3)) as a

function of muon energy and the path length through the material. Figure 6.13 shows the distribution of the projected angular deflection $\theta_{plane,x}$ obtained using the muon flux from the two-step simulation method and from the muon generator, for a 1000 cm^3 block of uranium. It includes a Gaussian fit of the central 98% of the distribution to enable comparison with the values from the Lynch & Dahl formula. Table 6.2 additionally provides the standard deviations of Gaussian fits from simulations using blocks of various materials, along with the corresponding values from Equation (2.3). For better visualization, Figure 6.14 displays 10 randomly selected muon trajectories entering and exiting the uranium block.

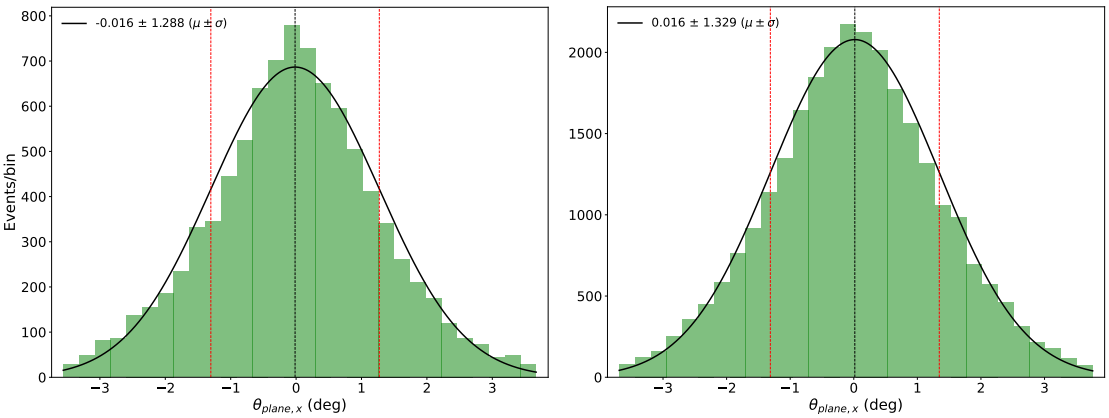

(a) (b)

FIGURE 6.13: (a) Scattering angle distribution of the projected angular deflection $\theta_{plane,x}$ for a 10 cm × 10 cm × 10 cm uranium block, using the muon flux from the two-step simulation. The muon energy, with an average of 4 GeV at sea level (see Chapter 1), was restricted to the range 3.5–4.5 GeV. The figure includes a Gaussian fit applied after trimming 1% from each tail of the distribution. (b) Same as (a), but using the muon flux from the muon generator. In both cases, $\theta_{plane,y}$ showed an almost identical distribution to $\theta_{plane,x}$.

Material	Z	Two-step sim. $\theta_{plane,x}$ (deg)	Generator $\theta_{plane,x}$ (deg)	E = 3.5 GeV θ_0 (deg)	E = 4.0 GeV θ_0 (deg)	E = 4.5 GeV θ_0 (deg)
Al	13	0.195	0.202	0.237	0.208	0.185
Fe	26	0.473	0.493	0.567	0.496	0.441
W	74	1.196	1.228	1.340	1.172	1.042
U	92	1.288	1.329	1.421	1.243	1.105

TABLE 6.2: Standard deviations from Gaussian fits of projected angular distributions for various materials, comparing simulation results (two-step and generator methods) at 3.5–4.5 GeV with values from the Lynch & Dahl formula.

As shown in the table, the simulated and calculated values are in very good agreement,

validating the simulation approach for the MST technique, whose results are presented in the next section.

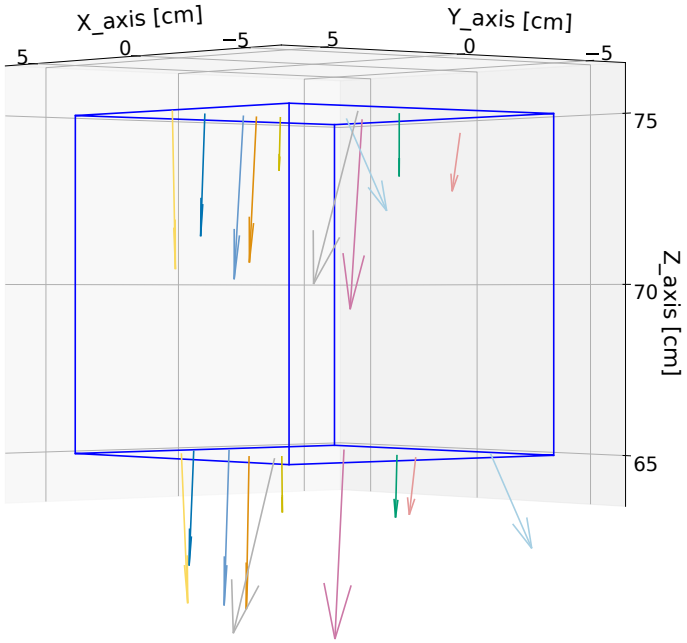

FIGURE 6.14: Example of 10 randomly selected muon trajectories entering and exiting the uranium block (two-step simulation); applied restriction: each muon must exit through the bottom face, partially limiting very short paths through the material. The arrow length provides an indication of the muon energy (3.5 to 4.5 GeV).

6.4 Simulation Results

After validating the muon spectra at sea level and the FLUKA MCS model, the impact of using RPCs with high spatial and temporal resolution on the MST technique was assessed. Several Monte Carlo simulations were conducted using the muon flux as the source term to address the following questions: **(i)** how can the effect of the detector's material budget on the scattering angle distribution be minimized? **(ii)** can the 3D reconstruction of the scanned object be improved using the TOF technique? **(iii)** how long would it take to identify high-Z materials in the medium- and large-sized geometries previously presented? The results discussed in the following subsections aim to answer these questions.

6.4.1 Effect of Material Budget on Angular Distribution

Comparing scattering angle distributions from simulations where components were progressively introduced into the geometry enabled assessment of each material's contribution to the total muon scattering. Instead of computing projected angular deflections from the direction cosines of muons entering and exiting the high-Z material, as done in the previous subsection, the full 3D angular deflections (θ_{space}) were compared by calculating muon directions before and after entering the fiducial region. Each direction was reconstructed from the two intersection positions at the locations of both pairs of RPCs, equivalent to the information that would be experimentally retrieved using a tracker of four detectors.

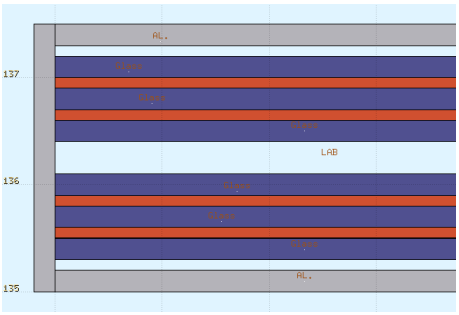

FIGURE 6.15: Cross-sectional view of the geometry implemented for each RPC. It includes a stack of 2 multi-gap RPCs with 2 gas gaps each (1 mm wide) and glass electrodes 2 mm thick, hence a total of 2×3×2 mm of glass plus 2×2 mm for the aluminium box. Z-axis positions [cm] are shown on the left. The RPC geometry corresponds to a simplified model of the tracker shown in Figure 2.7 and of the MRPCs used in this work (see layer diagram in Figure 4.14a).

For the medium-sized geometry shown in Figure 6.1a and the layer diagram in Figure 6.15, the RPCs were found to contribute significantly to the cumulative muon scattering. Figure 6.16a shows the θ_{space} distributions obtained from four different simulations, ranging from air only to the full geometry (air, RPCs, and the tungsten block). The scattering events from the simulation including only air and RPCs can be considered as 'background', since they arise from all materials except the one of interest. On the other hand, the geometry including only the high-Z object generates events exclusively due to this material, and thus corresponds to the expected 'signal'. The figure includes the ratio between events from both configurations. As it can be seen, the angular deflections caused by the tungsten block become dominant only above ∼12°, mainly due to the presence of the RPCs. With the deflections from the RPCs and air spread throughout the fiducial region, the ability to detect the high-Z material at its center is reduced. This result, combined with the detector's low spatial resolution (see Subsection 6.4.3), corroborated the

experimental observations shown in Subsection 2.2.3, where the detection of the tungsten block was improved by discarding angular deflections up to 10–11° [Sar23b], i.e., removing a substantial number of events, and consequently increasing the exposure time needed for the material detection.

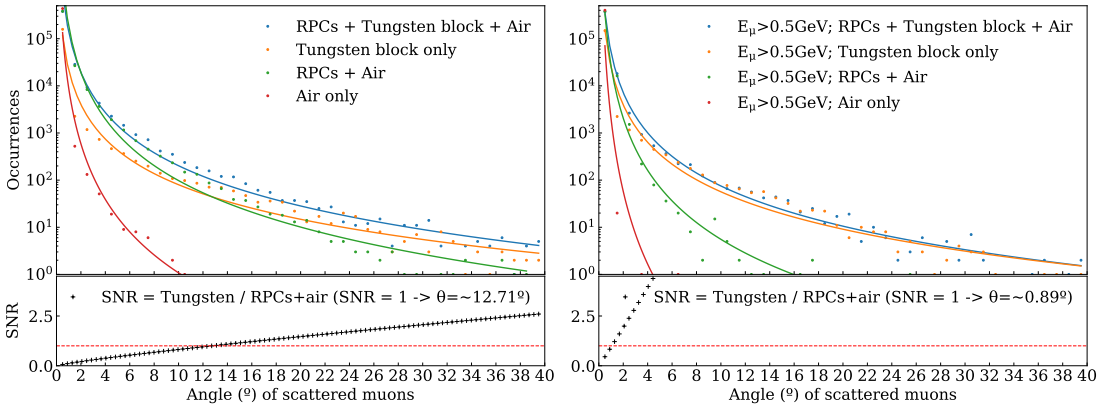

(a) (b)

FIGURE 6.16: (a) Scattering angle (θ_{space}) distributions as a function of material budget for the medium-sized geometry. The SNR is also shown, with signal from high-Z scattering and noise from background contributions (RPCs and air). (b) Same distributions but removing muons with energy up to 500 MeV. Taken from [Sar25].

The simulations also showed that, by rejecting low-energy muons (a few hundred of MeV), the angular deflections from the tungsten block become dominant over almost the entire scattering range (see Figure 6.16b). Since muons of low energy are highly scattered in all materials, even in the surrounding air, removing them improves not only the reconstructed image but also the exposure time required to detect high-Z materials, as further discussed.

6.4.2 Impact of the TOF Technique on MST

As seen in the previous subsection, low-energy muons undergo large scattering deflections in all materials. The TOF technique can be employed to discard these muons during the MST reconstruction of the scanned volume. For instance, with a time resolution of 100 ps (similar to the resolution achieved with the tRPCs used in this work), muons with energies up to ∼500 MeV and ∼1 GeV can be rejected for the medium- and large-sized geometries, respectively (see Figure 6.17).

For each muon crossing the four detector planes, the PoCA is computed as described in Chapter 2. Figure 6.18 shows the reconstructed 3D images for both geometries, with PoCAs corresponding to ∼50 minutes of acquisition plotted directly in the fiducial region.

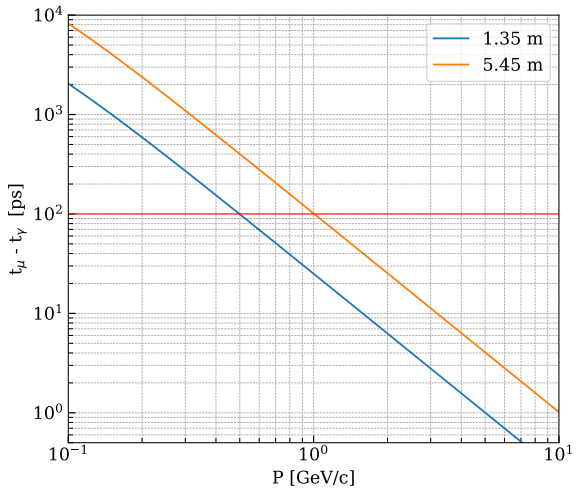

FIGURE 6.17: TOF delay of muons (relative to speed of light) as a function of momentum for distances between external RPCs of 1.35 m (medium-sized geometry) and 5.45 m (shipping container geometry).

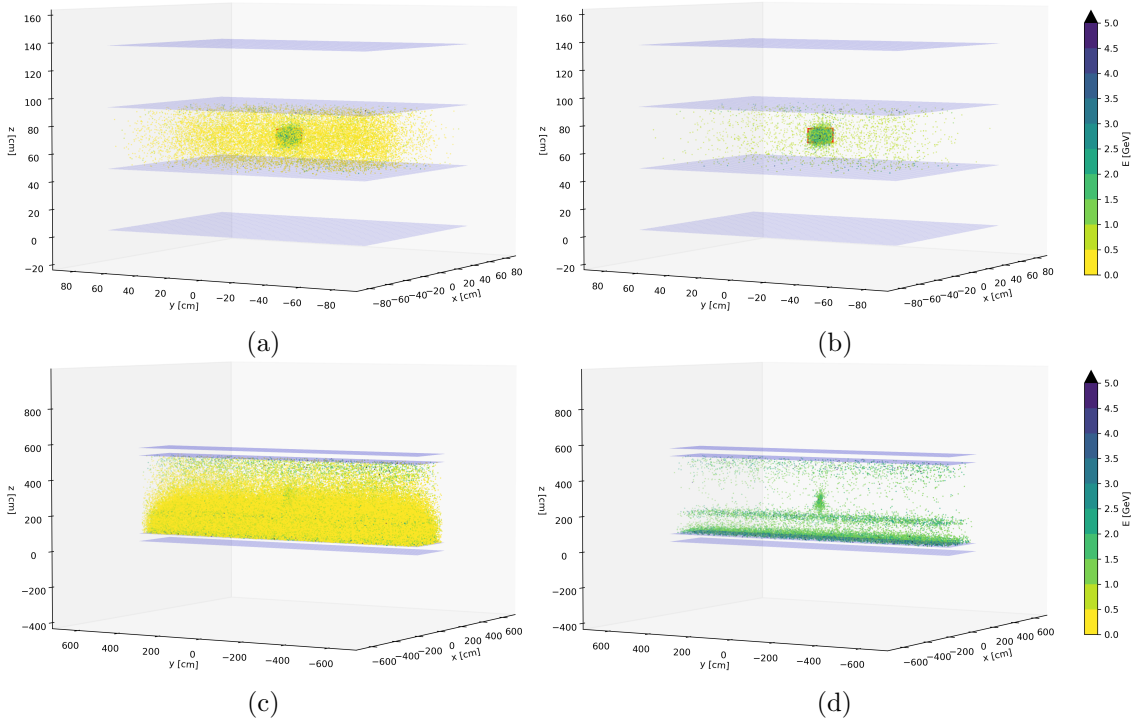

FIGURE 6.18: 3D reconstruction of the scanned volumes with PoCAs plotted directly in the fiducial region, for the medium-sized geometry (top) and the large-area geometry (bottom), both with a 1000 cm^3 tungsten block at the center. Applied restrictions: plotted only scattering angles above 1.5° (a) and 5.5° (c); removing also muons with energy below 0.5 GeV (b) and 1.0 GeV (d). Each reconstruction corresponds to an exposure time of approximately 50 minutes. [Sar24, Sar25]

Rejecting low-energy muons significantly enhances the reconstructed image of the high-Z material by reducing the spread of PoCAs across the fiducial region, while keeping most at the tungsten location. Of the 21038 PoCAs plotted in Figure 6.18a, only 13.75% (2892) are located at the tungsten position, highlighted by the red cube in the figure. After discarding muons with energies below 500 MeV (Figure 6.18b), only 5585 PoCAs remain, but almost half (2736) are located correctly.

For the large-area geometry, 390217 PoCAs were obtained within the fiducial region, of which 0.04% (146) correspond to the tungsten location (Figure 6.18c). Applying the 1 GeV energy restriction, the number of PoCAs decreased to 14749, with 0.68% (101) located at the tungsten position (Figure 6.18d). This energy cut also enabled the identification of the other structures in the geometry: the concrete floor, above it the truck deck supporting the container, and the walls of the container (better observed from a frontal perspective).

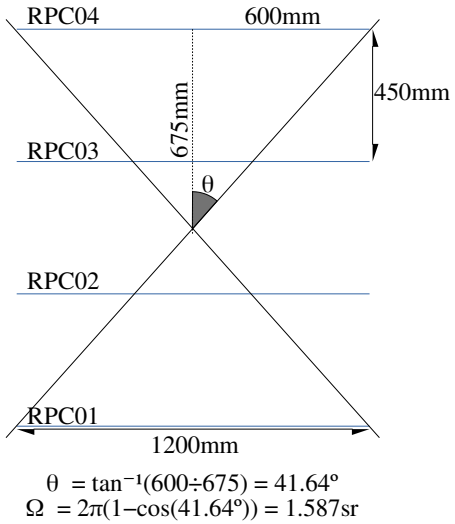

FIGURE 6.19: Angular acceptance of the tracker for the medium-sized geometry, assuming a conical aperture defined by its width. The same computation was carried out for the tracker's length.

Two methods were used to estimate the exposure time for each geometry: **i)** compute using Equation (1.3) the number of muons per minute crossing the four planes, assuming an average angular acceptance of the tracker based on its width and length, as shown in Figure 6.19. For each muon crossing the four planes corresponds one PoCA point, which can be located either inside or outside the fiducial region; **ii)** using the simulation results, calculate the ratio between the number of muons crossing all four detector planes and the average number crossing each individual plane. This ratio can then be directly multiplied by the flux over 2π sr, as given by Equation (1.3), to obtain the number of

muons per minute crossing the four planes. Similar results were obtained from both approaches, yielding ∼13000 and ∼210000 PoCAs per minute for the medium- and large-sized geometries, respectively.

The results in Figure 6.18, showing a significant reduction of PoCAs outside the high-Z region after applying a low-energy cut, highlighted the importance of the TOF technique for fast MST reconstruction. Figures 6.20 and 6.21 support this conclusion, showing MST reconstructions after only one minute of acquisition.

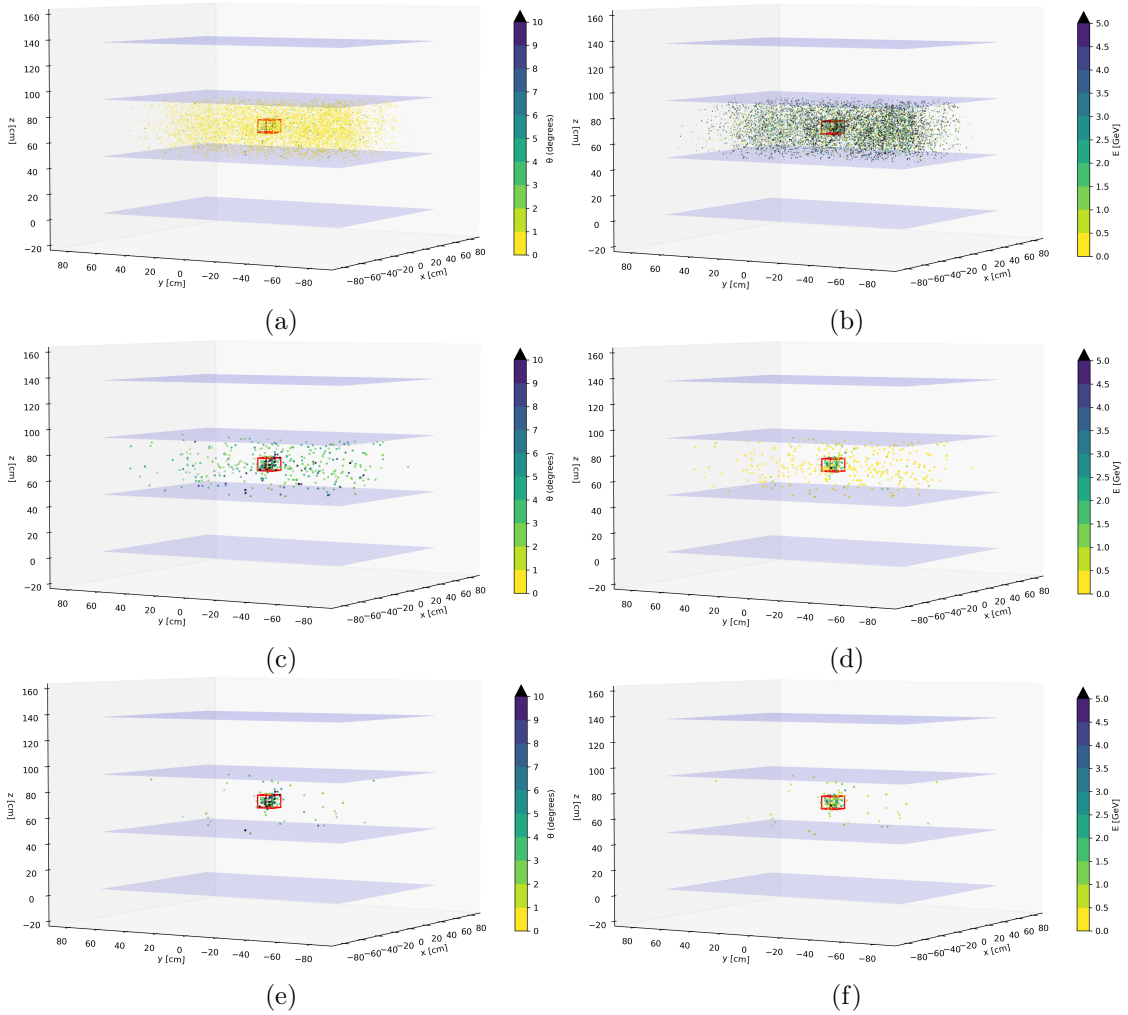

FIGURE 6.20: MST reconstruction of the medium-sized geometry after one minute of acquisition, with colors scaled by scattering angle (left) and muon energy (right). (a) & (b) Without any restriction, 8902 PoCAs were obtained in the fiducial region, with 2.11% (188) at the tungsten location. (c) & (d) Requiring a scattering angle greater than 2.0°, 411 PoCAs were obtained, 17.52% (72) at the correct location. (e) & (f) Also filtering out muons with energies below 500 MeV, 128 PoCAs remained, 51.56% (66) at the correct location of the tungsten block.

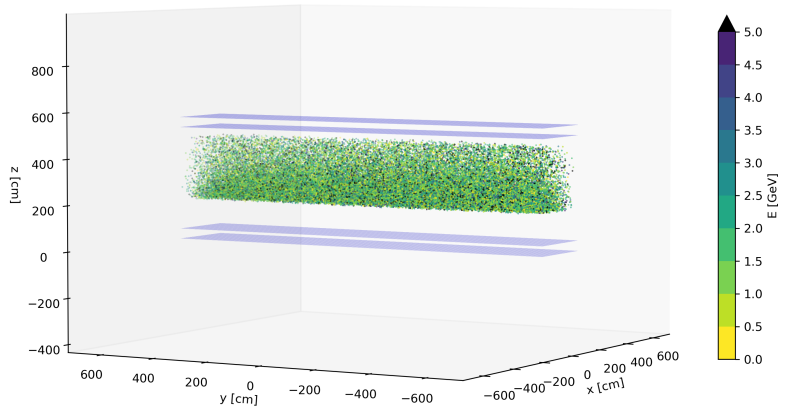

(a)

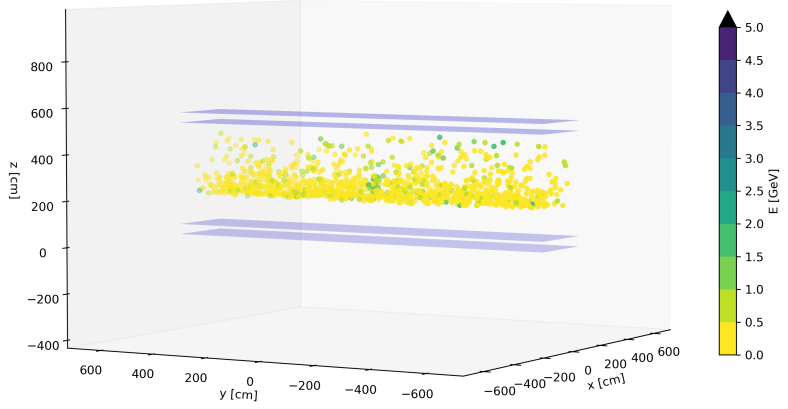

(b)

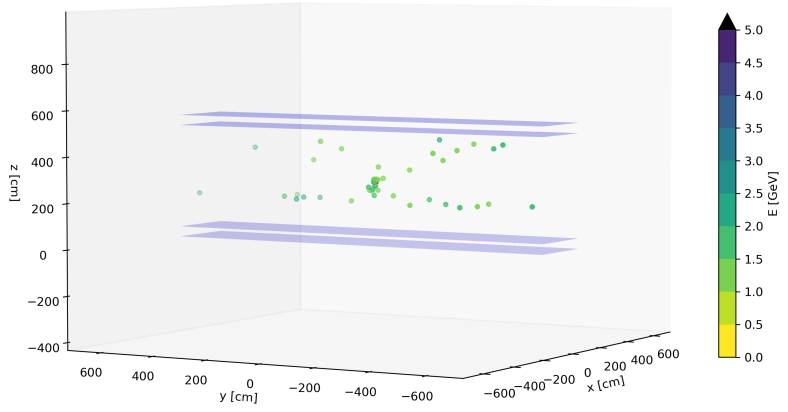

(c)

FIGURE 6.21: MST reconstruction of the shipping container after one minute of acquisition, showing only PoCAs within the container. (a) Without any restriction, 57651 PoCAs plotted, 0.02% (14) within the tungsten region. (b) Requiring a scattering angle greater than 5.5°, 1289 PoCAs obtained, 0.31% (4) at the correct location. PoCA point sizes were increased for better visibility. (c) Also filtering out muons with energies below 1 GeV, 44 PoCAs remained, 4.55% (2) at the correct location.

Despite only two PoCAs remaining at the tungsten block location after applying the 5.5° and 1 GeV restrictions (Figure 6.21c), the concentration of PoCAs in the surrounding area clearly indicates its presence in the container. However, for such large objects, voxelizing the scanned volume – plotting voxels with PoCAs above a given threshold instead of individual PoCAs – can improve visualization, as discussed in the next subsection.

A final illustration is given in Figure 6.22, showing the frontal view of the container, truck deck, and concrete floor after 1 and 50 minutes of acquisition. Figure 6.22b shows the distribution of PoCAs clearly extending beyond the boundaries of the tungsten block, especially in the vertical direction. The PoCA algorithm relies on the single-scattering approximation, which, in large geometries with superimposed materials, leads to the observed vertical elongation of the PoCA distribution [Sch03]. Other models could be used to improve the MST reconstruction, a topic beyond the scope of this document.

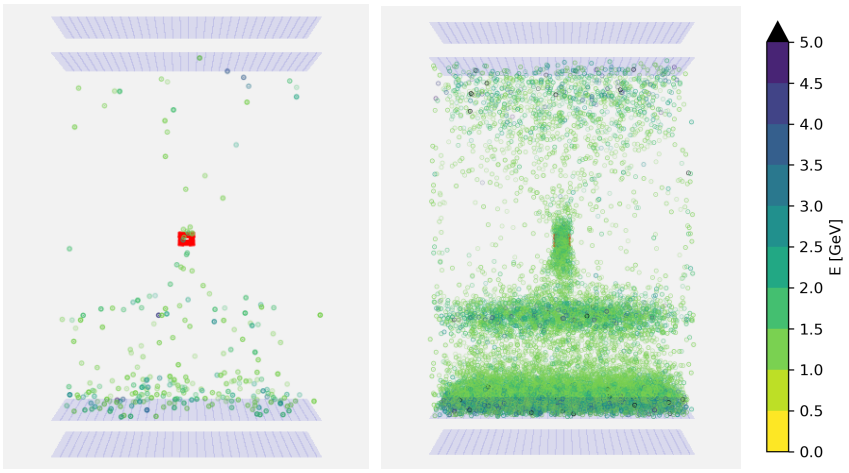

(a) (b)

FIGURE 6.22: MST reconstruction of the large-area geometry (frontal view) after 1 minute (a) and 50 minutes (b) of acquisition.

6.4.3 Time Required to Detect the Tungsten Block

To estimate the exposure time required to identify the tungsten block in both tested geometries for different RPC spatial resolutions, the following approach was established:

i) discretize the fiducial region into voxels: 5 cm × 5 cm × 5 cm for the medium-sized geometry and 10 cm × 10 cm × 10 cm for the shipping container geometry;

ii) apply Gaussian smearing to the muon positions at each detector plane to emulate the RPC's spatial resolution;

iii) compute the PoCAs according to the specified scattering and energy restrictions, and assign them to the corresponding voxels;

iv) identify voxels with the highest PoCA counts using different metrics: **(1)** the percentage of PoCAs per voxel relative to the total count, **(2)** the ratio between the voxel value and the mean, and **(3)** the standardized value $(N-\mu)/\sigma$, which indicates how far a voxel's value N deviates from the mean μ in units of standard deviation σ;

v) reduce the time of acquisition and repeat all the above steps.

The tungsten block is considered to have been detected for a given acquisition time if the voxels with the highest PoCA counts coincide with its location. Another indication of the high-Z material's presence is the clustering of voxels with PoCAs in this region, even if each contains a few PoCAs. This situation typically arises at very low exposure times, when only a few muons have traversed each voxel.

To remove PoCAs mostly related with the detector planes or, for instance, the 15 cm-thick concrete floor in the large-area geometry, an optional control run can be performed by including only these elements in the geometry. The number of PoCAs per voxel obtained in the control run can then be subtracted from the corresponding voxels of the main run before analyzing the PoCA distribution. In a real-world scenario, this would correspond to an MST scan e.g. without a truck in the scanned volume, or with the same type of truck but with an empty container.

Figure 6.23 shows the maximum values of PoCA counts per voxel (in σ units) as a function of acquisition time, for the medium-sized geometry and various spatial resolutions. These normalized values are provided for two regions within the fiducial volume: at the correct location of the high-Z material, and outside it. No scattering angle or energy restrictions were applied, as the values at the tungsten location were already significantly higher than those outside that region. The exception was the detector with 1 cm spatial resolution. In this case, the simulation shows that the number of PoCAs per voxel inside and outside the correct location are not substantially different, indicating a serious limitation for a detector with this resolution to detect a 1000 cm^3 tungsten block, especially for acquisition times below 10 minutes[1]. Additionally, the comparison of the results for 0.3 mm and 1 mm spatial resolutions indicates that achieving submillimeter resolution does not significantly enhance the detector's ability to detect the high-Z material.

[1]the detector used for the MST scan of 2021 (see Subsection 2.2.3) was thus negatively affected by its centimeter spatial resolution.

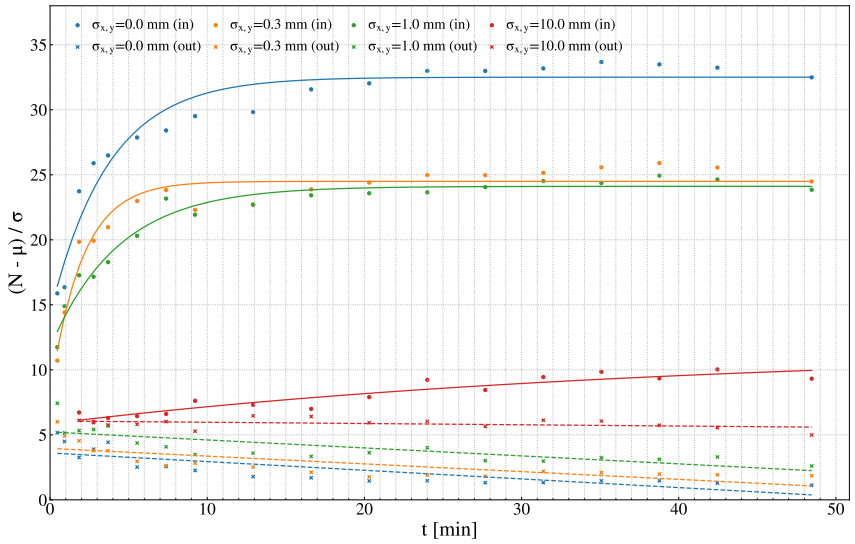

FIGURE 6.23: Maximum standardized PoCA counts per voxel as a function of acquisition time, for various RPC spatial resolutions in the medium-sized geometry. Two values are plotted per exposure time and resolution: one corresponding to the tungsten block location (in), and the other to the region outside it (out). All sets of values were fitted with either exponential or linear functions. The volume attributed to the tungsten's location includes a 5 cm margin around it.

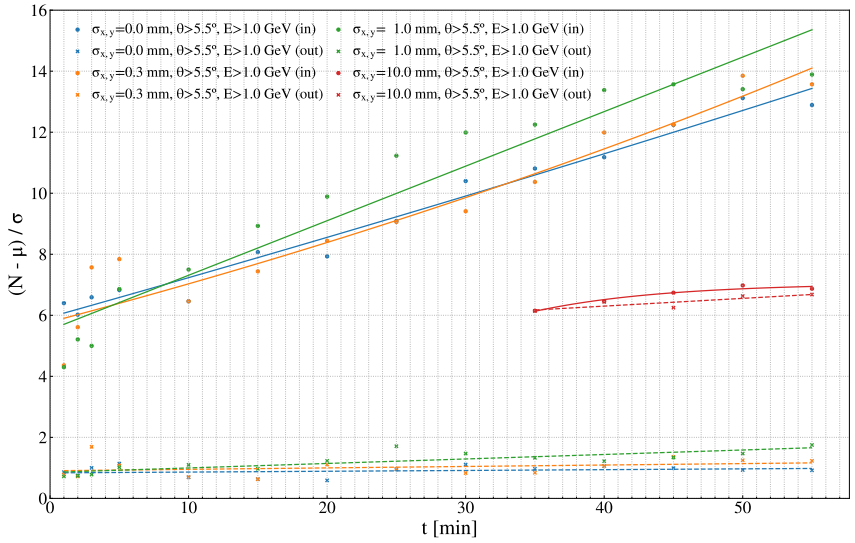

FIGURE 6.24: Maximum standardized PoCA counts per voxel as a function of acquisition time, for various RPC spatial resolutions in the shipping container geometry. As in the previous figure, two values are plotted per exposure time and resolution: one for the tungsten block location (in) and one for the region outside it (out). The volume attributed to the tungsten block's location includes a 15 cm margin in the horizontal plane (X, Y) and 45 cm vertically (Z), accounting for the vertical elongation artifact of PoCA points caused by the PoCA algorithm (see Figure 6.22b).

Figure 6.24, in turn, shows the maximum normalized PoCA counts per voxel for the large-area geometry. Scattering angle and energy restrictions were applied to increase the separation between the maximum number of counts inside and outside the tungsten block location, thereby enhancing its visualization. However, even with the 5.5° scattering angle and 1.0 GeV energy restrictions, the detector with 1 cm spatial resolution is unable to identify the 1000 cm^3 tungsten block, including for long exposure times. The solution in this case would be to increase the applied restrictions, at the cost of further reducing the muon statistics. As seen before, there is no improvement in detecting the high-Z material when comparing millimeter and submillimeter resolutions.

Figures 6.25 and 6.26 present two examples of MST scans using the voxelization technique, where the plotted voxels are limited based on the normalized PoCA counts per voxel. Both figures show exposure times of one and two minutes for the ideal and 1.0 mm spatial resolutions, respectively.

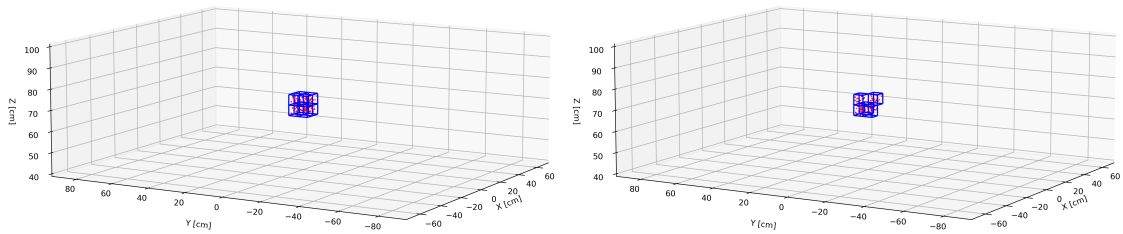

(a) (b)

FIGURE 6.25: MST reconstruction of the medium-sized geometry after one and two minutes of acquisition using the voxelization technique. (a) One minute of acquisition with ideal spatial resolution (0.0 mm), showing only voxels with normalized PoCA counts per voxel above 7σ. (b) Two minutes of acquisition with 1.0 mm spatial resolution, also showing only voxels with normalized PoCA counts per voxel above 7σ.

Figure 6.25a shows the scan result of the medium-sized geometry after one minute of acquisition with ideal spatial resolution. No scattering angle or energy restrictions were applied, but according to Figure 6.23, a threshold of 7σ was set on the normalized PoCA counts per voxel. As a result, only voxels at the correct location of the tungsten block are plotted, while all voxels with PoCA counts below this threshold (7σ above the mean) are discarded. The result for two minutes of acquisition and 1 mm spatial resolution is shown in Figure 6.25b, where the same threshold was applied.

With respect to the shipping container geometry, as shown in Figures 6.26a and 6.26c, after one and two minutes of acquisition applying the 5.5° scattering angle and 1.0 GeV energy restrictions, the clustering of voxels with PoCAs at the tungsten location already indicates its presence at the center of the container.

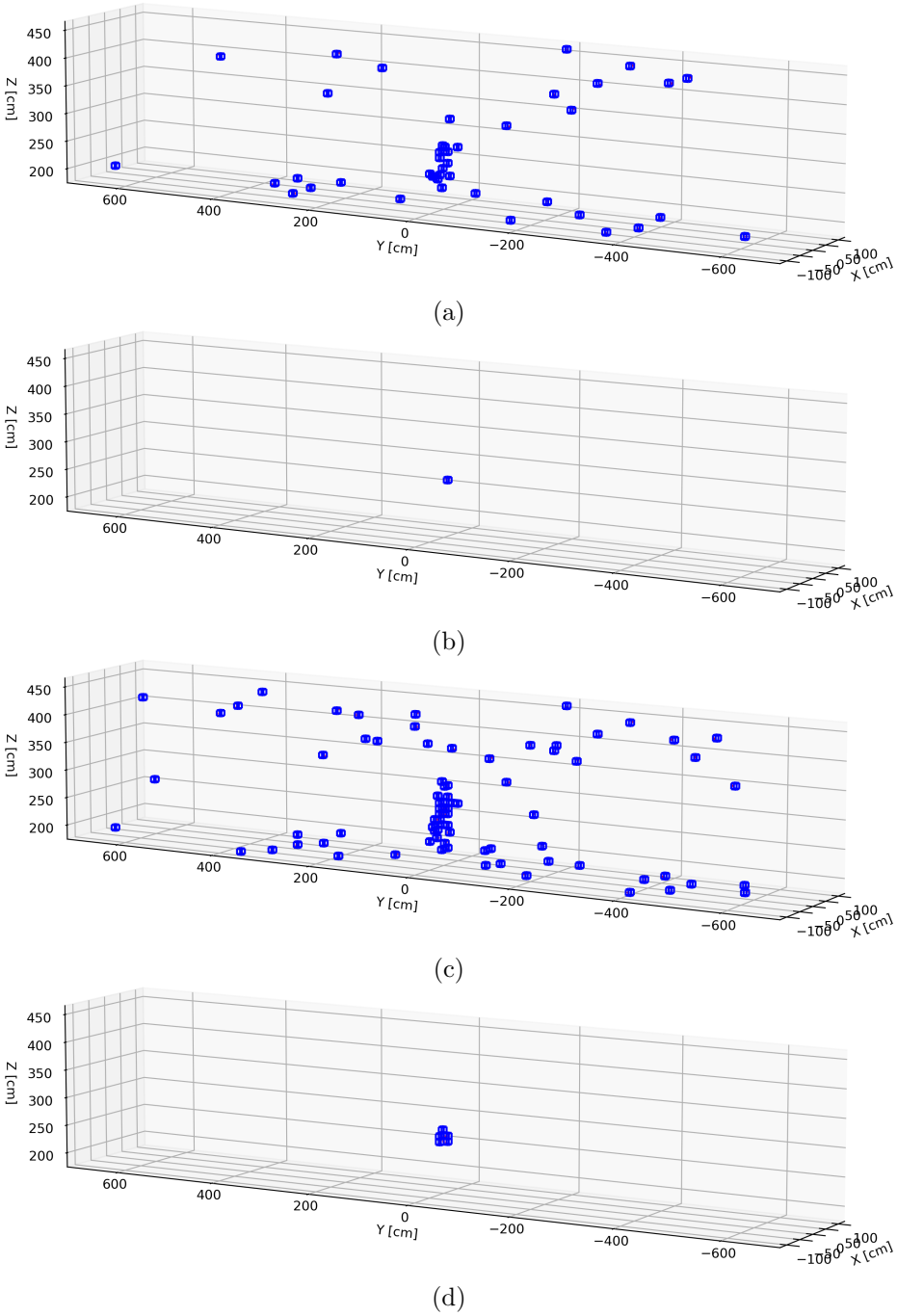

FIGURE 6.26: MST reconstruction of the shipping container after one and two minutes of acquisition using the voxelization technique. Applied restrictions: scattering angle $> 5.5°$ and muon energy > 1.0 GeV. (a) One minute of acquisition with ideal spatial resolution (0.0 mm). (b) Same as (a) but showing only voxels with normalized PoCA counts per voxel above 2σ. (c) Two minutes of acquisition with 1.0 mm spatial resolution. (d) Same as (c), but showing only voxels with normalized PoCA counts per voxel above 2σ.

As performed before, setting a threshold on normalized PoCA counts per voxel (2σ) enhances tungsten block detection, since only voxels with counts above this threshold are plotted (see Figures 6.26b and 6.26d).

The results in the previous figures show that one minute of acquisition time is sufficient to detect the 1000 cm^3 tungsten block in both simulated geometries. High-Z material detection can be enhanced by voxelizing the scanned volume, as it allows additional rejection based on the number of PoCAs per voxel. It was also observed that, especially for the large-area geometry, the TOF technique plays a key role in enabling the reconstruction of the scanned object after just one minute of acquisition by discarding muons with energies below 1 GeV. In both cases, a millimeter spatial resolution was shown to be adequate for the MST technique.

Conclusion and Outlook

High spatial and temporal resolution, combined with the relative ease of construction at low cost, make timing Resistive Plate Chambers (tRPCs) particularly well suited for muon detection across large areas. Given that the Front-End Electronics (FEE) dominates the overall cost of these detectors, a readout encoding scheme was developed to decouple the number of FEE channels from the detector area. The method relies on a Signal Merging Printed Circuit Board (SMPCB), which combines signals from multiple readout strips in parallel before feeding them to preamplifiers.

Several SMPCBs connected in a daisy-chain configuration enabled the use of only 48 electronic channels to instrument 888 strips on a 130×90 cm^2 tRPC. Without signal multiplexing, a detector with the same strip pitch (2.54 mm) and number of channels (48) would have been limited to a sensitive area over 300 times smaller (6×6 cm^2).

Each electronic channel was connected to as many as 22 strips in parallel, corresponding to a total strip length of approximately 20 m. Despite the increased capacitance and electronic noise per transmission line, submillimeter 2D spatial resolution was achieved during cosmic-ray measurements. The time resolution, after time-walk correction, reached 89 ps (σ), improving steadily to 73 ps (σ) over the final 10 days of acquisition.

The ambiguity introduced by grouping strips in parallel is resolved by adding a readout layer with wide strips (6 cm pitch), which simultaneously provides coarse 2D positional information and timing capabilities. As a result, only a partial decoupling is achieved with the proposed encoding scheme – a residual increase in the number of FEE channels with detector area remains, resulting from the very large strip pitch of the additional readout electrode.

The primary contributions of this work lie in the development and testing of the SMPCB-based readout encoding scheme. Comprehensive tests with 30×30 cm^2 prototypes and the 130×90 cm^2 detector demonstrated that the proposed signal multiplexing approach enables sub-1 mm 2D spatial resolution and sub-100 ps time resolution in high-efficiency tRPCs with areas above 1 m^2, along with a one order of magnitude reduction in electronic channels.

In addition, FLUKA Monte Carlo simulations were carried out to evaluate the use of tRPCs with high spatial and temporal resolution for scanning very large volumes (150 m^3) through the Muon Scattering Tomography (MST) technique. Simulations showed that 1 minute of acquisition time is sufficient to detect a $10 \times 10 \times 10$ cm^3 tungsten block inside a large shipping container. tRPCs with millimeter-scale spatial resolution proved adequate for this muon imaging method. In turn, the timing capabilities of these detectors were shown to play a significant role in discarding low-energy muons up to 1 GeV, enhancing high-Z material discrimination after just 1 minute of acquisition.

A medium-sized volume of 1 m^3 was also simulated and compared with experimental results from an MST scan performed using a 2 m^2 muon tracker, underlining the importance of millimeter-scale spatial resolution. In this case, the ability to reject low-energy muons up to 500 MeV using the Time Of Flight (TOF) technique was confirmed to be a clear advantage.

Future studies may address a potential limitation of the proposed SMPCB-based multiplexing technique by extending the detector area, for instance by doubling the area covered by the readout electrodes to $\sim$2.5 m^2. Each detector plane for a large-scale cargo scanning system could then be built by arranging fourteen 1×2.5 m^2 tRPC modules side by side to horizontally cover the full scanning area.

Another possible development would be to simplify the setup required by this multiplexing technique by removing the readout electrode with wide strips and using only one tRPC at the center of the stack. The coarse 2D position of each event, needed to identify the impinged group of thin strips, could in principle be obtained directly from one of the thin-strip readout electrodes by using an optimized SMPCB. This could be achieved by splitting the signals induced in the thin strips, routing the electronic component to current-sensitive amplifiers to provide the time and coarse 2D position of the events, while directing the ionic component to charge-sensitive amplifiers to yield the corresponding fine position. This approach would reduce the detector's material budget by half while providing the same information as the setups tested in the present work. Nevertheless, some impact on time resolution can already be anticipated, as only a single tRPC module would contribute to the prompt component of the signals.

Acknowledgements

Driven by an interest in the use of RPCs for muon imaging, R&D activities were undertaken by our group, culminating in the present work.

Firstly, I would like to thank the board of LIP – Laboratory of Instrumentation and Experimental Particle Physics for this opportunity and for supporting me in pursuing it.

This work would not have been possible without the efforts of many colleagues at LIP, ranging from the construction of the tested detectors and electronics design to the scientific exchanges that contributed to the project.

A special thanks to the RPC group, namely Alberto Blanco, Luís Lopes and Paulo Fonte, and to the personnel of the detector laboratory and the mechanical workshop of LIP for their valuable work.

For the FLUKA simulations, insightful discussions were held with former colleagues from CERN, in particular with members of the R2E team (STI group) and the RP group, as well as from the Brookhaven National Laboratory (Radiological Control Division). Their support and expertise are gratefully acknowledged.

To conclude, I am deeply grateful to my family for their presence, support, and patience throughout this journey.

References

[Abb18] M. Abbrescia, V. Peskov, and P. Fonte. *Resistive Gaseous Detectors*. Wiley-VCH, 2018. ISBN 978-3-527-34076-7. 42, 67, 71, 103

[Abe00] K. Abe, F. Handa, I. Higuchi, et al. *Performance of glass RPC operated in streamer mode with SF6 gas mixture. Nuclear Instruments and Methods in Physics Research Section A: Accelerators, Spectrometers, Detectors and Associated Equipment*, 455(2):397–404, 2000. doi:10.1016/S0168-9002(00)00518-0. 67

[Afo22] L. Afonso, I. Alexandre, S. Andringa, et al. *Muography in the university and in the museum. Journal of Advanced Instrumentation in Science*, (278), 2022. doi:10.31526/JAIS.2022.278. 15

[Ahd22] C. Ahdida, D. Bozzato, D. Calzolari, et al. *New capabilities of the FLUKA multi-purpose code. Frontiers in Physics*, 9, 2022. ISSN 2296-424X. doi:10.3389/fphy.2021.788253. 106

[Aie13] G. Aielli, M. Bindi, and A. Polini. *Performance, operation and detector studies with the ATLAS resistive plate chambers. Journal of Instrumentation*, 8(02):P02020, 2013. doi:10.1088/1748-0221/8/02/P02020. 1

[Aie14] G. Aielli, R. Cardarelli, L. D. Stante, et al. *The RPC space resolution with the charge centroid method. Journal of Instrumentation*, 9(09):C09030, 2014. doi:10.1088/1748-0221/9/09/C09030. 94

[Aki09] A. Akindinov, A. Alici, P. Antonioli, et al. *Final test of the MRPC production for the ALICE TOF detector. Nuclear Instruments and Methods in Physics Research Section A: Accelerators, Spectrometers, Detectors and Associated Equipment*, 602(3):709–712, 2009. doi:10.1016/j.nima.2008.12.095. 1

[Alv70] L. Alvarez, J. Anderson, F. E. Bedwei, et al. *Search for hidden chambers in the pyramids. Science*, 167, 1970. 14, 15

[An08] S. An, Y. Jo, J. Kim, et al. *A 20 ps timing device – a multigap resistive plate chamber with 24 gas gaps. Nuclear Instruments and Methods in Physics Research Section A: Accelerators, Spectrometers, Detectors and Associated Equipment*, 594(1):39–43, 2008. doi:10.1016/j.nima.2008.06.013. 26, 66

[Bab56] M. V. Babykin, A. G. Plakhov, Y. F. Skachkov, et al. *Plane-parallel spark counters for the measurement of small times. The Soviet Journal of Atomic Energy*, 1(4):487–494, 1956. doi:10.1007/BF01479848. 24

[Bad96] G. Badhwar and P. O'Neill. *Galactic cosmic radiation model and its applications. Advances in Space Research*, 17(2):7–17, 1996. doi:10.1016/0273-1177(95)00507-B. 109

[Bae24] O. Baeyer and W. Kutzner. *Versuche mit der glimmlampe als zählkammer. Zeitschrift für Physik*, 21(1):46–49, 1924. doi:10.1007/BF01328246. 23

[Bae12] P. Baesso, D. Cussans, J. Davies, et al. *High resolution muon tracking with resistive plate chambers. Journal of Instrumentation*, 7(11):P11018, 2012. doi:10.1088/1748-0221/7/11/P11018. 21

[Bat07] G. Battistoni, F. Cerutti, A. Fasso, et al. *The FLUKA code: description and benchmarking. AIP Conference Proceedings*, 896(1):31–49, 2007. doi:10.1063/1.2720455. 108

[Bat15] G. Battistoni, T. Boehlen, F. Cerutti, et al. *Overview of the FLUKA code. Annals of Nuclear Energy*, 82:10–18, 2015. doi:10.1016/j.anucene.2014.11.007. 106, 108

[Bel10] D. Belver, P. Cabanelas, E. Castro, et al. *Performance of the low-jitter high-gain/bandwidth front-end electronics of the HADES tRPC wall. IEEE Transactions on Nuclear Science*, 57(5):2848–2856, 2010. doi:10.1109/TNS.2010.2056928. 58, 59

[BIP19] BIPM. *The International System of Units (SI)*. BIPM - International Bureau of Weights and Measures, 2019. ISBN 978-92-822-2272-0. 13

[Bla12] A. Blanco, P. Fonte, L. Lopes, et al. *TOFtracker: gaseous detector with bidimensional tracking and time-of-flight capabilities. Journal of Instrumentation*, 7(11):P11012, 2012. doi:10.1088/1748-0221/7/11/P11012. 26, 74

[Bla25] A. Blanco, M. Carvalho, S. Fetal, et al. *Characterization of sealed (zero gas flow) rpcs under strong irradiation. Nuclear Instruments and Methods in Physics Research Section A: Accelerators, Spectrometers, Detectors and Associated Equipment*, 1080:170743, 2025. doi:10.1016/j.nima.2025.170743. 26

[Bor03] K. N. Borozdin, G. E. Hogan, C. Morris, et al. *Radiographic imaging with cosmic-ray muons. Nature*, 422:277, 2003. 21

[Cam98] P. Camarri, R. Cardarelli, A. D. Ciaccio, et al. *Streamer suppression with SF6 in RPCs operated in avalanche mode. Nuclear Instruments and Methods in Physics Research Section A: Accelerators, Spectrometers, Detectors and Associated Equipment*, 414(2):317–324, 1998. doi:10.1016/S0168-9002(98)00576-2. 67

[Car93] R. Cardarelli, A. D. Ciaccio, and R. Santonico. *Performance of a resistive plate chamber operating with pure CF3Br. Nuclear Instruments and Methods in Physics Research Section A: Accelerators, Spectrometers, Detectors and Associated Equipment*, 333(2):399–403, 1993. doi:10.1016/0168-9002(93)91182-M. 25

[Car13] C. Carloganu, V. Niess, S. Béné, et al. *Towards a muon radiography of the Puy de Dôme. Geoscientific Instrumentation Methods and Data Systems*, 2(1):55–60, 2013. doi:10.5194/gi-2-55-2013. 15

[CER] CERN. *FLUKA website*. `https://fluka.cern`. Accessed: 2025-06-01. 108, 109

[Chr71] L. G. Christophorou. *Atomic and Molecular Radiation Physics*. Wiley-Interscience, 1971. ISBN 0-471-15629-9. 31

[Cur36] S. C. Curran. *XLVII. The use of high-frequency discharge-tubes as electrical counters. The London, Edinburgh, and Dublin Philosophical Magazine and Journal of Science*, 22(148):599–616, 1936. doi:10.1080/14786443608561712. 23

[Cur54] S. C. Curran. *The new counters. Science Progress (1933-)*, 42(165):32–45, 1954. ISSN 00368504, 20477163. 23

[Dai15] J. S. Dai. *Euler–Rodrigues formula variations, quaternion conjugation and intrinsic connections. Mechanism and Machine Theory*, 92:144–152, 2015. doi:10.1016/j.mechmachtheory.2015.03.004. 113

[Dav73] A. J. Davies and C. J. Evans. *The theory of ionization growth in gases under pulsed and static fields*. CERN-73-10. CERN. Geneva, 1973. doi:10.5170/CERN-1973-010. 36, 38

[Dec] Decision Sciences. *Decision Sciences website*. `https://www.decisionsciences.com/`. Accessed: 2025-01-01. 21

[Edw16] T. Edwards and M. Steer. *Foundations for Microstrip Circuit Design*. John Wiley & Sons, 4th edition, 2016. ISBN 978-11-189-3619-1. 51, 85

[Eva55] R. Evans. *The Atomic Nucleus*. McGraw-Hill, 1955. 16

[Fas97] A. Fasso, A. Ferrari, J. Ranft, et al. *An update about FLUKA*, 1997. 108

[Fed78] G. V. Fedotovich, Y. N. Pestov, and K. N. Putilin. *Spark counter with a localized discharge. Novosibirsk group, Institute of Nuclear Physics USSR*, 1978. 24

[Fer92] A. Ferrari, P. R. Sala, R. Guaraldi, et al. *An improved multiple scattering model for charged particle transport. Nuclear Instruments and Methods in Physics Research Section B: Beam Interactions with Materials and Atoms*, 71(4):412–426, 1992. doi:10.1016/0168-583X(92)95359-Y. 108

[Fer97] A. Ferrari and P. R. Sala. *The Physics of High Energy Reactions.* Technical report, CERN, Geneva, 1997. 8

[Fis91] H. Fischle, J. Heintze, and B. Schmidt. *Experimental determination of ionization cluster size distributions in counting gases. Nuclear Instruments and Methods in Physics Research Section A: Accelerators, Spectrometers, Detectors and Associated Equipment*, 301(2):202–214, 1991. doi:10.1016/0168-9002(91)90460-8. 33, 34

[Fon00] P. Fonte, R. F. Marques, J. Pinhão, et al. *High-resolution RPCs for large TOF systems. Nuclear Instruments and Methods in Physics Research Section A: Accelerators, Spectrometers, Detectors and Associated Equipment*, 449(1):295–301, 2000. doi:10.1016/S0168-9002(99)01299-1. 25, 66

[Fon02a] P. Fonte. *Applications and new developments in resistive plate chambers. IEEE Transactions on Nuclear Science*, 49(3):881–887, 2002. doi:10.1109/TNS.2002.1039583. 42

[Fon02b] P. Fonte and V. Peskov. *High-resolution TOF with RPCs. Nuclear Instruments and Methods in Physics Research Section A: Accelerators, Spectrometers, Detectors and Associated Equipment*, 477(1):17–22, 2002. doi:10.1016/S0168-9002(01)01914-3. 42

[Fon13] P. Fonte. *Frequency-domain formulation of signal propagation in multistrip resistive plate chambers and its low-loss, weak-coupling analytical approximation. Journal of Instrumentation*, 8(08):1–15, 2013. doi:10.1088/1748-0221/8/08/P08007. 51

[GD11] D. Gonzalez-Diaz, H. Chen, and Y. Wang. *Signal coupling and signal integrity in multi-strip resistive plate chambers used for timing applications. Nuclear Instruments and Methods in Physics Research Section A: Accelerators, Spectrometers, Detectors and Associated Equipment*, 648(1):52–72, 2011. doi:10.1016/j.nima.2011.05.039. 85

[GD17] D. Gonzalez-Díaz, F. Palomo, J. González, et al. *Detectors and concepts for sub-100 ps timing with gaseous detectors. Journal of Instrumentation*, 12(03):C03029, 2017. doi:10.1088/1748-0221/12/03/C03029. 43

[Gei13] H. Geiger and E. Marsden. *The laws of deflexion of α particles through large angles. Philosophical Magazine*, 25(604), 1913. 16

[Geo55] E. P. George. *Cosmic rays measure overburden of tunnel. Commonwealth Engineer*, pages 455–457, 1955. 13, 14

[Geo09] J. S. George, K. A. Lave, M. E. Wiedenbeck, et al. *Elemental composition and energy spectra of galactic cosmic rays during solar cycle 23. The Astrophysical Journal*, 698(2):1666–1681, 2009. doi:10.1088/0004-637x/698/2/1666. 4

[Got93] B. Gottschalk, A. Koehler, R. Schneider, et al. *Multiple Coulomb scattering of 160 MeV protons. Nuclear Instruments and Methods in Physics Research B*, 74:467–490, 1993. 16

[Gri01] P. Grieder. *Cosmic rays at Earth.* Elsevier, 2001. 8, 10

[Gri10] P. Grieder. *Extensive air showers.* Springer, 2010. 9

[GSI] GSI. *TRB website.* `http://trb.gsi.de/`. Accessed: 2025-01-01. 61

[Hes12] V. Hess. *Über beobachtungen der durchdringenden strahlung bei sieben freiballonfahrten. Physikalische Zeitschrift*, 13:1084–1091, 1912. 4

[Jor94] V. T. Jordanov and G. F. Knoll. *Digital synthesis of pulse shapes in real time for high resolution radiation spectroscopy. Nuclear Instruments and Methods in Physics Research Section A: Accelerators, Spectrometers, Detectors and Associated Equipment*, 345(2):337–345, 1994. doi:10.1016/0168-9002(94)91011-1. 56

[Keu49] J. W. Keuffel. *Parallel-plate counters. Review of Scientific Instruments*, 20(3):202–208, 1949. doi:10.1063/1.1741489. 23

[Leo94] W. Leo. *Techniques for Nuclear and Particle Physics Experiments.* Springer-Verlag, 1994. 13, 16, 17, 77, 83, 85, 88

[Lip93] P. Lipari. *Lepton spectra in the Earth's atmosphere. Astroparticle Physics*, 1(2):195–227, 1993. doi:10.1016/0927-6505(93)90022-6. 10, 119, 120

[LXC] LXCat. *BOLSIG+ solver ver. 03/2016.* `www.lxcat.net`. Accessed: 2025-05-01. 36, 37

[Lyn91] G. R. Lynch and O. I. Dahl. *Approximations to multiple Coulomb scattering. Nuclear Instruments and Methods in Physics Research B*, 58:6–10, 1991. 16, 17

[Mad48] L. Madansky and R. W. Pidd. *Characteristics of the parallel-plate counter. Phys. Rev.*, 73(10):1215–1216, 1948. doi:10.1103/PhysRev.73.1215. 23

[Mee53] J. M. Meek and J. D. Craggs. *Electrical breakdown of gases.* Oxford University Press, 1953. doi:10.1002/qj.49708034425. 38

[Men16] E. L. Menedeu. *RPC application in muography and specific developments. Journal of Instrumentation*, 11(06):C06009–C06009, 2016. doi:10.1088/1748-0221/11/06/c06009. 15

[Mor17] K. Morishima, M. Kuno, A. Nishio, et al. *Discovery of a big void in khufu's pyramid by observation of cosmic-ray muons. Nature*, 552:386–390, 2017. doi:10.1038/nature24647. 15

[NAS07] NASA National Space Science Data Center (2007). *COSPAR international reference atmosphere (CIRA-86)*, 2007. 6

[Nei13] A. Neiser, J. Adamczewski-Musch, M. Hoek, et al. *TRB3: a 264 channel high precision TDC platform and its applications. Journal of Instrumentation*, 8(12):C12043, 2013. doi:10.1088/1748-0221/8/12/C12043. 54

[NIS18] NIST. *CODATA values of the fundamental physical constants.* `https://physics.nist.gov/cuu/Constants/index.html`, 2018. Accessed: 2024-01-01. 13

[Par71] V. Parkhomchuck, Y. Pestov, and N. Petrovykh. *A spark counter with large area. Nuclear Instruments and Methods*, 93(2):269–270, 1971. doi:10.1016/0029-554X(71)90475-7. 24

[PDG21] PDG. *The review of particle physics (2020 and 2021 update). P.A. Zyla et al. (Particle Data Group), Prog. Theor. Exp. Phys., 083C01*, 2021. 4, 8, 9, 10, 12, 13, 15, 16, 17, 118, 119

[PDG24] PDG. *The review of particle physics (2024). S. Navas PDG (Particle Data Group), Phys. Rev. D 110, 030001*, 2024. 24, 31, 33

[Pfo35] G. Pfotzer and E. Regener. *Vertical intensity of cosmic rays by threefold coincidences in the stratosphere. Nature*, 1935. 6

[Pfo36] G. Pfotzer. *Dreifachkoinzidenzen der ultrastrahlung aus vertikaler richtung in der stratosphäre. Zeitschrift für Physik*, 1936. 6

[Pri03] W. C. Priedhorsky, K. N. Borozdin, G. E. Hogan, et al. *Detection of high-Z objects using multiple scattering of cosmic ray muons. Review of Scientific Instruments*, 74(10):4294–4297, 2003. doi:10.1063/1.1606536. 21

[Pro13] S. Procureur, R. Dupré, and S. Aune. *Genetic multiplexing and first results with a $50\times50cm^2$ micromegas. Nuclear Instruments and Methods in Physics Research Section A: Accelerators, Spectrometers, Detectors and Associated Equipment*, 729:888–894, 2013. doi:10.1016/j.nima.2013.08.071. 28

[Pug06] G. Pugliese. *The RPC system for the CMS experiment.* In *2006 IEEE Nuclear Science Symposium Conference Record*, volume 2, pages 822–826, 2006. doi:10.1109/NSSMIC.2006.355977. 1

[Pum69] J. Pumplin. *Application of sommerfeld-watson transformation to an electrostatics problem. American Journal of Physics*, 37(7):737–739, 1969. ISSN 0002-9505. doi:10.1119/1.1975793. 94

[Rae38] H. Raether. *Über eine gasionisierende strahlung einer funkenentladung. Zeitschrift für Physik*, 110(9):611–624, 1938. doi:10.1007/BF01340219. 39

[Rae39] H. Raether. *Die entwicklung der elektronenlawine in den funkenkanal. Zeitschrift für Physik*, 112(7):464–489, 1939. doi:10.1007/BF01340229. 39

[Rae40] H. Raether. *Zum aufbau von gasentladungen. Naturwissenschaften*, 28(47):749–750, 1940. doi:10.1007/BF01475193. 39

[Rae64] H. Raether. *Electron Avalanches and Breakdown in Gases*. London Butterworth, 1964. 38, 39, 40, 44

[Ram39] S. Ramo. *Currents induced by electron motion. Proceedings of the IRE*, 27(9):584–585, 1939. doi:10.1109/JRPROC.1939.228757. 43, 46, 150

[Rie72] F. F. Rieke and W. Prepejchal. *Ionization cross sections of gaseous atoms and molecules for high-energy electrons and positrons. Phys. Rev. A*, 6:1507–1519, 1972. doi:10.1103/PhysRevA.6.1507. 31

[Rie03] W. Riegler, C. Lippmann, and R. Veenhof. *Detector physics and simulation of resistive plate chambers. Nuclear Instruments and Methods in Physics Research Section A: Accelerators, Spectrometers, Detectors and Associated Equipment*, 500(1):144–162, 2003. doi:10.1016/S0168-9002(03)00337-1. 41, 43

[Rie04] W. Riegler and C. Lippmann. *The physics of resistive plate chambers. Nuclear Instruments and Methods in Physics Research Section A: Accelerators, Spectrometers, Detectors and Associated Equipment*, 518(1):86–90, 2004. doi:10.1016/j.nima.2003.10.031. 32

[Ros41] B. Rossi and K. Greisen. *Cosmic-ray theory. Reviews of Modern Physics*, 13:240–309, 1941. 17

[Ros42] B. Rossi and N. Nereson. *Experimental determination of the disintegration curve of mesotrons. Phys. Rev.*, 62:417–422, 1942. doi:10.1103/PhysRev.62.417. 24

[San81] R. Santonico and R. Cardarelli. *Development of resistive plate counters. Nuclear Instruments and Methods in Physics Research*, 187(2–3):377–380, 1981. doi:10.1016/0029-554X(81)90363-3. 24

[Sar20] J. P. Saraiva, A. Blanco, J. Garzón, et al. *The TRISTAN detector—2018–2019 latitude survey of cosmic rays. Journal of Instrumentation*, 15(09):C09024–C09024, 2020. doi:10.1088/1748-0221/15/09/c09024. 1, 5

[Sar23a] J. P. Saraiva, C. Alemparte, D. Belver, et al. *Advances towards a large-area, ultra-low-gas-consumption RPC detector. Nuclear Instruments and Methods in Physics Research Section A: Accelerators, Spectrometers, Detectors and Associated Equipment*, 1046:167744, 2023. doi:10.1016/j.nima.2022.167744. 3, 21, 63

[Sar23b] J. P. Saraiva, C. Alemparte, D. Belver, et al. *A large-area MRPC detector for muon scattering tomography. Nuclear Instruments and Methods in Physics Research Section A: Accelerators, Spectrometers, Detectors and Associated Equipment*, 1050:168183, 2023. doi:10.1016/j.nima.2023.168183. 3, 21, 22, 125

[Sar24] J. P. Saraiva and A. Blanco. *New readout scheme for large area timing & position RPCs. Nuclear Instruments and Methods in Physics Research Section A: Accelerators, Spectrometers, Detectors and Associated Equipment*, 1068:169803, 2024. doi:10.1016/j.nima.2024.169803. 3, 126

[Sar25] J. P. Saraiva and A. Blanco. *New readout codification of large-area multi-gap timing RPCs for muon scattering tomography. Nuclear Instruments and Methods in Physics Research Section A: Accelerators, Spectrometers, Detectors and Associated Equipment*, 1076:170466, 2025. doi:10.1016/j.nima.2025.170466. 3, 125, 126

[Sch03] L. J. Schultz. *Cosmic Ray Muon Radiography.* Ph.D. thesis, Portland State University, 2003. 21, 130

[Sho38] W. Shockley. *Currents to conductors induced by a moving point charge. Journal of Applied Physics*, 9(10):635–636, 1938. ISSN 0021-8979. doi:10.1063/1.1710367. 46, 150

[Sim52] J. A. Simpson, W. Fonger, and S. B. Treiman. *Cosmic radiation intensity-time variations and their origin. Physical Review*, 90(5), 1952. 7, 8

[Sma21] D. F. Smart and M. A. Shea. *Vertical geomagnetic cutoff rigidities for epoch 2015.* In *Proc. of the 36th International Cosmic Ray Conference*, ICRC, 2021. doi:10.22323/1.358.1154. 5

[Smi05] I. B. Smirnov. *Modeling of ionization produced by fast charged particles in gases. Nuclear Instruments and Methods in Physics Research Section A: Accelerators, Spectrometers, Detectors and Associated Equipment*, 554(1):474–493, 2005. doi:10.1016/j.nima.2005.08.064. 31

[Tei22] P. Teixeira, L. Afonso, S. Andringa, et al. *Muography for underground geological surveys: ongoing application at the Lousal mine. Journal of Advanced Instrumentation in Science*, (278), 2022. doi:10.31526/JAIS.2022.287. 15

[Tim81] J. G. Timothy, G. H. Mount, and R. L. Bybee. *Multi-anode microchannel arrays. IEEE Transactions on Nuclear Science*, 28(1):689–697, 1981. doi:10.1109/TNS.1981.4331264. 27

[Tim89] J. G. Timothy, J. S. Morgan, D. C. Slater, et al. *MAMA detector systems: A status report.* 1158:104–117, 1989. doi:10.1117/12.962535. 27

[Tow00] J. S. Townsend. *The conductivity produced in gases by the motion of negatively-charged ions. Nature*, 62(1606):340–341, 1900. doi:10.1038/062340b0. 35

[Tsa74] Y.-S. Tsai. *Pair production and bremsstrahlung of charged leptons. Reviews of Modern Physics*, 46(4):815–851, 1974. 17

[Urq09] J. Urquijo, A. M. Juárez, E. Basurto, et al. *Electron swarm coefficients in 1,1,1,2 tetrafluoroethane (R134a) and its mixtures with Ar. The European Physical Journal D*, 51(2):241–246, 2009. doi:10.1140/epjd/e2008-00288-6. 36, 37

[Vla24] V. Vlachoudis, A. Donadon, G. Hugo, et al. *FLAIR3 – recasting simulation experiences with the advanced interface for FLUKA and other monte carlo codes. EPJ Web Conf.*, 302(11005), 2024. doi:10.1051/epjconf/202430211005. 107

[Woo98] B. E. Woodgate, R. A. Kimble, C. W. Bowers, et al. *The space telescope imaging spectrograph design. Publications of the Astronomical Society of the Pacific*, 110(752):1183, 1998. doi:10.1086/316243. 28

[Yue14] X. Yue, M. Zeng, Y. Wang, et al. *An encoding readout method used for multi-gap resistive plate chambers (MRPCs) for muon tomography. Journal of Instrumentation*, 9(09):C09033, 2014. doi:10.1088/1748-0221/9/09/C09033. 28

[Yue16] X. Yue, M. Zeng, Z. Zeng, et al. *Mathematical modelling and study of the encoding readout scheme for position sensitive detectors. Nuclear Instruments and Methods in Physics Research Section A: Accelerators, Spectrometers, Detectors and Associated Equipment*, 816:33–39, 2016. doi:10.1016/j.nima.2016.01.080. 29

[Zeb96] E. C. Zeballos, I. Crotty, D. Hatzifotiadou, et al. *A new type of resistive plate chamber: The multigap RPC. Nuclear Instruments and Methods in Physics Research Section A: Accelerators, Spectrometers, Detectors and Associated Equipment*, 374(1):132–135, 1996. doi:10.1016/0168-9002(96)00158-1. 25

[Zeb97] E. C. Zeballos, I. Crotty, D. Hatzifotiadou, et al. *Latest results from the multigap resistive plate chamber. Nuclear Instruments and Methods in Physics Research Section A: Accelerators, Spectrometers, Detectors and Associated Equipment*, 392(1):145–149, 1997. doi:10.1016/S0168-9002(97)00222-2. 25

A

HV Adjustment with Pressure and Temperature

The equation for dynamic High-Voltage (HV) adjustment as a function of atmospheric pressure and temperature can be derived starting from the ideal gas law:

$$P \cdot V = n \cdot k_B \cdot T, \tag{A.1}$$

with P the pressure [Pa] and V the volume [m^3] of the gas, n the number of molecules or atoms, k_B the Boltzmann constant 1.380649×10^{-23} kg·m^2·s^{-2}·K^{-1}, and T the absolute temperature [K].

Using the gas number density $N = n/V$ (introduced in Subsection 3.2.1) in Equation (A.1), one obtains:

$$P = N \cdot k_B \cdot T \Leftrightarrow N = \frac{P}{k_B \cdot T} \tag{A.2}$$

In turn, the electric field E resulting from the applied voltage is given by:

$$E = \frac{HV}{d}, \tag{A.3}$$

where HV is the voltage applied to the external resistive electrodes and d is the total gas gap distance where ionizations occur.

Dividing Equation (A.3) by Equation (A.2) yields:

$$E/N = k_B \frac{HV \cdot T}{d \cdot P}, \tag{A.4}$$

which relates the reduced electric field E/N (see Subsection 3.2.2) to the HV set by the High-Voltage Power Supply (HVPS), the total gas gap distance d, and the gas pressure P and temperature T. Rewriting Equation (A.4):

$$HV = \frac{E/N \cdot d \cdot P}{k_B \cdot T}, \tag{A.5}$$

which enables periodic HV corrections based on pressure and temperature measurements, while keeping the applied reduced electric field constant.

Expressing E/N in Townsend, d in cm, P in mbar, and T in K, the Boltzmann constant can be rewritten as $k = \sim 0.01381\ mbar \cdot cm^3 \cdot K^{-1}$.

B

Charge Induction on a Readout Electrode

The instantaneous current induced i_{ind} on a readout electrode by a charge q moving with drift velocity $\vec{v}$ is given by the Shockley–Ramo theorem [Ram39, Sho38] as the product of the charge and the dot product of its velocity with the weighting field $\vec{E}_w$:

$$i_{ind} = q\vec{v} \cdot \vec{E}_w. \tag{B.1}$$

For dimensional consistency, Equation (B.1) implies that $\vec{E}_w$ must have units of inverse length, given that the weighting potential V_w is dimensionless.

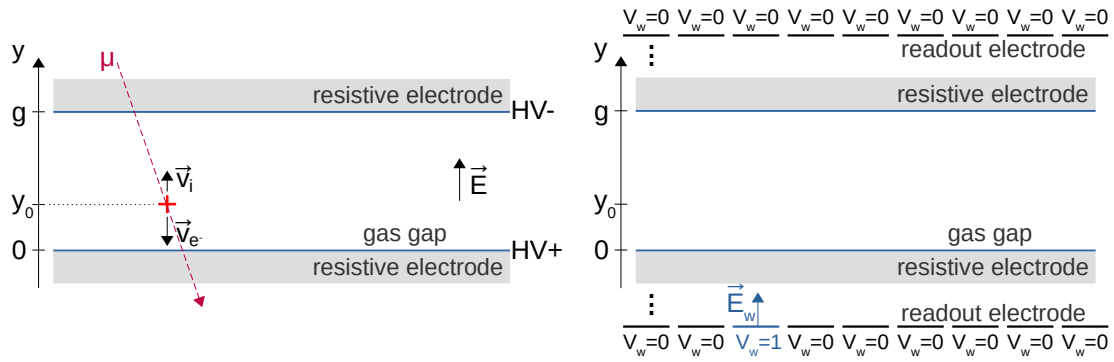

(a) (b)

FIGURE B.1: (a) Ionizing event creating an ion-electron pair in the gas gap; (b) Illustration of the Shockley–Ramo theorem: point charge removed, selected electrode at unit potential, and all other conductors grounded.

In the case of an ion-electron pair generated at an arbitrary position y_0 inside a gas

gap of thickness g (see Figure B.1), the induced current results from the sum of the individual contributions due to the motion of both particles toward their respective resistive electrodes:

$$i_{ind} = e\vec{v}_i \cdot \vec{E}_w - e\vec{v}_e \cdot \vec{E}_w, \tag{B.2}$$

where the elementary charge is represented by e, with the index i referring to the ion's contribution and e referring to the electron's contribution.

Integrating Equation (B.2) over the respective drift times along the gap yields the total induced charge Q_{ind} on the readout electrode due to the motion of both particles:

$$Q_{ind} = \int_0^{t_i} e\vec{v}_i \cdot \vec{E}_w \, dt \; - \int_0^{t_e} e\vec{v}_e \cdot \vec{E}_w \, dt. \tag{B.3}$$

Assuming that both carriers move only along the Y-axis (normal to the readout electrode surface), the following simplification arises:

$$\begin{aligned} Q_{ind} &= e\int_0^{t_i} v_{i,y}E_{w,y}\,dt \; + e\int_0^{t_e} v_{e,y}E_{w,y}\,dt \\ &= e\int_{y_0}^{g} E_{w,y}\,dy \; - e\int_{y_0}^{0} E_{w,y}\,dy \\ &= e\int_{y_0}^{g} E_{w,y}\,dy \; + e\int_{0}^{y_0} E_{w,y}\,dy \\ &= e\int_0^{g} E_{w,y}\,dy. \end{aligned} \tag{B.4}$$

Finally, since along the Y-axis $E_{w,y} = -dV_w/dy$, the total induced charge can be expressed in terms of the weighting potential:

$$\begin{aligned} Q_{ind} &= e\int_0^{g} -\frac{dV_w}{dy}\,dy \\ &= e\int_g^{0} dV_w \\ &= e\,(V_w(0) - V_w(g)) \\ &= -e\,\Delta V_w. \end{aligned} \tag{B.5}$$